Energy-Related Applications of Molecular Simulations

By

Isaak Daniels

Submitted to the Department of Chemistry and the
Graduate Faculty of the University of Kansas
in partial fulfillment of the requirements for the degree of
Doctor of Philosophy

Committee members

Prof. Brian B. Laird, Chairperson

Prof. Ward H. Thompson

Prof. Marco Caricato

Prof. Krzysztof Kuczera

Prof. Kyle Camarda

Date defended: May 04, 2016

The Dissertation Committee for Isaak Daniels certifies
that this is the approved version of the following dissertation :

Energy-Related Applications of Molecular Simulations

Prof. Brian B. Laird, Chairperson

Date approved: July 07, 2016

Abstract

We employ molecular simulations to investigate two key issues pertinent to sustainable energy: reducing emissions of CO_2 into the atmosphere and the use of renewable energy sources. Specifically, we use Monte Carlo simulations to study adsorption of various gases into Zeolitic Imidazolate Frameworks (ZIFs). For the latter project, we examine the dielectric constant of several organic solvent systems under different stimuli.

GCMC simulations were used to study three groups of ZIFs, each of which has a common functional group, but differing topology. We examined adsorption of pure CO_2 and pure CH_4. Agreement with experiment was considerably good for the majority of systems. We examined the effect electrostatics had on adsorption for CO_2. We also created visualizations of where the guest molecules preferred to reside in the ZIFs. We also simulated adsorption of H_2S into two groups of ZIFs, one of which was used previously. The new set consists of ZIFs which vary in topology but possess the same functional group.

For our second project, we examined the effect of applying an electric field at various field strengths, and adding various salt using molecular dynamics. Our force fields were found to produce good agreement for our solvents for density and dielectric constant. We found that for certain solvents, a large enough field causes the solvent to freeze, which is corroborated by dielectric data and simulation snapshot. We found that the dielectric constant decreases generally with the application of electric field and addition of salt. Crystallization was observed for solutions including NaBr, which matches experimental findings.

Acknowledgements

I have many people to thank for my being able to work on this manuscript regarding my research for the last several years. I would like to first thank my mother, who helped me realize my potential by allowing me to follow my various passions, whether film or relevant to this work, theoretical chemistry.

For immersing me into the world of physical chemistry, I would like to acknowledge Professor Kurt Christoffel of Augustana College, whose tests were notorious for their duration and difficulty. The classes I took under him showed that behind the seeming simplicity of equations lied quite arduous mathematical techniques.

I will forever be indebted to Professor Brian Laird, whose intelligence I will always be in awe of and hope one day to replicate. He has also been more than willing to assist my group members and me whenever we encountered an issue during our research, making good use of whiteboards. My group members have also proved more than willing to help me with any queries I may have. Specifically, I would like to thank the following members: Ning He (for assisting me in ZIF research and helping me get acclimated with the TOWHEE code I would use for that project); Dr. Jesse Kern (for always being ready to answer any question I had), Dr. Zhenxing Wang (for assisting me in making code that I ultimately used to compose my first first-author paper), and Dr. Soohwan Lee (for being willing to offer helpful suggestions)

Contents

List of Figures

List of Tables

Chapter 1

Introduction

Society has started to give increased attention to the problems attributable to our dependence on fossil fuels – namely the finite amount available and the harmful byproducts given off during fuel consumption. To circumvent the energy-related issues of our day, we must decompose this larger issue into several more comprehensible ones, specifically more renewable resources and mechanisms to capture these byproducts before introduced into the environment. As will be detailed below, this work seeks to address some of these issues.

This thesis has its basis in the computer simulation of molecular systems, which makes a cursory summary of the methods used in this work essential. Chapter 2 explains the basic principles of Molecular Dynamics and Monte Carlo simulations. These methods solve for the thermodynamical and physical values we ultimately want to determine, but are implemented in different ways.

Once we examine the basics of these methods, we examine the first of the topics of investigation, specifically the development of technologies and materials to capture greenhouse gases such as CO_2 from flue gases. In particular, we explore the ability of a recently developed class of systems called Zeolitic Imidazolate Frameworks, which are a subset of a broader class of systems known as metal organic frameworks (MOFs). These systems have demonstrated wide use for the purpose of capturing greenhouse gases, particularly CO_2 , in experimental settings. They have also been found to separate CH_4 from the other gases that consist of natural gas, such as CO_2. ZIFs

possess a high level of tunability to tailor its use. Three principal methods by which these systems can be changed is through topology, functional group and using a different metal atom. Simulations have found considerable use in providing understanding of the specific properties that aid in adsorption.

Chapters 3-4 treat various methods to examine the characteristics in ZIFs that lead to adsorption of gases. Chapter 3 delves into the considerable literature produced by the examination of ZIFs. This field has not only attracted numerous experimental papers, but has also inspired interest in theoreticians to employ multiple methods of computer simulations. In chapter 4, we first examine adsorption of pure CO_2 for three sets of ZIFs, each possessing the same functional group. We also gauge the adsorption of CH_4, because it is the main component of natural gas. We compare our data to experimental work performed by our collaborators.

Once we determine that our force fields provide reasonable agreement with respect to experimental findings, we examine the effect of removing electrostatic interactions on adsorption of the above-mentioned gases. This allows us to gain a better understanding of the mechanism of adsorption for the ZIFs under study. We also create density maps of the guest molecules in the various ZIFs, which we use to examine where preferential adsorption can be found. To determine the effect of pressure we examine the systems at pressures more than an order of magnitude apart.

In addition to greenhouse gases, other gases can enter the atmosphere. Instead of contributing to global warming, however, these gases can pose an immediate risk to human health. An example of such a gas is H_2S. For this reason we study the adsorption of H_2S for two groups of ZIFs, one of which we examined previously in this work and another from Ref. 7 which in lieu of possessing the same functional group, instead has the same topology.

Managing harmful gases to either the atmosphere or human health is one method materials science can better society. Another method relates to society's need for renewable sources of energy. Solar and wind energy are gaining prominence because of their renewability and nonexistent waste byproducts. However, they are intermittent, and might not be able to supply energy when it is most needed. To solve this problem, energy storage systems can be used. An example of such

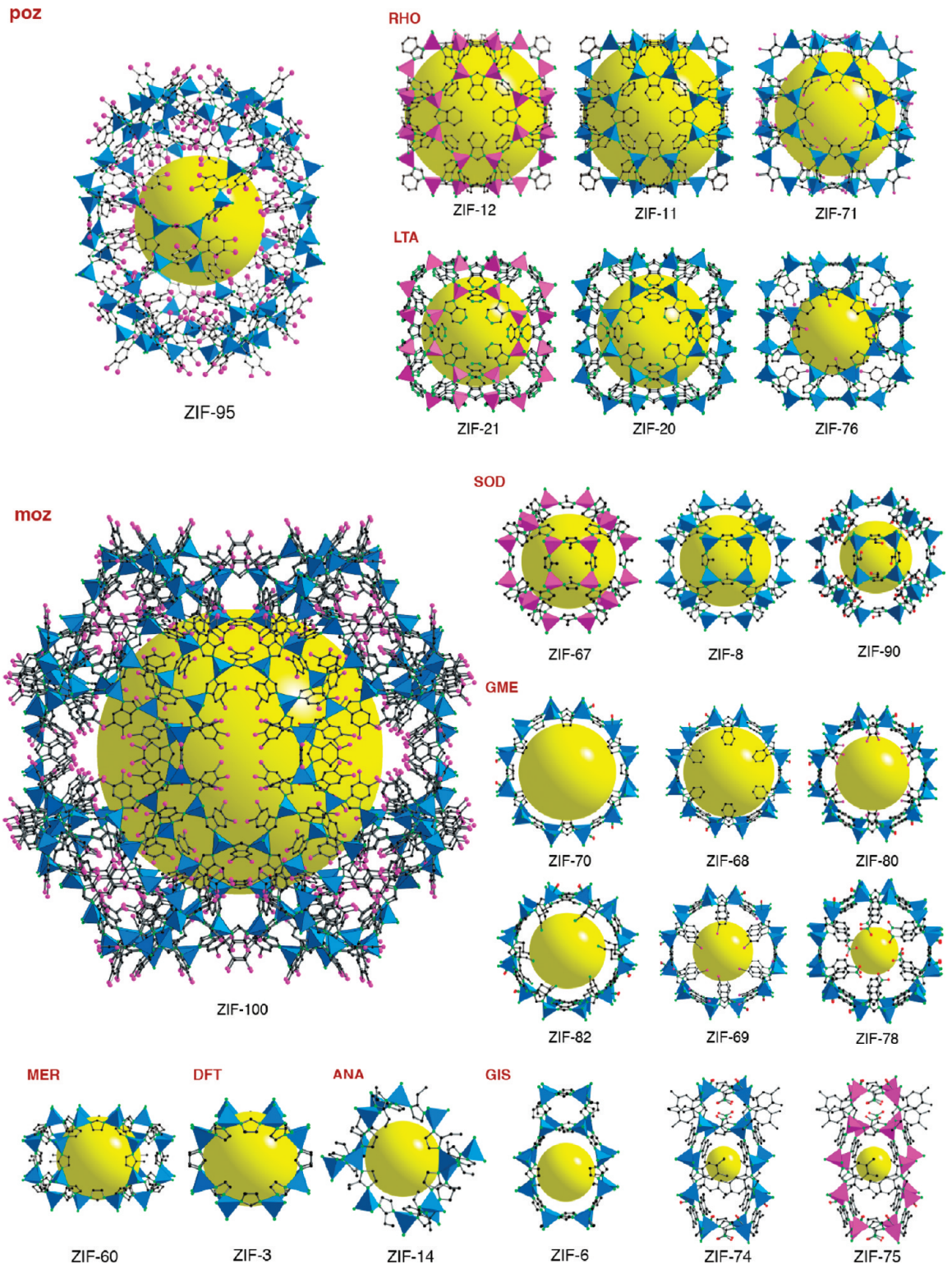

Figure 1.1: Models of selected known ZIF structures. The three letter designation refers to topology. The yellow ball indicate cage of ZIF. In the molecular structures the following coloring scheme was used. Black: carbon; Green: nitrogen; Red: oxygen; Pink: chlorine. From Ref. 1.

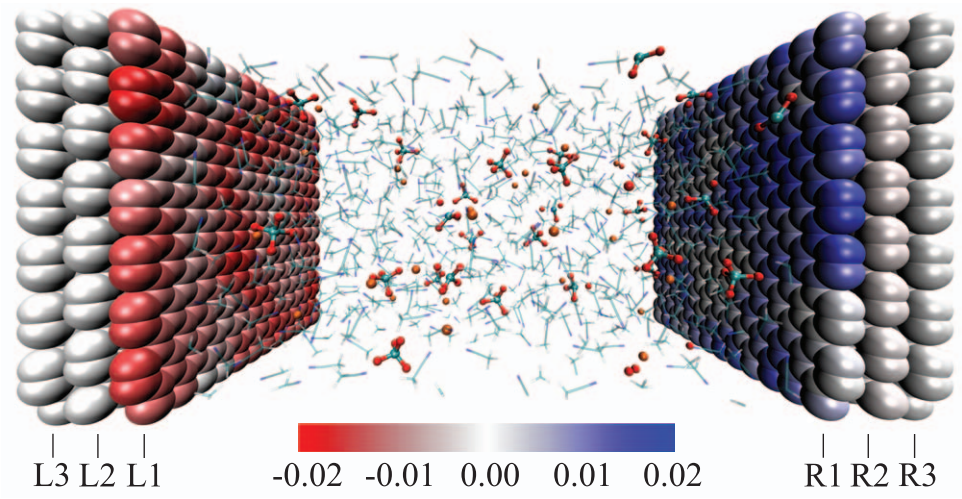

Figure 1.2: Image of EDLC model in which graphene electrodes surround MeCN solvent containing $LiClO_4$ electrolyte. Orange: Li^+ ions; Red: O in ClO_4 ions; MeCN molecules represented by 'stick models'. Reproduced from Ref. 2.

a system is a supercapacitor. Part II explores the other main topic of this thesis, namely exploring the dielectric behavior of solvents under varying conditions. Solvents (often with the addition of electrolytes) are used in supercapacitors. We will consider the class of supercapacitors known as electric double-layer capacitors (EDLCs). These systems store energy principally via electrostatic interactions between an electrode and the nearest layer of ions, forming a version of a capacitor. EDLCs can be modeled approximately using continuum methods, which is more efficient than considering the entire system on an atomistic scale. However, using such a model requires input parameters. One method to obtain these parameters is to perform atomistic simulations. The parameter we are interested in gives the effect of the electric field on the dielectric constant.

The effect of applied electric field on dielectric constant for four pure electrolyte solvents (ethylene carbonate, propylene carbonate, acetonitrile and dimethyl carbonate) and several molar ratios of ethylene carbonate and dimethyl carbonate was investigated. We fit our data to a model for the electric field dependence of dielectric constant developed by Booth. The dielectric constant decreased for the most part with respect to electric field. For most of the systems analyzed, the fit to the Booth model was good; however we observed several anomalously low dielectric constant

values for several of our systems at high electric fields. We performed additional analysis, and concluded the solvents were undergoing a process called electrofreezing.

The effect the addition of salt has on the dielectric constant was also examined. We compared our data with that of Ref. 18. We examined the salts sodium iodide (NaI) and lithium bromide (LiBr), which were in the paper. We also tested solutions of sodium bromide (NaBr) and lithium iodide (LiI) to determine the effect of changing one of the ions, and found that the dielectric decrement was anomolously smaller for solutions of NaBr. We then sought to understand how our data can be explained atomistically. To accomplish this, we determined the coordination number of N(MeCN) with respect to the cations used to determine if we could find any correlation, which we did. We also examined snapshots of a subset of our simulations to gain further understanding. We observed that the ions of NaBr mostly formed an agglomeration, This finding agreed with the experimental observation that NaBr has a low solubility in MeCN. The dielectric decrement of PC solutions of NaI, NaBr and LiBr were also examined. Finally, we determined the dielectric decrement for varying molar ratios of EC/DMC solutions containing NaI. We found that the choice of salt molecule had little to no effect on the dielectric decrement of PC. For EC/DMC solutions, the dielectric decrement overall increases with a larger molar concentration of EC, with notable dielectric increment occuring for solutions containing 0.9 molar fraction DMC and for pure DMC.

Chapter 2

Molecular Simulations

2.1 Introduction

Research into issues relevant to materials science provides society materials through which it can better function. Two examples of such research are the development of materials to capture greenhouse gases before they can enter the atmosphere and the creation of more efficient systems to store energy produced by renewable sources. Experimental work on these topics can and is complemented by investigations using molecular simulations. Molecular simulations give several benefits, such as not requiring physical contact with caustic substances and the ability to examine physical processes in detail at the atomic scale. Simulations have seen a large growth in capabilities in the last sixty years since Metropolis, et al.[19] published their seminal paper on what was to be known as "Metropolis Monte Carlo" and Alder and Wainwright[20] used early molecular-dynamics to examine the dynamics of hard spheres. A large number of computational methods have been devised for examining molecular systems. The two principal methods to be discussed in this chapter are Metropolis Monte Carlo (MMC) and molecular-dynamics (MD) simulations. To perform these simulations, a number of molecular parameters are needed to describe the system under study (e.g. bond lengths, angles, dihedrals, charges, et al.).

2.2 Monte Carlo

Within the classical approximation, chemical systems at equilibrium can be completely understood using statistical mechanics through its partition function, which has the form[21]

$$Z = \frac{1}{h^{dN}N!}\int d\mathbf{p}^N d\mathbf{r}^N \exp\left(-_i H\left(\mathbf{r}^N\mathbf{p}^N\right)/k_B T\right) \tag{2.1}$$

where $H\left(\mathbf{r}^N\mathbf{p}^N\right)$ denotes the Hamiltonian (energy) of the system. $H\left(\mathbf{r}^N\mathbf{p}^N\right)$ is comprised of a kinetic energy term (which depends on the momenta of the particles, $\mathbf{p}^N$) and a potential energy term (which depends on the position of the particles $\mathbf{r}^N$). The variable d represents the dimensions of the system and h^{dN} denotes the volume in "classical phase space." The Hamiltonian has the form (for a classical system)

$$H\left(\mathbf{r_i}^N\mathbf{p_i}^N\right) = \sum_{i=1}^{N}\frac{p_i^2}{2m_i} + U(\mathbf{r}^N). \tag{2.2}$$

The equilibrium expectation value of any dynamical variable F can be computed using the partition function as follows

$$\langle F\rangle = \frac{\int F\left(\mathbf{r^N}\right)\exp\left[-\beta H\right]d\mathbf{r}^N d\mathbf{p}^N}{Z}. \tag{2.3}$$

Because N is extremely large for a microscopic system, solving for the partition function is both analytically and numerically unfeasible for all but a few highly idealized systems. This inability to solve for most systems is because of the high dimensionalities of the integrals in the partition function.

To avoid having to solve for the partition function explicitly, simulations can be employed to model the system under study. One simulation method that uses probability is the so-called Monte Carlo method, which relies on choosing random points in the trajectory of interest instead of performing an integration of the entire system. The name Monte Carlo arises from the use of random numbers in the method, echoing the games of chance performed in the eponymous city. An example[22] demonstrating the use of Monte Carlo is the calculation of π. A circle with a radius of 1 is enscribed within a square with a side length of two. Random numbers are generated to create a set of coordinates. If these coordinates fall within the circle they are counted as successful

attempts, and if not, are considered failed attempts. Given a sufficient number of points, the ratio of successful points to total points should be in reasonable agreement with the area of a circle with respect to the area of a square, the latter ratio being $\pi/4$. Thus, using this method gives an estimation of π.

One näive result of Monte Carlo is that all points are treated as equally probable, which in many problems is false. To work around this problem[21] we can make use of a different method of performing Monte Carlo simulations, called Metropolis Monte Carlo. To implement this method, we focus our attention on the "configurational part" of the partition function Q, because in classical statical mechanics, solving for the momentum is trivial. For a classical system at constant N,V,T,

$$Q = \int d\mathbf{r}^N \exp\left(-U\left(\mathbf{r}^N\right)/k_B T\right). \tag{2.4}$$

The variables N, V, and T give the thermodynamic conditions of the system, namely that these three variables are held fixed. The collection of all systems consistent with these conditions is often referred to as an *ensemble*. The probability density of particle positions is

$$\rho(\mathbf{r}^N) \equiv \frac{\exp\left[-\beta U\left(\mathbf{r}^N\right)\right]}{Q} \tag{2.5}$$

where Q is the configurational part of Z. With this relation, one now uses the concept of microscopic detailed balance, in which

$$\rho(o)\,\kappa(o \to n) = \rho(n)\,\kappa(n \to o) \tag{2.6}$$

where $\kappa(\mathrm{o} \to \mathrm{n})$is a "transition matrix" from an "old" (o) to "new" (n) state. If a given simulation follows the above equation, the number of moves accepted for the duration of the simulation equals the number of reverse moves. The transition matrix can be written as the product of a symmetric and an asymmetric matrix, the first giving the probability of performing a possible configurational move, $\alpha(o \to n)$ and the second giving the acceptance probability of performing this change, $acc(\mathrm{o} \to \mathrm{n})$. Using Eq. 2.6, one can observe that

$$\frac{acc\,(o \to n)}{acc\,(n \to o)} \quad = \quad \frac{\kappa\,(o \to n)}{\kappa\,(n \to o)} \quad = \quad \frac{\rho\,(\mathrm{n})}{\rho\,(\mathrm{o})} \quad = \quad \exp\left[-\beta\left[U\left(\mathbf{r}'^{N}\right) - U\left(\mathbf{r}^{N}\right)\right]\right]. \quad (2.7)$$

Thus, if one knows the energy of the system before and after a proposed move, one can determine the likelihood of the move being accepted.[19,21]

When performing Metropolis Monte Carlo, a randomly chosen system undergoes a change in internal configuration or position of one of its constituents, if one of the following conditions is met

1. The specified change results in a decrease in energy.

2. If 1. is not satisfied, the following actions are performed.

   (a) The difference $\exp\left(U\left(r'^{N}\right) - U\left(r^{N}\right)\right)$ is calculated, in which $U\left(r'^{N}\right)$ and $U\left(r^{N}\right)$ are, respectively, the energies calculated after and before the move.

   (b) The result is then compared with a random number uniformly distributed between 0 and 1 and if the former is larger, the move is accepted, and rejected otherwise. Thus, the the system will be biased toward the global minimum of the energy landscape.

2.2.1 Performing Monte Carlo For Different Statical Mechanical Ensembles

2.2.1.1 Constant *NVT* Monte Carlo

Now that the mathematical basis has been given for basic Metropolis Monte Carlo, further aspects can be examined. Several classes of Monte Carlo simulations can be performed in which various thermodynamic variables are held constant. The derivation for Monte Carlo given above uses an *NVT* ensemble (the same as the partition function).

2.2.1.2 Constant *NPT* Monte Carlo

Another possible distribution available to the researcher is *NPT* (isothermal-isobaric) in which the number of molecules, pressure and temperature are held constant. Volume can be varied by

rescaling variables in the Hamiltonian equation as follows

$$\mathbf{r}_i = L\mathbf{s}_i \tag{2.8}$$

where

$$L = V^{1/3}. \tag{2.9}$$

This scaling of position allows V to be an explicit variable in the partition function, which can be varied during a Monte Carlo simulation. The criteria for making a move is as follows

1. One can make a move either affecting the positions of the constituents or volume of the system. As before, a move which lowers energy is automatically accepted.

2. If 1. is not satisfied, the following actions will occur with respect to a random number uniformly distributed between 0 and 1, depending on the nature of the move

   (a) If a displacement change is selected, the move will occur if the random number is less than $\exp\left[-\beta\left(\left(U\left(\mathbf{s}'^N,\mathbf{V}\right)\right)-\left(U\left(\mathbf{s}^N,\mathbf{V}\right)\right)\right)\right]$.

   (b) If a volume change is selected, the move will occur if the random number is less than $\exp\left[-\beta\left(\left(U\left(\mathbf{s}^N,\mathbf{V}'\right)\right)-\left(U\left(\mathbf{s}^N,\mathbf{V}\right)\right)+P\left(V'-V\right)-\left(N+1\right)\beta^{-1}\ln\left(V'/V\right)\right)\right]$.

2.2.1.3 Grand Canonical Monte Carlo

Finally, another ensemble is Grand Canonical Monte Carlo (GCMC) or μVT Monte Carlo, in which the chemical potential, volume and temperature are fixed. For this ensemble, the number of molecules varies, thus the ensemble can be used to examine systems in which molecules enter and leave the system. GCMC is useful for examining adsorption, because this ensemble matches the experimental set up of adsorption in which guest molecules can enter and leave the host system. The rules for accepting a move are noted below.

1. A translational/orientational displacement of any of the substituents or molecule insertion or deletion is accepted if it lowers the system energy.

2. If 1. is not satisfied, a random number is chosen and compared with one of the three values below depending on the move chosen

   (a) For a displacement, $\exp\left(-\beta\left(U\left(r'^N\right)\right)-U\left(r^N\right)\right)$.

   (b) For a molecular insertion, $\frac{V}{\Lambda^3(N+1)}\exp\left(-\beta\left(\mu-U\left(N+1\right)-U\left(N\right)\right)\right)$, in which μ is chemical potential and Λ is the thermal wavelength.

   (c) For a molecular deletion, $\frac{N\Lambda^3}{V}\exp\left(-\beta\left(\mu-U\left(N-1\right)-U\left(N\right)\right)\right)$.

One common method to calculate chemical potential is "Widom insertion".[21,23] In this method, the energy difference is calculated when an additional atom or molecule is added to a system.

2.3 Molecular-Dynamics Simulation

Though Metropolis Monte Carlo is useful for a number of applications, its reliance entirely upon an equilibrium spatial probability distribution means that it provides no information with respect to time-dependent qualities. Dynamic observables such as the diffusion constant can not be calculated in this manner. To fill this gap, one can use molecular dynamics (MD). Unlike for MC, in MD one keeps track of not only position of the substituents, but also the momenta. To model atom movement, the classical laws of motion are employed for each step. As with MC, the theoretical basis for one of the probability distributions will be given, in this case, the *NVE* ensemble (micro-canonical). In MD, the classical laws of motion of Hamilton determine the trajectory of motion from the forces acting between the molecules. Hamilton's Equations of Motion are

$$\begin{cases} \dot{p} = -\dfrac{\partial H}{\partial r} = ma \\ \dot{r} = \dfrac{\partial H}{\partial p} \end{cases} \tag{2.10}$$

where $H\left(r^N, p^N\right)$ is the system Hamiltonian. As opposed to MC, MD requires a method of numerical integration to advance the trajectories from one step to another. One standard numerical integration algorithm for MD simulation is the Verlet method,[24] which gives the following equa-

tion with respect to position

$$r_i(t+\Delta t) \approx 2r_i(t) - r_i(t-\Delta t) + \frac{F\left(r_{ij}\right)h^2}{m} \tag{2.11}$$

where $F\left(r_{ij}\right)$ are the forces and Δt is the timestep. Eq. 2.11 can be rearranged to give the equation for velocity. In 1982,[25] an equation to directly calculate velocity from that of the previous step was derived (Velocity-Verlet),[21,22,25]giving the following numerical algorithm:

$$\begin{cases} r_i(t+\Delta t) = r(t) + \dfrac{\Delta t\, p_i}{m} + \dfrac{F(t)\,\Delta t^2}{2m} \\ p(t+\Delta t) = p(t) + \dfrac{1}{2}\Delta t\left(F[t] + F[t+\Delta t]\right) \end{cases}. \tag{2.12}$$

Verlet and Velocity-Verlet integrators are members of a larger group of numerical integrators called symplectic integrators. Symplectic integrators are able to preserve the geometric properties of the system's Hamiltonian.

In MD, specialized algorithms have been developed to control both pressure and temperature in the simulation. An algorithm to produce trajectories that are distributed according to a canonical (NVT) distribution was developed by Nosé.[26] This algorithm implements an *extended Hamiltonian*, in which additional variables are incorporated to sample from a given distribution. In Nosé's method the following variables are used

$$\begin{cases} r_i' = r_i \\ p_i' = p_i/s \\ t' = \displaystyle\int^t \frac{dt}{s} \end{cases} \tag{2.13}$$

where the variables describing the system are given in terms of 'virtual' variables and the variable s is used for scaling purposes. The Nosé Hamiltonian is written as follows

$$H = \sum_{i=1}^{3N} \frac{(p_i)^2}{2m_i s^2} + U(r^n) + \frac{(p_s)^2}{2Q} + g\frac{\ln s}{\beta} \tag{2.14}$$

where p_s is the momentum conjugate to s, Q serves as the "mass" to control s in units of energy/time^2 and g represents the degrees of freedom inherent in the system. The Nosé equation of motion gen-

erated by this Hamiltonian (including those for the scaling variables) are

$$\begin{cases} \dot{r}_i = \dfrac{p_i}{ms} \\ \dot{p}_i = -\dfrac{\partial U}{\partial r_i} \\ \dot{s} = \dfrac{p_s}{Q} \\ \dot{p}_s = \dfrac{\sum_i p_i^2/m_i s^2 - (g+1)\,kT}{s} \end{cases} . \tag{2.15}$$

Hoover[27] expanded Nosé's scheme, leading to the Nosé-Hoover algorithm, which has gained wide use, including in many of the simulations performed in this manuscript. The main difference between the Nosé-Hoover method from Nosé's original method is that the equations of motion are defined in real (not scaled) time. Using a variable transformation, Hoover recast Nosé's equations of motion in the following form

$$\begin{cases} \dot{q}_i = \dfrac{p_i}{m_i} \\ \dot{p}_i = -\dfrac{\partial U}{\partial r_i} - \zeta p \\ \dot{\zeta} = \dfrac{\sum_i m\dot{q}_i^2 - (g)\,kT}{Q} \end{cases} \tag{2.16}$$

where ζ is defined as p_s/Q. There is no Hamiltonian for this system[21,27].

For MD simulations, one controls the variable Q through a quantity τ, called the *damping parameter*, which defined through the following equation

$$Q = gk_BT\tau^2 \tag{2.17}$$

where τ is a damping parameter. To set up a proper thermostat that will ensure the simulation occurs at the temperature specified, one must choose a τ that is not too small, otherwise the simulation will spend a significant amount of time equilibrating around the temperature specified, and not choose a τ that is too large, which will induce rapid fluctuations in the temperature. A more sophisticated approach can be used to implement thermostats in MD simulations, namely using a Nosé-Hoover *chain*, in which multiple thermostats are allowed to respond to one another.[28] This procedure is employed in the simulations in Chapters 6 and 7, using three thermostats. LAMMPS also uses a procedure[29] that employs a chain of three thermostats for each degree of freedom of

the barostat in Chapters 6 and 7.

MD can also be performed using constant pressure conditions instead of constant volume, in order to sample from an isothermal-isobaric (or NPT) distribution. Andersen[30] explored how to implement constant pressure conditions for simulations using an extended Hamiltonian. A scaling factor was used as was done by Nosé, except in this instance position was the variable scaled as shown

$$s_i = \mathbf{r}_i / V^{1/3} \tag{2.18}$$

This allows volume to be used as an extended variable. Because the position coordinates have been redefined, the momentum conjugate will be re-expressed as shown

$$\pi_i = mQ^{2/3}\dot{\rho}_i. \tag{2.19}$$

The momentum conjugate to the variable Q is

$$\Pi = M\dot{Q} \tag{2.20}$$

with M representing the mass of the piston described above. The Nosé-Anserson Hamiltonian is

$$\mathscr{H}\left(s^N, \pi^N, Q, \Pi\right) = \frac{1}{2mQ^{2/3}} \sum_{i=1}^{N} \pi_i \cdot \pi_i + \sum_{i<j=1}^{N} u\left(Q^{1/3} s_{ij}\right) + \frac{1}{2M}\Pi^2 + \alpha Q. \tag{2.21}$$

As was the case for NVT simulations, we also control the damping parameter for volume in molecular dynamics. Rescaling the variables and using the equations of motion based on the Hamiltonian, the following equations are obtained

$$\begin{cases} \dfrac{d\mathbf{q_i}}{dt} = \dfrac{\mathbf{p}_i}{m} + \dfrac{1}{3}\mathbf{q}_i \dfrac{d\ln V}{dt} \\ \dfrac{d\mathbf{p_i}}{dt} = \displaystyle\sum_{i<j=1}^{N} -u'\left(\mathbf{q}_{ij}\right) - \frac{1}{3}\mathbf{p}_i \frac{d\ln V}{dt} \\ \dfrac{Md^2V}{dt} = -\alpha + \left(\dfrac{2}{3}\displaystyle\sum_{i=1}^{N} \frac{\mathbf{p}_i \cdot \mathbf{p}_i}{2m} - \frac{1}{3}\sum_{i<j=1}^{N} q_{ij} u\left(\mathbf{q}_{ij}\right)\right)/V \end{cases} \tag{2.22}$$

2.4 Choosing Force Fields

Both MD and MC simulations rely on a force field to calculate the forces used to determine the equilibrium configurations of the system under examination. The forces calculated with the aid of the parameters of the force field are used to calculate the total energy of the system at each step, which is typically divided as follows

$$E = E_{Bond} + E_{Angle} + E_{Dihedral} + E_{vanderWaals} + E_{Electro}. \tag{2.23}$$

Note that choosing a force field in this way applies to simulations based on empirical fitting, and that one can perform simulations in which energies are calculated on-the-fly by *ab-initio* calculations. Unfortunately, this leads to a shorter time frame and smaller system than one can examine using more empirical means, because more time is required to compute the energy using this method. For most classical simulations (including the ones detailed in this thesis) atomic charges do not fluctuate. Additional terms may be added to the force field to simulate molecular polarization. Choosing the type of force field may be assisted by comparing the results of the force field with experimental results. We can split the energy terms into those that rely on bonding and those that rely on nonbonding, discussed in the following subsections (2.4.1 and 2.4.2).

2.4.1 Parameters for Bonding Interactions

To fully understand the interactions for a molecule, we will write explicit equations for bonds, angles and dihedrals. For bonds, one can choose to model them using a harmonic functional form, which is a very common approach in simulation. This model is expressed with the following equation,

$$E_{Bond} = k_r (r - r_0)^2 \tag{2.24}$$

where r is the distance between bonded atoms at a given step, k_r is the force constant for the interaction and r_0 is the equilibrium bond length. Modeling the system harmonically is also used

frequently done for angles, with a similar equation to the above,

$$E_{Angle} = k_\theta \left(\theta - \theta_0\right)^2 \tag{2.25}$$

where θ is a bond angle, k_θ is a corresponding force constant and θ_0 is the equilibrium bond angle. Finally, for modeling dihedrals, there are various approaches to the system one can undertake. For our purposes, we will focus on two of the forms (harmonic and multi-harmonic). Unlike the equations for bonds and angles, a set equilibrium value is not used for either of these equations. The following equation is employed to solve for the harmonic dihedral energy

$$E_{Dihedral} = k_\phi \left(1 + d\cos\left[n\phi\right]\right) \tag{2.26}$$

where ϕ is a dihedral (arrangement of four consecutive atoms), k_ϕ is a corresponding force constant, d is either +1 or -1 (controlling the sign of the second term) and n is the periodicity, which is an integer parameter that depends on the symmetry of a molecule. For the multi-harmonic form, we use the following equation

$$\sum_{n=1}^{6} A_n \cos^{n-1}\left(\phi\right) \tag{2.27}$$

where A_i are coefficients with units of energy.

2.4.2 Parameters for Nonbonding Interactions

To model non-bonded van der Waals (vdW) interactions, the Lennard-Jones (LJ) potential has found widespread use. The equation for this is

$$E_{vdW} = 4\varepsilon_{ij}\left(\left[\frac{\sigma_{ij}}{r}\right]^{12} - \left[\frac{\sigma_{ij}}{r}\right]^{6}\right) \tag{2.28}$$

where σ_{ij} is the Lennard-Jones effective diameter between the centers of atom types i and j. and ε_{ij} and is the well depth of the energy of the interaction. The first term in Eq. 2.28 accounts for repulsion that occurs when the atoms are very close together, and the second term for attraction. One widespread method to model the LJ interaction between different atom types is Lorentz-

Berthelot mixing, in which the following equations are used

$$\sigma_{ij} = \frac{\sigma_i + \sigma_j}{2} \tag{2.29}$$

and

$$\varepsilon_{ij} = \sqrt{\varepsilon_i \varepsilon_j} \tag{2.30}$$

electrostatic interactions are modeled using Coulomb's equation,

$$E_c = \frac{q_i q_j}{r} \tag{2.31}$$

where q_i is the charge of atom i.

2.5 Periodic Boundary Conditions

Molecular simulations can undergo significant surface effects due to the confinement of the system in a bounded box, depending on the size of the system. Because increasing the number of molecules in the system will incur a larger computational cost, another method is needed to avoid these size effects. One method of avoiding size effects is to model infinite copies of the system along each principal axis. In this method, as a molecule crosses the boundary, it returns through the opposite boundary. To make sure an atom does not interact with both another atom and the image of that atom simultaneously for vdW interations, these interactions should be truncated. Figure 2.1 displays a simplified model of how periodic boundaries function in a simulation.

2.6 Ewald Sums

As noted, one aspect that is crucial to correctly modeling the system is the distribution of charges, because they will interact not only with other charges in the system but also the periodic images. Unlike Lennard-Jones interactions, directly calculating the energy contribution from electrostatics may yield a divergent quantity, thus it is critical to find another way to account for charge interaction across the periodic boundaries. One popular method for accomplishing this is

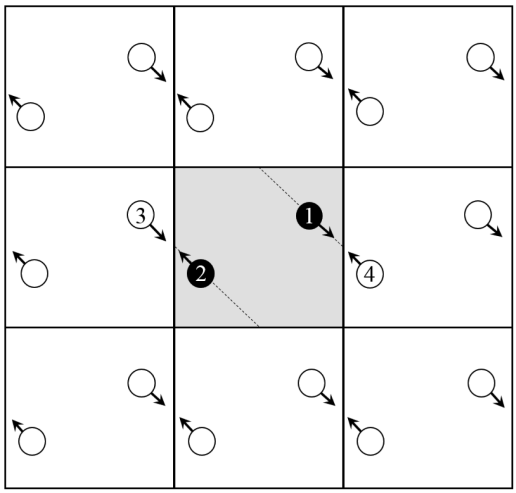

Figure 2.1: Two-dimensional visualization of two particles with periodic boundaries. Reproduced from Ref. 3.

the Ewald method.

This method involves setting up a charge cloud around each atom, which screens the atom and ensures that the electrostatic interactions are curtailed, giving a shorter required force calculation. Before this assumption, as noted in Ref. 21, the equation for the potential was 'poorly converging'. The standard method to model this charge cloud is as a sum of Gaussian functions centered on the lattice sites. The equation for the cloud has the form

$$\rho(r) = \sum_{j=1}^{N} \sum_{\mathbf{n}} q_j \left(\frac{\alpha}{\pi}\right)^{3/2} \exp\left(-\alpha \left|\mathbf{r} - \left(\mathbf{r_j} + nL\right)\right|^2\right) \tag{2.32}$$

with α proportional to the width of the Gaussian function, n representing the number of periodic copies and L the side-length of the system. We use Eq. 2.32 to solve for the following equation

$$k^2 \tilde{\phi}(k) = 4\pi \tilde{\rho}(k) \tag{2.33}$$

where $\tilde{\phi}(k)$ and $\tilde{\rho}(k)$ are the Fourier transforms of the potential and density, respectively. We obtain

$$\phi_1(r) = \sum_{k \neq 0} \sum_{j=1}^{N} \frac{4\pi q_j}{k^2} \exp\left(i\mathbf{k} \cdot \left[\mathbf{r} - \mathbf{r}_j\right]\right) \exp\left(-k^2/4\alpha\right) \tag{2.34}$$

and using the energy due the charge cloud is calculated to have the following form

$$U_1 = \frac{1}{2V}\sum_{k\neq 0}\frac{4\pi}{k^2}\left|\rho\left(\mathbf{k}\right)\right|^2\exp\left(-k^2/4\alpha\right) \tag{2.35}$$

where

$$\rho\left(k\right) = \sum_{i=1}^{N} q_i \exp\left(ik\cdot\mathbf{r}_j\right). \tag{2.36}$$

One must also add a term to account for the atom interacting with a charge cloud with an opposite charge of that of the first cloud. The use of this charge cloud ensures the sum charge of the system is not affected by all of the charge clouds. In order to subtract contributions to the energy from self-interaction, the following potential at $r = 0$ is used

$$\phi = 2q_i\left(\alpha/\pi\right)^{1/2} \tag{2.37}$$

resulting in

$$U_{\text{self}} = \left(\frac{\alpha}{\pi}\right)^{1/2}. \tag{2.38}$$

Finally, one calculates the energy from the original charges. With the original charge clouds, the interaction from these charges should be screened, with a potential of

$$\phi\left(r\right) = \frac{q_i}{r}\text{erfc}\left(\sqrt{\alpha}r\right) \tag{2.39}$$

giving

$$U\left(r\right) = \frac{1}{2}\sum_{i\neq j}^{N} q_i q_j \text{erfc}\left(\sqrt{\alpha}r_{ij}\right)/r_{ij}. \tag{2.40}$$

The following equation is computed for electrostatic interactions using the Ewald method to account for periodic boundaries

$$U\left(r\right) = \frac{1}{2V}\sum_{k\neq 0}\frac{4\pi}{k^2}\left|\rho\left(\mathbf{k}\right)\right|^2\exp\left(-k^2/4\alpha\right) - \left(\frac{\alpha}{\pi}\right)^{1/2}\sum_{i=1}^{N} q_i^2 + \frac{1}{2}\sum_{i\neq j}\frac{q_i q_j \text{erfc}\left(\sqrt{\alpha}r_{ij}\right)}{r_{ij}}. \tag{2.41}$$

Simulations employing partial charges and periodic boundaries, such as the simulations performed in this thesis, employ Ewald summation. To ensure that simulations perform correctly, it is key to choose reasonable parameters to model the cutoff and convergence criteria for Ewald summation. First, one must choose the type of summation to be used for the long-range electrostatic interactions. Ewald summation was used in all of our simulations. For our MC simulations

in Chapter 3 we used an unchanging number of vectors for $k-space$. In our MD simulations in Chapters 6 and 7, we used PPPM (particle-particle-particle-mesh),[31] which benefits from its relative efficiency with respect to other methods. In this method, the potential is solved for using Poisson's equation. The resulting potential is used to model the forces in k-$space$.[21]

Part I

Computer Simulation of Gas Adsorption in Zeolitic Imidazolate Frameworks

Chapter 3

Overview on Background Literature for Zeolitic Imidazolate Frameworks

3.1 Introduction

In this section, we review the potential use of Zeolitic Imidazolate Frameworks (ZIFs) for gas adsorption and separation. ZIFs are mesoporous crystalline materials that consist of metal atoms (often zinc or cobalt) connected by imidazolate groups. These systems reside in the larger class of crystal structures known as Metal Organic Frameworks (MOFs). ZIFs are labeled with the adjective 'Zeolitic' because they can possess many of the same topologies as those of zeolites. Zeolites are porous structures formed by silicon atoms linked by oxygen. Similarly, ZIFs are formed through metal atoms connected via an imidazole group. This similarity is shown in in Figure 3.1.

To visually understand what is meant by the *topology* of a ZIF (and why this property would be highly valued when synthesizing these structures), we refer to Figure 3.2, which shows a small subset of the variety of possible structures for ZIFs. The three letter code accompanying each ZIF denotes the topology of the particular system (i.e. sod is the 'sodalite' topology), and follows standard zeolite terminology.

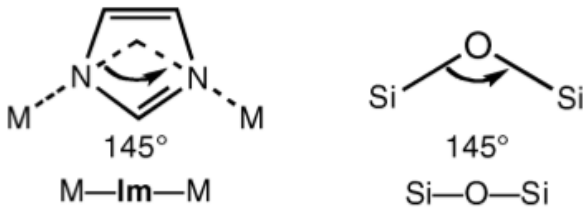

Figure 3.1: Bonding geometries for ZIFs (left) and zeolites (right). 'M' indicates the metal atom and 'Im' indicates the imidazolate group. (From Ref. 1).

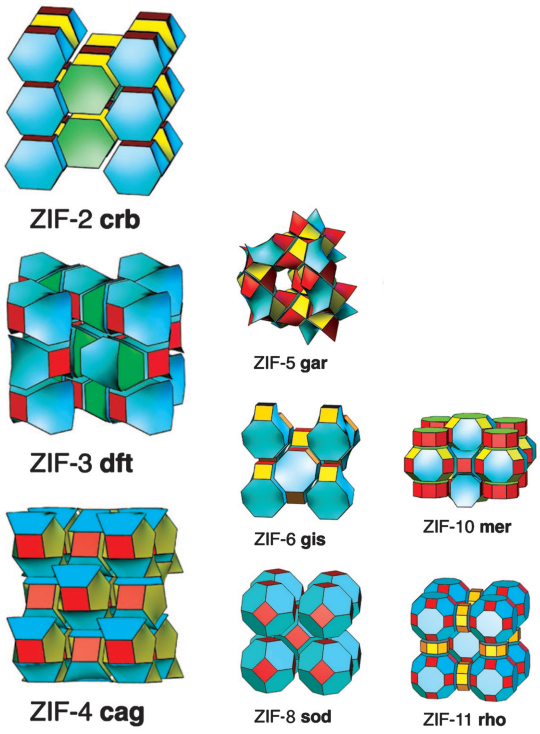

Figure 3.2: Subset of topologies of ZIFs. From Ref. 4.

ZIFs have a number of potential applications, such as gas-separation[1], liquid-separation[32–34], and acting as electrodes for supercapacitors[35]. To synthesize ZIFs that perform well in carbon capture and separation, understanding how varying the topology, functional group and metal atom affect their performance in these two areas is critical. This work was a collaboration sponsored by Molecularly Engineered Energy Materials(MEEM), and Energy Frontier Research Center(EFRC). We collaborated with other groups, including the Yaghi research group, which synthesized the

ZIFs and also provided us experimental data on adsorption of those ZIFs, and the Asta group, which performed binding energy calculations for CO_2 in ZIFs, and Professor Houndonougbo, who assisted in the implementation of classical simulations. This collaboration served the dual purpose of verifying that the force fields used in the simulation produce results consistent with experimental findings, and using simulations to obtain data and a molecular-level picture not easily accessible through experimental means. We examined the effect of both topology and functional groups on gas adsorption.

Scientific finding points to CO_2 as the predominant source of global climate change.[36] To prevent the release of this gas into the atmosphere (and separate it from the other gases that coexist with it in flue gas), various techniques have been used, of which chemical absorption and adsorption have been among the most popular methods to perform carbon capture. One estimate for the composition of flue gas from coal is 12.5-12.8 % CO_2, 6.2 % H_2O, 4.4 % O_2, 50 ppm CO, 420 ppm NO_x, 420 ppm SO_2 and 76-77 % N_2.[37] *Post-combustion* methods can be used to capture CO_2 from flue gas. For absorption, researchers note a number of problems that would hinder the use of conventional methods to capture CO_2, including the use of solvents (such as amine scrubbers) which can degrade to act as the absorbent and a significant energy input required to remove the absorbate from the material.[36,38,39] Absorbents such as amine scrubbers (e.g. monoethanolamine (MEA)) have been used previously in industry,[36,38–40] one example acting to separate CO_2 from the Shady Point plant in Oklahoma.[40] Ionic liquids as the solvent may be able to lower energy cost[36,38] and provide better stability.[38] Researchers have also made many contributions to the study of adsorption using various materials, including activated carbon and zeolites.[36,38–40] As stated in Ref. 38, requirements for optimal adsorption materials are "high CO_2 capacity at low pressure, high selectivity for CO_2, gas adsorption/desorption kinetics, good mechanical properties, high humid and chemical stability, as well as low costs of synthesis." As of 2013, MOFs suffered from much lower volumetric uptake of CO_2 with respect to MEA solution.[36]

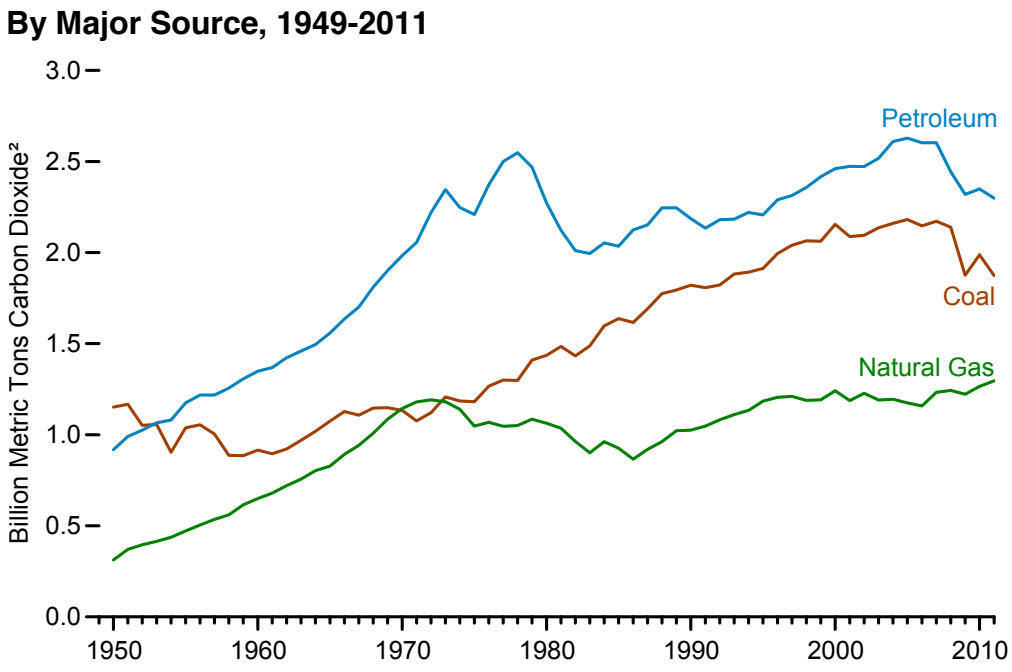

Figure 3.3: CO_2 emissions from 1949-2011 categorized by source. From Ref. 5.

3.2 Experimental research on ZIFs

ZIFs were first defined as a class of crystalline materials in the group of Omar Yaghi,[4] though several of these systems have been reported previously.[41–43] In addition to the topology, two other factors differentiating individual ZIFs are (a) the functional group (or groups) attached to the imidazole ring and (b) the specific metal atom or atoms joining these rings, though there is a paucity of experimental work in examining the effect of metal atom on gas adsorption.[44] In 2006, Park[4] made special notice of two ZIFs, ZIFs-8 and -11, (of which ZIF-11 was later studied by our group). In this paper, the authors noted several properties that would make them particularly desirable for commercial application. Both ZIFs showed excellent chemical stability in boiling solvent up to a period of seven days. These ZIFs also maintained structure at the temperature 550°C. ZIF-8 was also found to have very good stability in boiling water. Researchers also found that when the ZIF-8 framework contained water, it was better able to bind methane.[45] ZIF-8 was also found to perform better at storing H_2 when initially placed in water at ambient pressure.[46]. However, at 77 K, water had a deleterious effect on adsorption. A ZIF-68-based membrane was found to be

relatively stable in DMF (dimethylformamide), hexane and p-xylene.[47] These factors show ZIFs can function fairly well in the harsh conditions common in industry. ZIFs are not impervious to damage, however. In Ref. 47, boiling water at 100°C caused significant damage to ZIF-68. ZIF-8, when in the form of small crystals, degraded under humid conditions.[48] In 2008, a method was introduced in Ref. 49 to create twenty-five different ZIFs by combining several linkers and metal atoms in various ratios. This research showed that a variety of ZIFs could be efficiently produced and examined for their adsorption capacity. Also promisingly, the researchers were able to obtain several ZIFs with topologies that have not been observed for zeolites. In additional work, Yaghi, et al. was able to synthesize a series of ZIFs all with the Gmelinite (gme) topology,[50] create ZIFs with Linde Type A (lta) topology,[51] create a ZIF that was as of the time of the writing of the article one of the largest MOFs (ZIF-100) yet discovered,[52] and performed additional accomplishments. New types of ZIFs have also been synthesized. In 2015, a ZIF with a previously unseen topology was synthesized, with 10 crystallographically independent Zn^{2+} atoms, which the authors note as unprecedented for ZIFs.[53]

Researchers can also create ZIFs with different ratios of imidazolate functional groups[54–59] which enable a greater variety of potential ZIFs. Varying the composition of linkers is found to affect the porosity (measured by N_2 adsorption) and is hypothesized as a method to tune pore size.[54] Researchers have also been able to partially substitute the metal ions on some ZIFs,[59,60] with Ref. 59 substituting a portion of the Zn^{2+} cations with Mn^{2+}in ZIFs-71 and -8. Since the discovery of their excellent behavior with regard to adsorption many groups have examined numerous ZIFs to understand how each does in terms of adsorption, selectivity and other factors. One of the first papers relating to selectivity noted that ZIF-20 can selectivity adsorb CO_2 in a mixed stream containing CH_4.[51] Wu, et al.[61] explored the H_2 adsorption of ZIF-8 using neutron diffraction and DFT and concluded that the imidazolate linker was the main location for adsorption, a finding which would be echoed in later papers. Chmelik, et al.[62] used infra-red microscopy in conjunction with Monte Carlo simulations to examine that guest molecules in a CO_2/CH_4 stream can lead to blocking of the apertures in ZIF-8. Researchers have also grown ZIFs on support systems, forming

membranes.[48,63–97] As a specific example, a membrane was made for ZIF-69 supported by α-alumina and tested (among other things) the separation of CO_2 and CO, with selectivity favoring the CO_2 in Ref. 84. Some of the examples[48,89,91–98] of a membrane involved creating a "mixed matrix membrane" (MMM). An MMM consists of ZIF material distributed in a polymer.

ZIFs are not limited to only adsorbing CO, CO_2, CH_4, N_2 and H_2. The ability of ZIF to adsorb non-methane hydrocarbons has attracted considerable interest in the scientific community[70,71,76–78,80,83,89,91,92,96,98–119]with several works examining the potential to separate linear alkanes from branched ones[106,114,120] and separating alkenes from alkanes.[70,78,80,82,89,91,96,111,117–119] One example of ZIFs showing this selectivity (propane/propene) was hypothesized to originate from the pore windows selectively allowing propane to diffuse.[117] ZIF-8 was also used to test adsorption of phthalic acid and diethyl phthalate, with Khan noting good adsorption of phthalic acid.[121] Several works have shown that ZIF-8 can be used to adsorb iodine,[122,123] with Chapman, et al.[123] demonstrating that amorphizing the ZIF allows for iodine to be less likely to be de-adsorbed the ZIF. ZIFs have also been found to adsorb various alcohols, SO_2,[134] (stability of this gas for ZIFs tested,[135]) arsenic and arsenic containing compounds,[32,136,137] SF_6,[71,80] and theophylline.[138]

Experimentalists have also explored the mechanism of adsorption on ZIFs. In 2014,[139] Raman spectroscopy was used to examine the interactions CO_2 had with ZIF-69. The change in the 159 cm^{-1} peak with respect to CO_2 pressure gave evidence of the importance to adsorption from the interaction between CO_2 and the 5-chlorobenzimidazole functional group. Neutron powder diffraction has been used to examine (in tandem with DFT) binding sites preferred for CO_2 in ZIF-7.[6]. Figure 3.4 gives a diagram of ZIF-7 and how the constituents of the system are categorized. The authors note 'Cavity B' preferentially adsorbs guest molecule and from 100kPa to 200kPa, external pressure distorts the ZIF such that further adsorption of CO_2 is minimal. IR[138] and XPS[138] have also been found to give information regarding interactions between guest molecule and atom groups.

Since 2006, many experimental investigations have been undertaken to examine the gas ad-

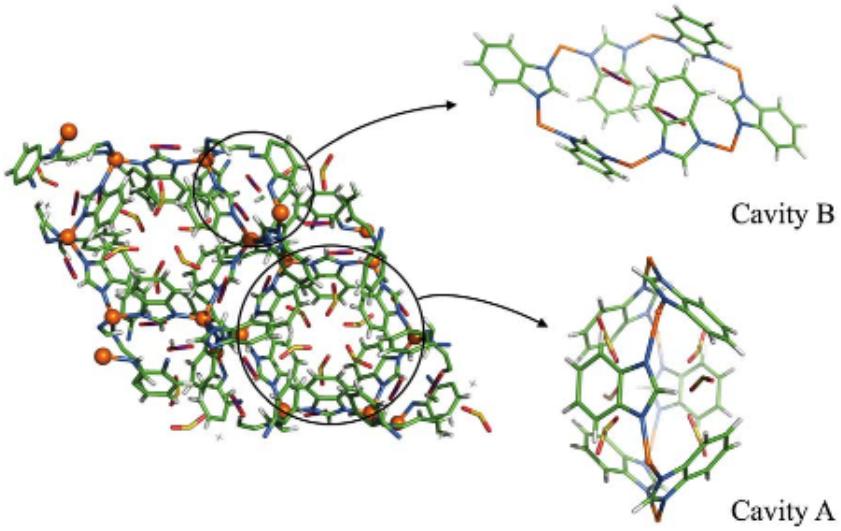

Figure 3.4: ZIF-7 Diagram. From Ref. 6.

sorption properties of ZIFs, stemming from the variety of different types afforded and stability in harsh conditions. ZIFs can be further customized through combining them with other materials to form membranes and composites. Though studied largely for its ability to capture CO_2, researchers have studied the adsorption of other species, both in gaseous and aqueous form.

3.3 Previous Molecular Simulation Work on ZIFs

In addition to experimental study, numerous simulations have been reported in the literature that examine the adsorption of ZIFs for various gases, including CO_2. Liu, et al.[140] performed preliminary work using molecular simulation (MD and GCMC) to study gas adsorption and diffusion in ZIFs, specifically ZIF-68 and ZIF-69. Molecular simulations helped Liu, et al. with two aspects of adsorption and diffusion: finding the effect of electrostatics on adsorption and mapping the adsorbate locations within the ZIF. The effect of electrostatics can be understood by examining the difference in adsorption between a ZIF with partial charges and one in which the charges are set to to zero. Rankin, et al.[141] examined this effect for ZIFs-68 and -70 and found that using charges for the ZIF contributed to overestimation of CO_2 adsorption at low pressures. In 2012,

Amrouche, et al. showed that electrostatics can account for about half of CO_2 adsorption for certain ZIFs.[142] Further mentions of the use of turning off charges will be found later in this work. Sirjoosingh, et al.[143] used simulation to map out regions where CO_2 and CO were most likely to be adsorbed in ZIFs-68 and 69. They observed that pores (the open areas in the ZIF) were more likely to be occupied than channels (the connecting linkers for pores) for CO_2 in ZIF-69, unlike the more uniform distribution in ZIF-68. The authors accounted for this by noting that the vdW radius of the -Cl functional group in ZIF-69 may make occupancy in the channels difficult. Several years ago, in a collaboration which includes the Laird group,[7] a combined experimental-theoretical investigation into the effect of functional group on CO_2 adsorption was performed. To understand this effect, five ZIFs possessing the rho topology with different functional groups were synthesized and analyzed: ZIFs-25, 71, 93, 96 and 97. ZIFs-25 and 71, the only ZIFs in the group to have symmetrical imidazolate linkers, also had the lowest adsorption, as shown in Figure 3.5. The authors' hypothesis was that the asymmetry of the other ZIFs increased the electric field in the vicinity of the functional groups, leading to increased interaction between ZIF and CO_2, because though CO_2 lacks a dipole moment, it has a large quadrupole moment. This occurs because imidazolate linkers that have symmetric functional groups cancel out the electric field near the functional groups, leading to a weaker electrostatic interaction. Many of the authors of the previously mentioned work also studied CH_4 adsorption for these five ZIFs.[144]. In this work, adsorption and diffusion selectivities for CO_2/CH_4 were examined. To complement the classical simulations performed, density functional calculations were also performed for ZIF-97, as well as an *ab-initio* molecular-dynamics(AIMD) simulation of ZIF-93. Additional work exists (for pure gases) with respect to the effect of topology[145] and functional group[146,147] for H_2. Armouche, et al.,[148] with the aid of quantitative structure-property relationship, was able to screen various ZIFs spanning three topologies for the effect of functional group on isosteric heat of adsorption for various gases.

To better mimic real-world situations (in which a ZIF could be used to separate a gas from a flue stream for example) computer simulations of gas separation prove useful, because simulations give the researcher an opportunity to examine adsorption of the ZIFs on an atomistic scale to determine

which properties affect adsorption of gases in ZIFs. Guo, et al.[149] examined four ZIFs (ZIFs-8, -10, -67, and -60) in addition to another MOF in order to gauge their selective adsorption of CH_4 in a CH_4/H_2 mixture. The authors found that topology determined what direction selectivity would go to with increased pressure. Topology was also found to influence the difference of heats of adsorption for the gases, with the ZIFs possessing the larger heat of adsorption for CH_4 with respect to H_2 also having the higher CH_4 selectivity. Finally, the authors examined the relative densities of the guest molecules occupied in the ZIFs and determined that the organic linkers played a considerably larger role than the metal atoms in which the guest molecules adsorbed. Liu and Smit examined the separations of mixtures of CO_2/N_2, CO_2/CH_4 and CH_4/N_2 for ZIFs-68 and -69.[150] In addition the effect of electrostatics and various loadings of water was looked at. CO_2 was found to have a greater selectivity with respect to the other molecules and N_2 with respect to CH_4 when charges were used in the simulation. Researchers can also examine diffusion of gas mixtures in a ZIF. One particular example, amongst others,[151–154] was the examination by Liu, et al. of CH_4/H_2 and CO_2/CH_4 mixtures in ZIF-68 and ZIF-70 and the relation of diffusion with membrane selectivity.[155]

Computer simulations can also assist researchers in studying combined systems composed partly of ZIFs. Atci and Keskin[151] looked at the adsorption of a polymer/ZIF-90 composite to examine both adsorption and selectivity of several gases. To supplement their force fields, the authors used continuum model to obtain permeabilities through the composite. Yilmaz and Keskin examined a mixed matrix membrane of various MOFs (including five ZIFs) using mathematical modeling with MD simulations providing used to provide input values for the models.[154] In Chapter 4, results will be given for the effect of topology on adsorption of CO_2 and CH_4. for ZIFs 2-4, -7, -11, -93 and -94. Additionally, the adsorption of H_2S will also be examined for ZIFs 2-4, -25 -71, -93, -96 and -97.

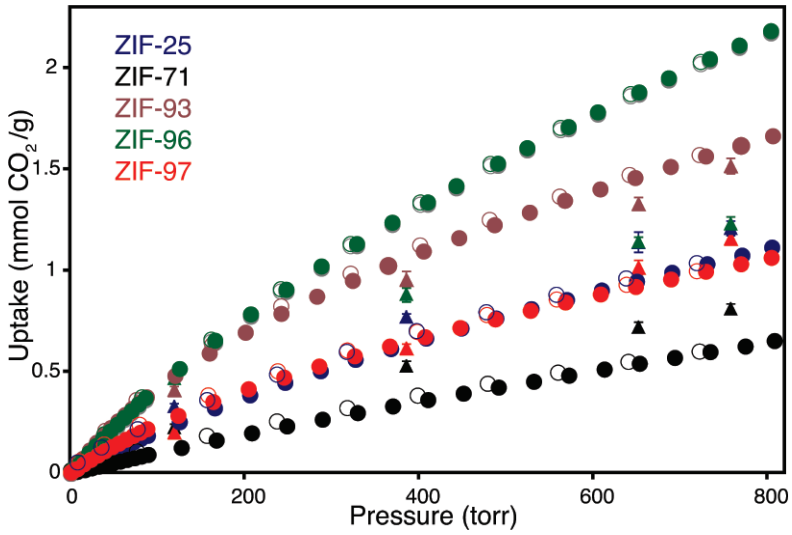

Figure 3.5: Adsorption data for several rho ZIFs with varying functionalization. Filled and empty circles indicate experimental data for adsorption and desorption, respectively, while triangles indicate simulation data[7].

3.3.1 Force Fields for ZIF Simulations

Because classical simulations require a potential to model the forces, various force fields have been under investigation for the modeling of ZIF/gas interactions. Liu, et al. used[140] the UFF (Universal Force Field)[156] to model the ZIF framework, which was later used by other authors including Battisti who used it to model ZIFs 2-10. Pérez-Pellitero, et al. created[157] a modified UFF force field for ZIFs-8 and 76, and which was later taken up by Battisti, et al.[152] to simulate ZIFs 2-10. Liu also used a modified UFF force field in the examination[150] of ZIF-69 in his work that we have noted previously. Authors have also created force fields through quantum mechanical calculations. Han, et al. used a force field based on the quantum mechanical function MP2 for 10 ZIFs and examined how the functional group affected adsorption of $H_2$for five of these ZIFs with the same topology.[146]. In 2014, Sevillano, et al. used QM to develop a set of charges that could model various imidazolate linkers[158] In addition to what was learned about adsorption, the Laird group[7], in collaboration with other groups, also determined that using the UFF potential alone to describe ZIF-96 was insufficient, because the adsorption for the simulation was lower than that

for experiment. To alleviate this problem, the OPLS-ua force field[159] was used to model the functional groups. Instead of using empirical force fields, researchers can use quantum mechanics to understand the behavior of ZIFs. As a continuation of previous work involving Laird,[160] it was noted that during the use of quantum mechanics to model adsorption of gases, accounting for van der Waals interaction was necessary to obtain the correct binding energies for the rho ZIFs previously studied. Mcdaniel, et al.[161] created an *ab-initio*-based force field to avoid problems regarding the scaling of parameters which may produce "unphysical" behavior.

When setting up a force field for a ZIF, it is often assumed that the ZIF is rigid, and researchers treat it as such during simulation. This has been shown exhaustively to not be the case in experiment[6,63,66,75,76,80,95,99,100,102,107,110,111,116,126,127,162–167] so in order to account for molecules passing through seemingly smaller windows than the guest molecules' size researchers can overcome this by factoring in flexibility. Zheng created a method to simulate ZIF-8 using a non-rigid model with point charges and found improved accuracy for CO_2 diffusion using the flexible model.[168] Haldoupis, et al. used AIMD to generate positions of the atoms in a flexible ZIF, which negated the need to account for vibrations for diffusion calculations.[169] Additional work exists regarding various methods of incorporating flexibility in ZIF structure.[108,115,152–154,165,168,170–172] . For the simulations explored in the next chapter, however, most of the ZIFs we will investigate have fairly strong rigidity (with the exceptions of ZIFs-7 and 11, thus for the systems we investigate in the next chapter, we will allow the ZIFs to remain rigid.

In addition to classical force fields, we note that force fields based on quantum mechanical calculations of the energy can also be employed to examine various properties of ZIFs. Hou and Li[173] used a mixed quantum/classical technique known as ONIOM to examine CO_2 adsorption for the previously mentioned group of ZIFs -68 and -69. Their calculations show Lewis Acid base interactions between CO_2 and CO with the ZIFs at high pressures cause the small pores to be blocked. DFT has been used to examine the binding of CO_2 to various linkers, because as was noted, the linker plays a critical part in adsorption. DFT was also used to determine the effect of metal ion for H_2 adsorption of ZIF-23.[174] In addition to examining specific configurations of a

system using quantum mechanics (QM), it has been shown that MD simulations can be performed using QM to model part of the interaction between the ZIF and guest molecules.[175] Adsorption can also be modeled in a ZIF by using coarse grained models, which account for less detail than the classical simulations mentioned earlier, but can apply for systems that are larger than can be handled by such classical simulations.[176,177]

Over the past decade, many research groups have added knowledge regarding ZIFs through experiment and computer simulations. ZIFs have become highly sought after stemming from their superb ability to capture gases harmful to the environment. These systems may be customized with regard to topology, functional group and metal ion. For computer simulations, various levels of theory have been used to examine adsorption, from course grained models to quantum-level. Ideally, ZIFs would be available in every type of topology that a zeolite can assume, but the sheer number of topologies theoretically possible for a zeolite[1] make that unlikely in the near future. Work also needs to be done to examine use of ZIFs on an industrial scale.

Chapter 4

Results for Simulations of Gas Adsorption in ZIFs

4.1 Introduction

As noted in the previous chapter, ZIFs can be distinguished from one another by their topology, functional group(s), and metal atom(s). To isolate the effect of one of these properties on the adsorption of gases, adsorption behavior of ZIFs can be compared for ZIFs that differ only in the property of interest. In this chapter, we examine the effect of varying the topology on the adsorption of CO_2 and CH_4. We examine three sets of ZIFs: 2-4, 7/11 and 93/94. The members of each of the sets have identical functional groups and metal atom, but differ in topology. We measure the adsorption with respect to adsorption and plot these points in the form of an *adsorption isotherm* (constant-temperature). Density maps have been created for the ZIFs at two pressures (1.01 bar and 40.0 bar) to determine the preferential adsorption sites of CO_2 and CH_4 within the ZIF. Creating these maps also provides atomistic information to understand our isotherms. Because computer simulations allow us to determine the effect of a single variable, we can turn off the charges for the simulation to examine the effect of electrostatics on CO_2 adsorption (not needed for CH_4 because there are no charges for the force field model used). We will also present some simulation data on

the adsorption of H_2S for the set ZIF-25, -71, -93, -96 and -97. In this set, all ZIFs have the same topology (RHO), but different functional groups. This allows us to assess the effect of functional group. We have adsorption data for H_2S adsorption for ZIFs 2-4, to look at the effect of topology. For this set of ZIFs, we also calculate the effect electrostatics has on adsorption. We also examine the effect of electrostatics for ZIFs 2-4 with respect to adsorption of the toxic gas H_2S.

4.2 CO_2 and CH_4 Adsorption Simulation

To explore the effect of topology on adsorption, three sets of ZIFs were chosen, each set having the same functional group, ZIF-7 and -11, ZIF-93 and -94, and ZIFs 2-4. This research was done in collaboration with Professor Yao Houndonougbo, former postdoctoral researcher Ning He and myself. ZIFs 7/11 have the bIM (benzimidazolate) functional group, 93/94 have the almeIM (4-aldemetylimidazolate), and the last have the Im (imidazolate) group. Figure 4.2 shows the functional groups of the ZIFs used for this study and Figure 4.1 shows the topologies.

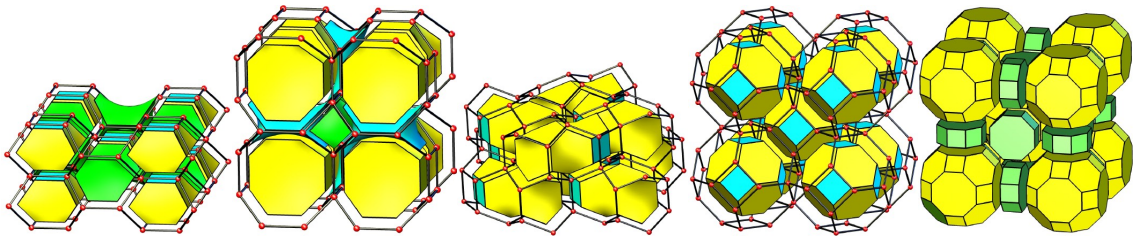

Figure 4.1: Topologies for ZIFs used in work: CRB (ZIF-2), DFT (ZIF-3), CAG (ZIF-4), SOD (ZIF-7, -94) , RHO (ZIF-11, -93). Images from Ref. 8.

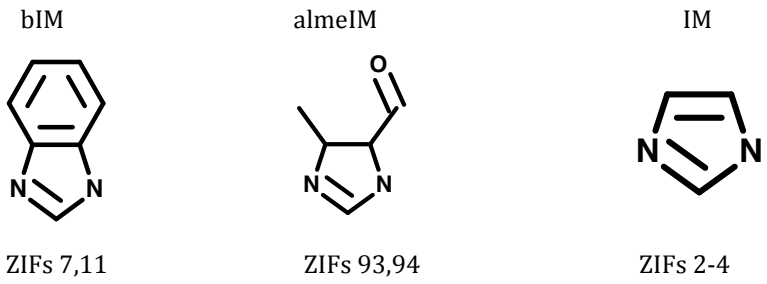

Figure 4.2: Functional groups for ZIF groups (7,11), (93,94), and (2-4).

The molecular simulation program used for this project was "Monte Carlo for Complex Chemical Systems (MCCCS) Towhee". Grand Canonical Monte Carlo simulations were performed in which the number of molecules adsorbed in the ZIF was allowed to vary. For simplification, all ZIFs were modeled as rigid. *NPT* simulations were performed initially to calculate the chemical potential at 100 kPa for CO_2, $CH_4$and N_2 using the Peng-Robinson Equation of State[178]. A simulation at 101.0 kPa was used to calculate the chemical potential for H_2S at that pressure, This chemical potential served as the initial input for the following equation

$$\mu_2 = \mu_1 + RT \ln \frac{P_2}{P_1}. \tag{4.1}$$

This equation assumes that the system is ideal, which is valid for our purposes, because we only examined systems at low pressure (< 101.0 kPa=1 atm). For N_2,we later used the chemical potential at 6 kPa(calculated using the Peng-Robinson Equation of State) as input for Eq. 4.1 to calculate chemical potentials for additional, lower pressures. For CO_2 and CH_4, pressures from 5.09 kPa to 4000 kPa were used as input to obtain chemical potentials at the corresponding pressures. BET surface area measurements[179] (named after Brunauer, Emmett and Teller) has been employed for decades to calculate the surface area. The method relies on correlating the amount of N_2 adsorbed in a system with the surface area of the system. This correlation is based on the assumption that N_2 adsorbs on a system in the form of a monolayer. We use a form of this method developed for periodic systems by Snurr and Walton.[180] All of the simulations were done at 298 K, except for the N_2 BET simulations, which were done at 77 K. In addition to calculating the adsorption of CO_2 and CH_4, several simulations were performed for ZIF-7 and ZIF-11 using N_2 to determine the BET surface area.

We used a combination of force fields to model the various molecules simulated. All non-bonded van der Waals interactions were based on the Lennard-Jones 12-6 potential

$$U = 4\varepsilon \left(\left(\frac{\sigma}{r} \right)^{12} - \left(\frac{\sigma}{r} \right)^{6} \right) \tag{4.2}$$

where σ and ε are the Lennard-Jones parameters for each defined "atom" (though in united atom

models, alkyl hydrogens are considered part of another atom). Charges were assigned using the program REPEAT,[181] which was designed to calculate the charges for atoms in a periodic system using input from electronic structure calculations. The electrostatic potential for the system is used as a reference for the atomic charges of the system, and the atomic charges are adjusted so that the potential created by the atoms is similar to the calculated potential. The potential is dependent on the geometry of the system, thus we use a fixed geometry for the ZIF as a simplifying assumption. This assumption should not significantly affect our results because most of the ZIFs under examination are relatively rigid in experiment.

Interactions between unlike atoms were constructed using Lorentz-Berthelot mixing, Eq. 2.29. We used the EPM2[182] model for CO_2, in which each atom had its own LJ and charge term. For CH_4, the united atom model of Verlet was used[183], with only the carbon assigned Lennard-Jones parameters. For modeling H_2S, we used the potential described in Ref. 184. For the simulations of CO_2 and CH_4 adsorption, we used the UFF force field[156] to model the atoms in the imidazolate ring for ZIF-93 and ZIF-94. For the other atoms in ZIFs-93 and 94, we use OPLS-1996.[185] We also use the UFF to model the zinc and nitrogen atoms in the imidazolate ring of ZIFs 2-4,7 and 11. For the other atoms in ZIFs 2-4, 7 and 11, we use OPLS-2001[186]. For modeling adsorption of H_2S into ZIFs 25, 71, 93, 96 and 97, we used a force field courtesy of Ref. 187. We used Ref. 188 to model N_2. For the adsorption on H_2S in ZIFs 2-4, we used the same force field as for CO_2 and CH_4 adsorption. We used the code HOLE[9] to calculate the pore distributions of ZIFs 2-4, -7, -11, -93 and -94, which are shown in Figures 4.6-4.8. HOLE calculates the pore diameters of a given system by determining the maximum size of a sphere that does not overlap with the vdW volume of the system being measured. This occurs along evenly sized increments along a given axis.

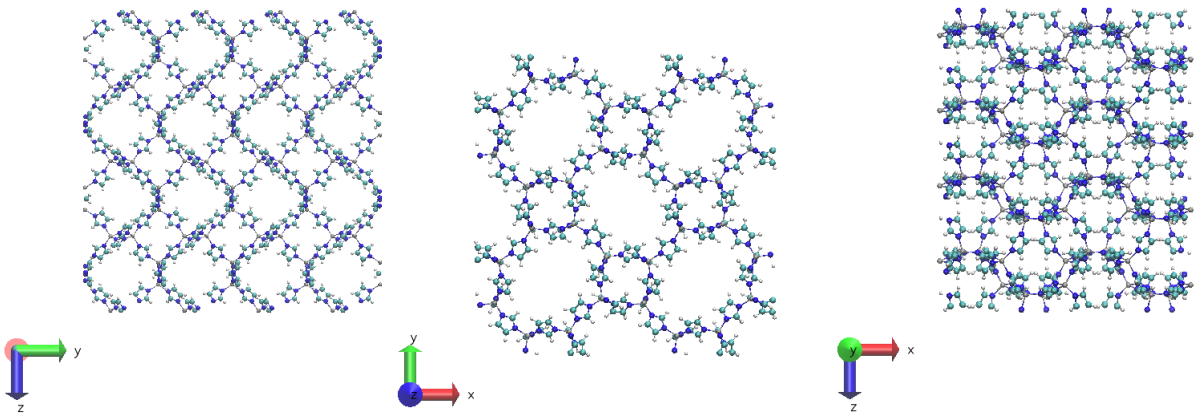

Figure 4.3: Images of ZIF-2, -3 and -4.

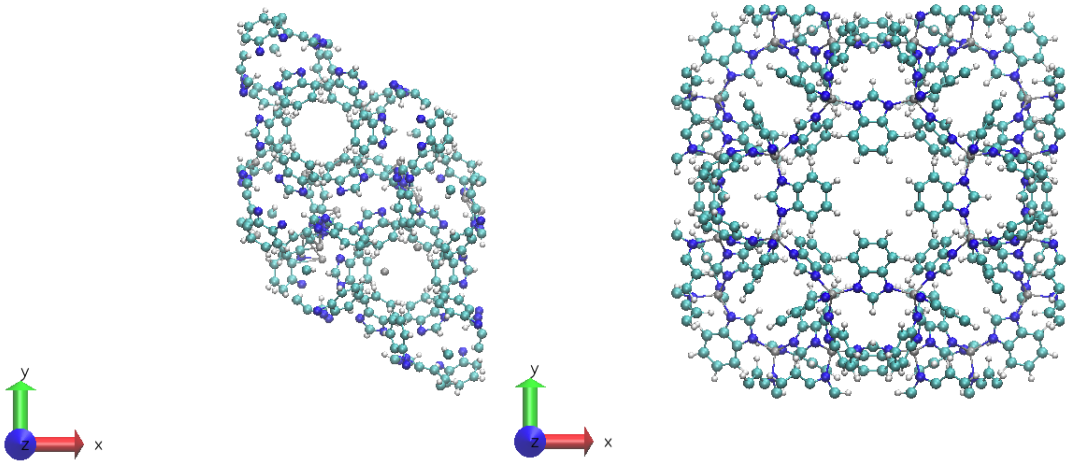

Figure 4.4: Images of ZIF-7 and -11.

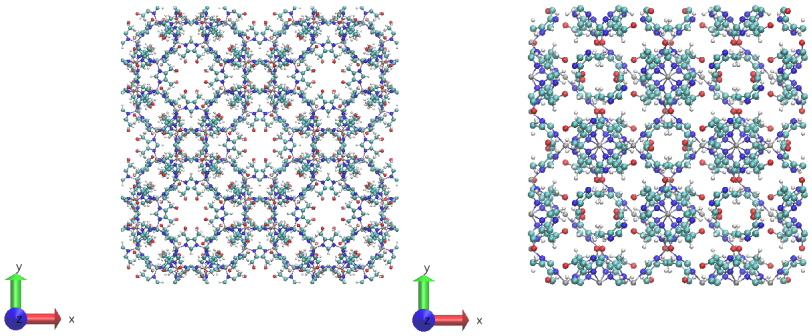

Figure 4.5: Images of ZIF-93 and -94.

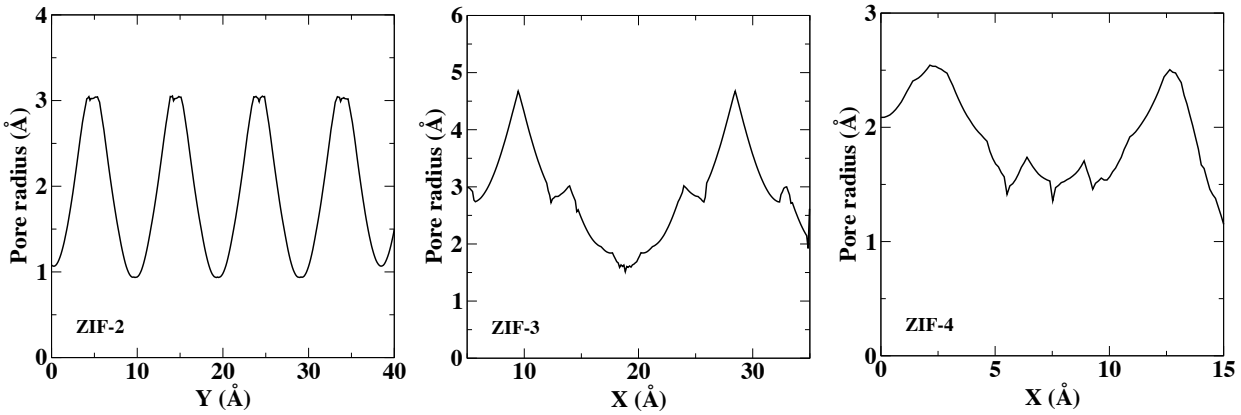

Figure 4.6: Pore size distributions of ZIFs 2-4. Data obtained using Ref. 9.

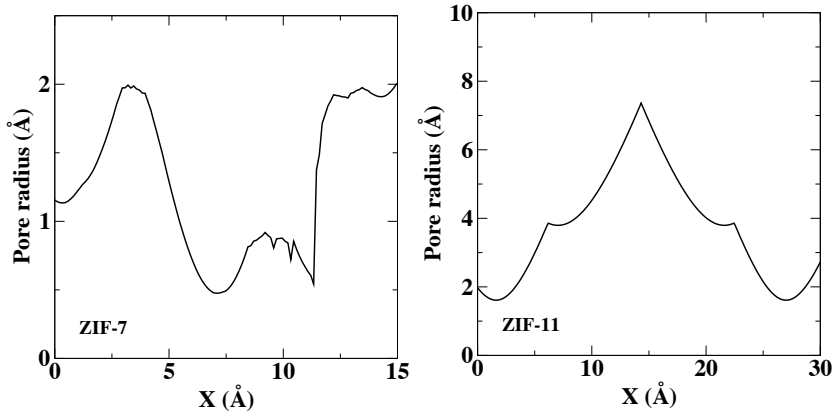

Figure 4.7: Pore size distributions of ZIFs-7, -11. Data obtained using Ref. 9.

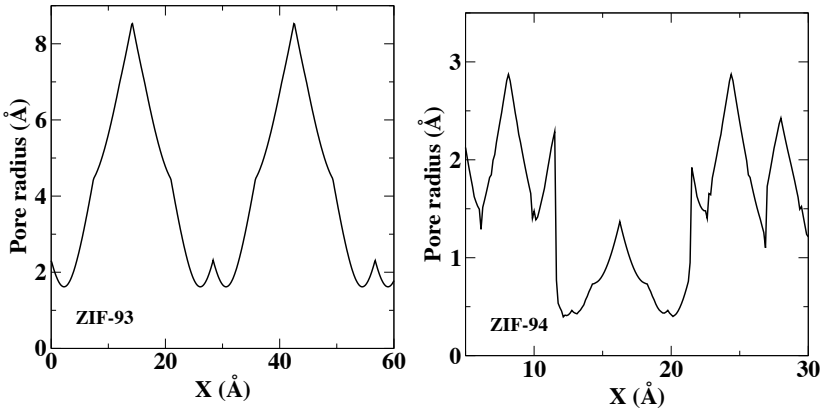

Figure 4.8: Pore size distributions of ZIF-93, -94. Data obtained using Ref. 9.

Simulations from 5.09 kPa to 4000 kPa have been performed for CO_2 and CH_4 adsorption

and compared with experiment when experimental results are available. To better illustrate the behavior at the various pressures, separate plots of ZIFs at low pressure and high pressure have been made. To maintain consistency, all of our comparisons of pure gas between simulation and experiment are made at 1 atm (with estimations made for experiment because experimental data for this exact pressure may not be in the experimental data of our collaborators). All percentages following are the relative discrepancy between our results and experiment, calculated using the following equation

$$Error\,(\%) = \frac{|Exper_{1\text{atm}} - Simul_{1\text{atm}}|}{Exper_{1\text{atm}}} * 100 \tag{4.3}$$

As shown in Figure 4.9, the simulated low-pressure isotherm of ZIF-11 has reasonable agreement with experiment (21 %) . The low-pressure adsorption isotherm for ZIF-7 is qualitatively different than the desorption isotherm. This discrepancy can be explained by referring to Ref. 189, in which the authors demonstrate that ZIF-7 changes structure when exposed to gas molecules. The experimental results from our collaborators exhibit significant hysteresis for ZIF-7 at low pressures for both gases. Desorption isotherms are included in plots where hysteresis occurs. This hysteresis indicates some issues with the ZIF which may need to be further studied. This behavior can also explain the significant difference between the simulated and experimental adsorption for ZIF-7 (34 %). Despite this discrepancy, we note that agreement with experiment is good at the lowest pressures. In Figure 4.10 ZIFs-93 and 94 show excellent agreement with experiment (9 % and 5 %, respectively), thus lending credibility to the force fields employed for these ZIFs. As shown in Figure 4.11, we find good agreement between experiment and simulation for ZIF-4 at 1 atm (9 %), thus we can use our force field for other ZIFs possessing the same functional group (in our case, ZIFs-2 and 3). We also observe close agreement at high pressures as shown by Figures 4.12 and 4.13, with the exception of ZIF-7. For CH_4, ZIF-7 has a considerably large discrepancy with respect to adsorption (108 %) while for ZIF-11 it is more accurate (37 %). For ZIFs-93 and 94, we find differences of 57 % and 10 %. ZIF-4 is found to have excellent agreement with experiment for CH_4 (<1 %) As shown, for most of our ZIFs our accuracy is significantly worse for CH_4 than for CO_2 adsorption.

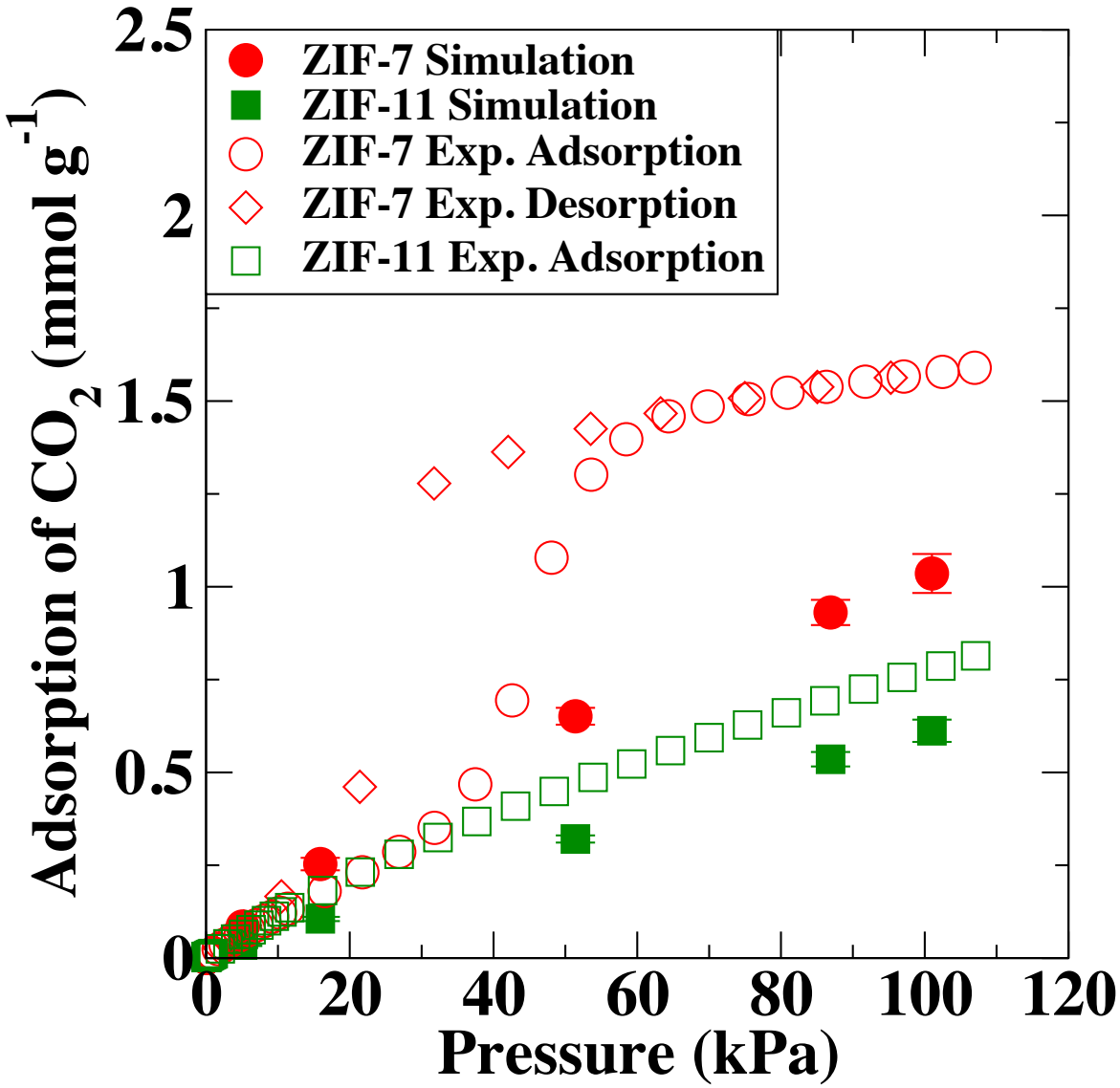

Figure 4.9: Results of GCMC simulations for CO_2 adsorption of ZIF-7 and -11 up to 101.0 kPa. Filled symbols denote simulation data and open symbols denote experimental data. Experimental results from Ref. 10.

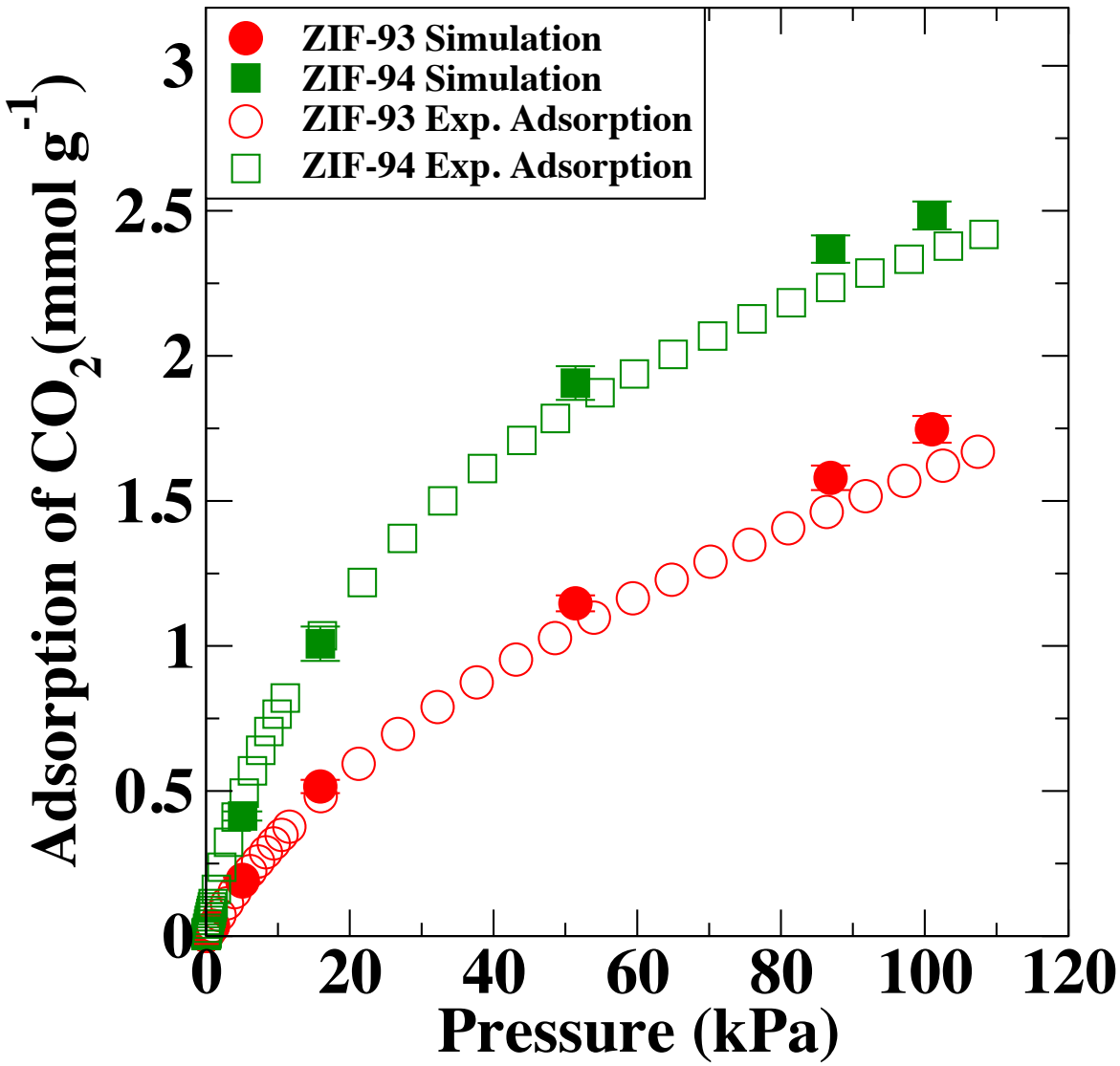

Figure 4.10: Results of GCMC simulations for CO_2 adsorption of ZIF-93 and -94 up to 101.0 kPa. Filled symbols denote simulation data and open symbols denote experimental data. Experimental results from Ref. 10.

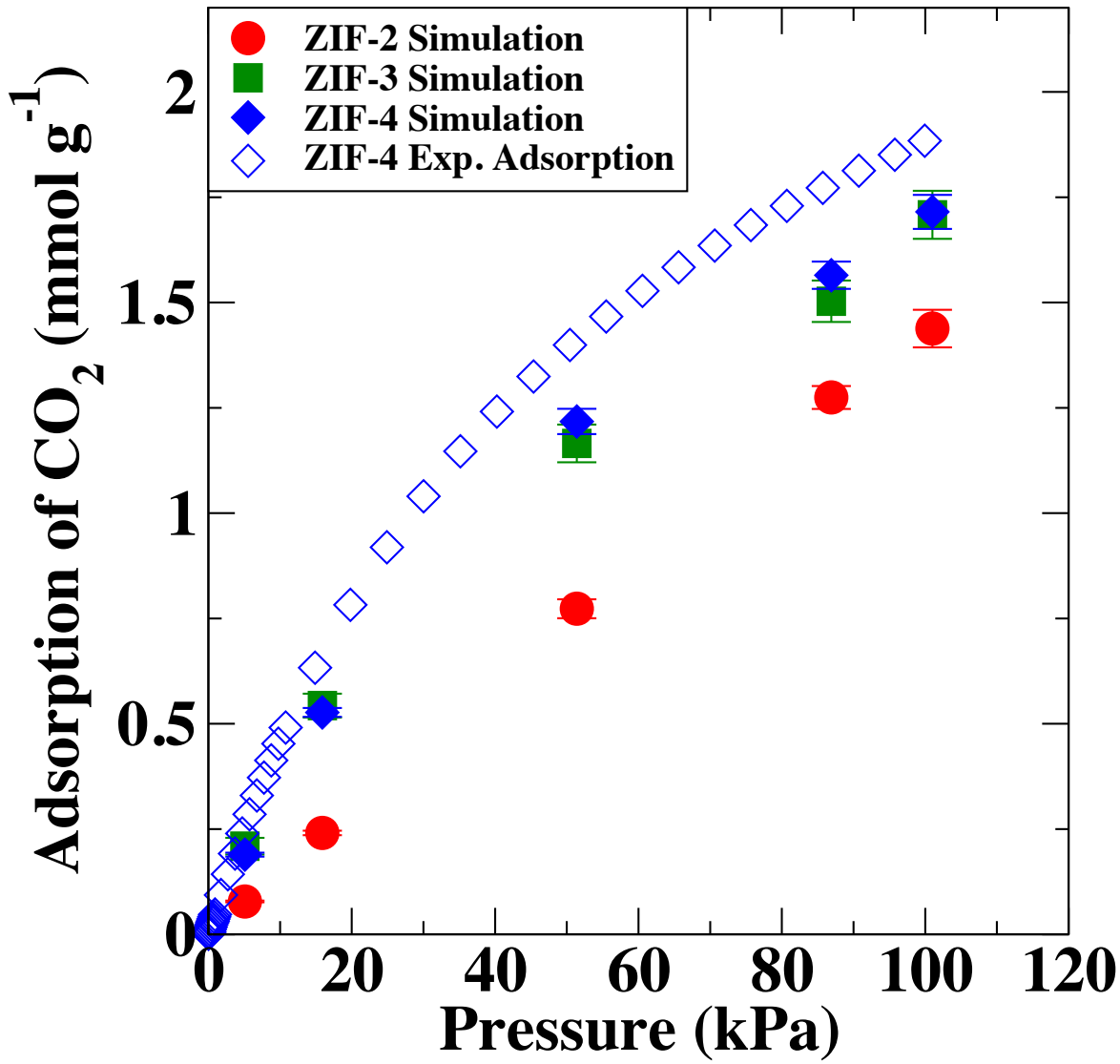

Figure 4.11: Results of GCMC simulations for CO_2 adsorption of ZIFs 2-4 up to 101.0 kPa. Filled symbols denote simulation data and open symbols denote experimental data. Experimental results courtesy of Ref. 11.

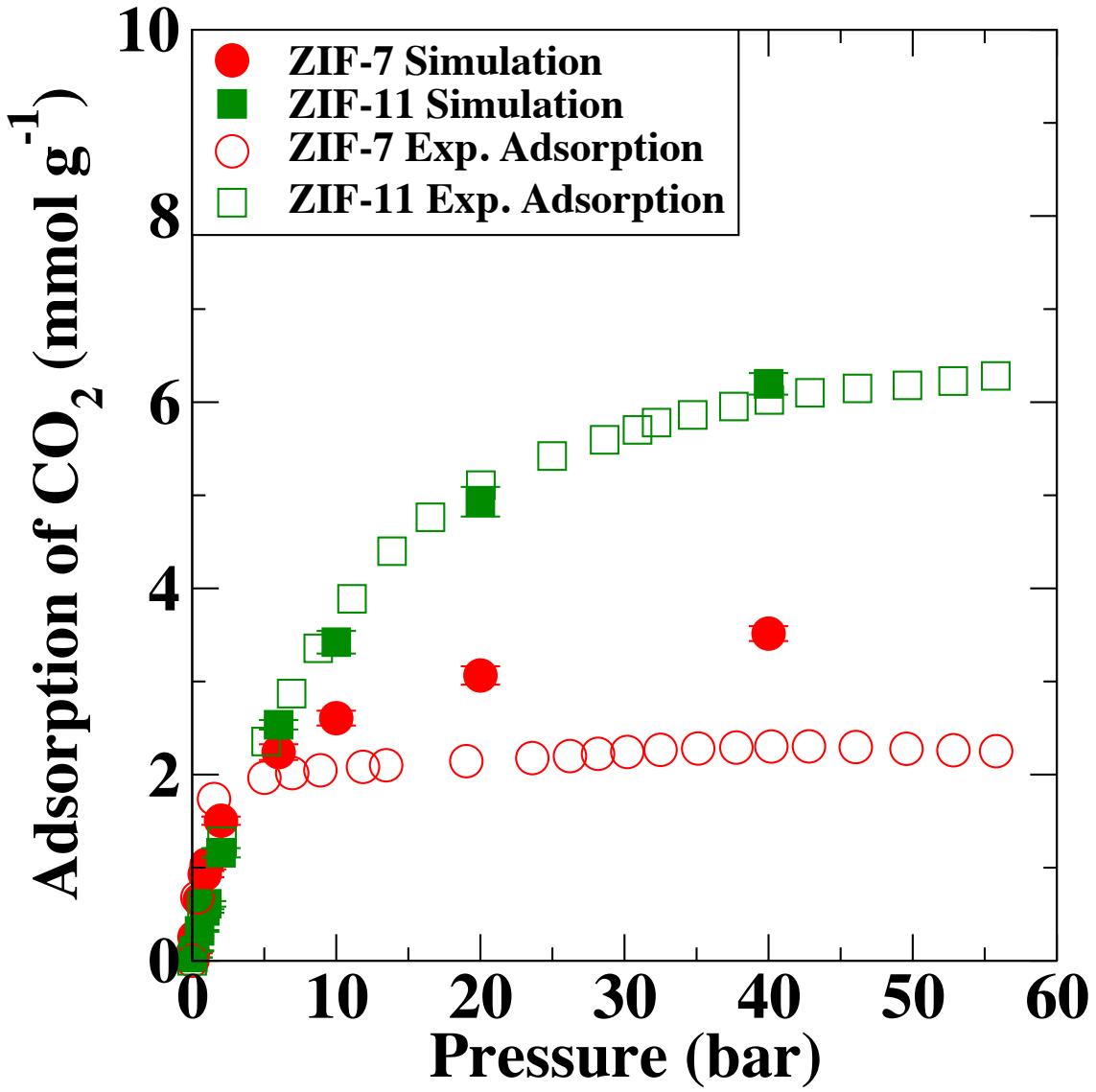

Figure 4.12: Results of GCMC simulations for CO_2 adsorption of ZIF-7 and -11 up to 40.0 bar. Filled symbols denote simulation data and open symbols denote experimental data. Experimental results from Ref. 10.

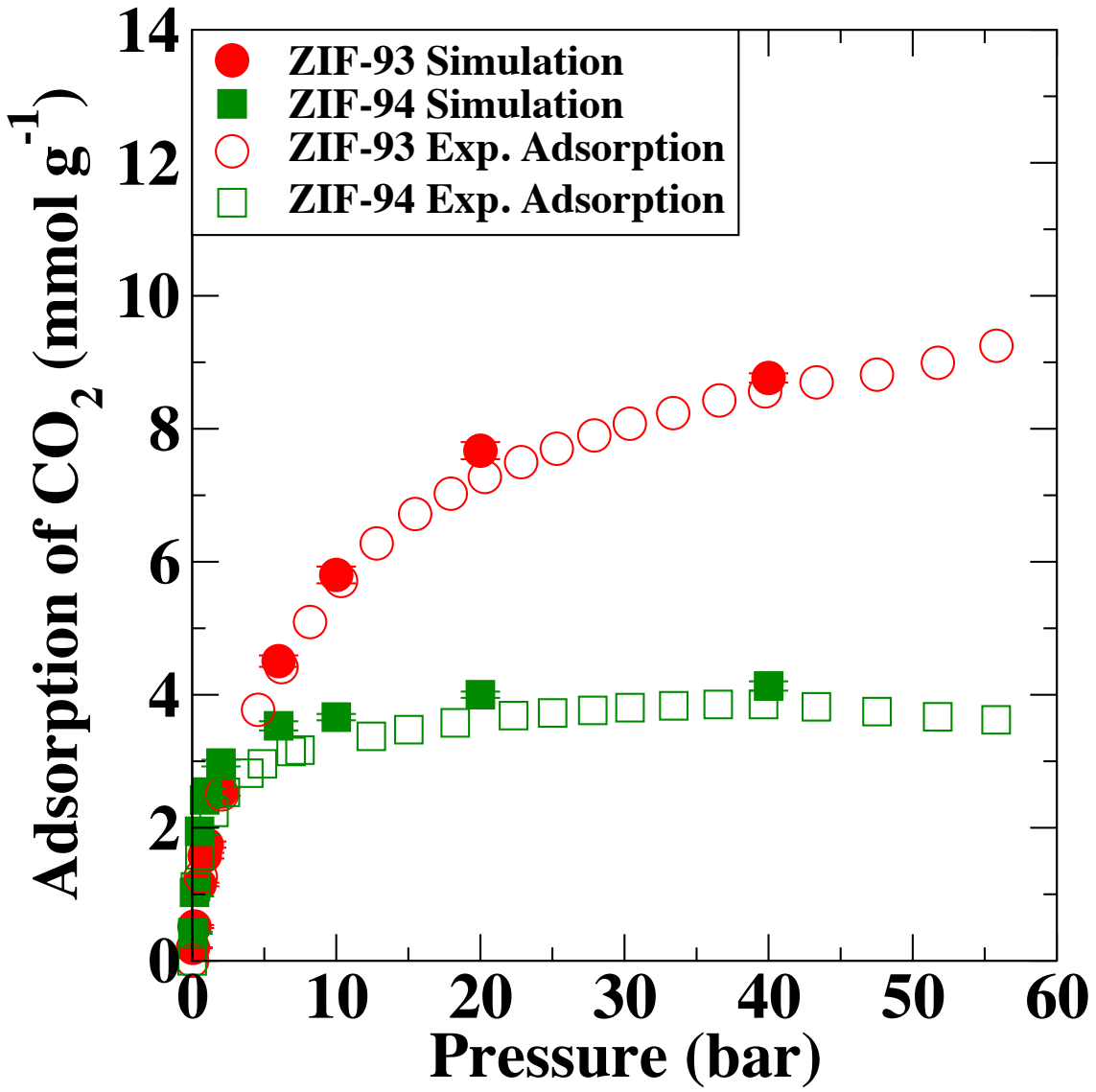

Figure 4.13: Results of GCMC simulations for CO_2 adsorption of ZIF-93 and -94 up to 40.0 bar. Filled symbols denote simulation data and open symbols denote experimental data. Experimental results from Ref. 10.

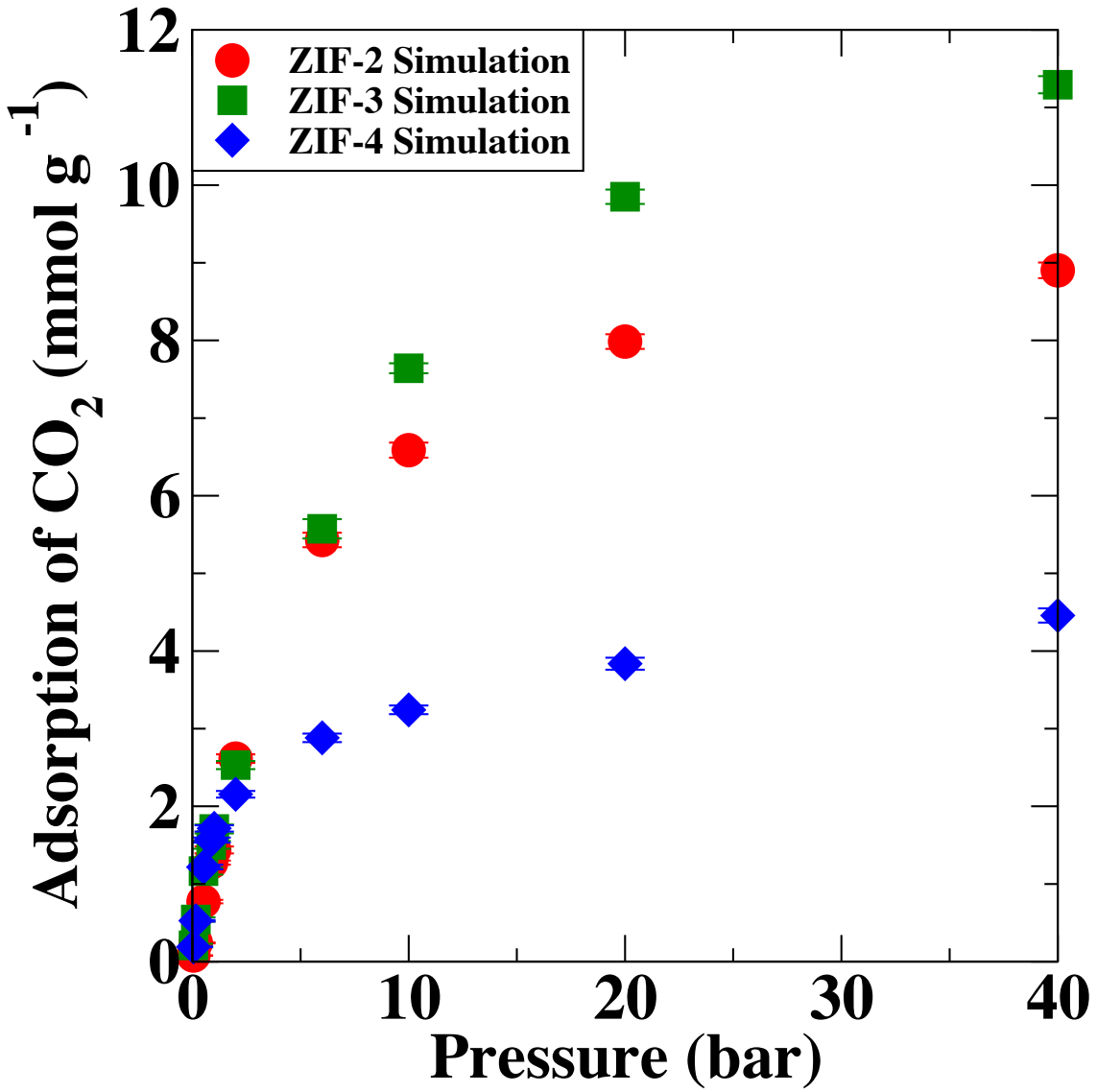

Figure 4.14: Results of GCMC simulations for CO_2 adsorption of ZIFs 2-4 up to 40.0 bar. Filled symbols denote simulation data and open symbols denote experimental data. Experimental results courtesy of Ref. 11.

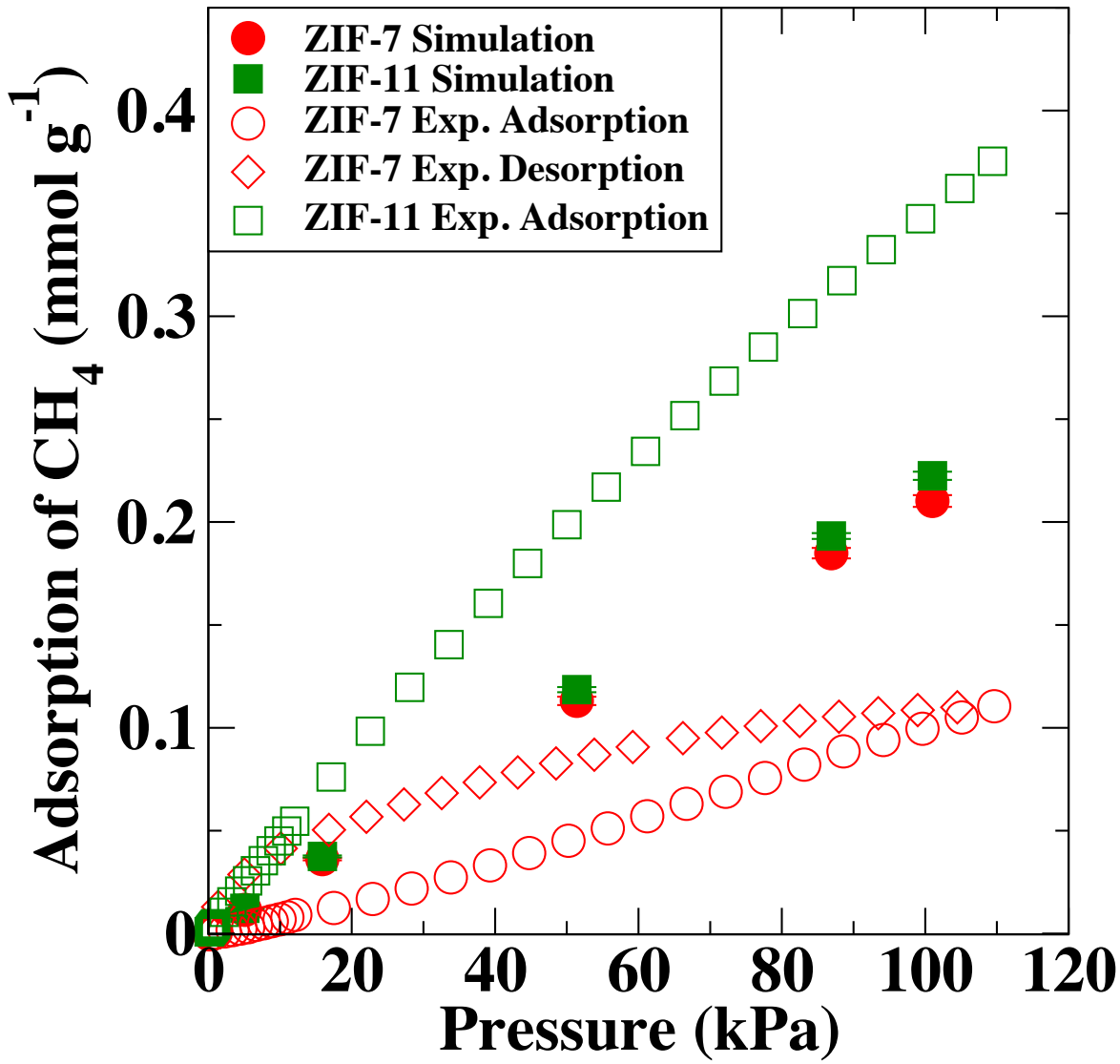

Figure 4.15: Results of GCMC simulations for CH_4 adsorption of ZIF-7 and -11 up to 101.0 kPa. Filled symbols denote simulation data and open symbols denote experimental data. Experimental results from Ref. 11.

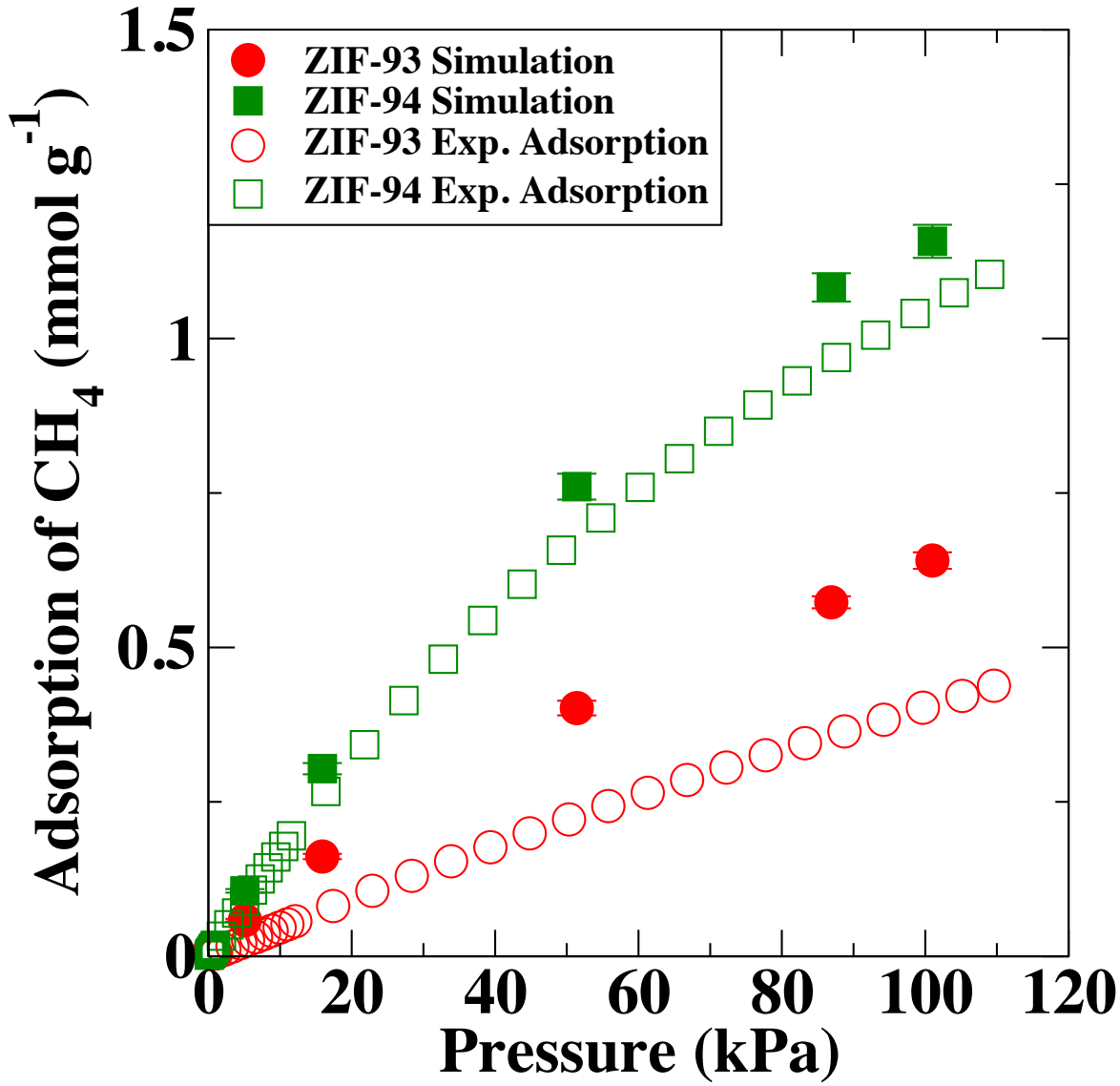

Figure 4.16: Results of GCMC simulations for CH_4 adsorption of ZIF-93 and -94 up to 101.0 kPa. Filled symbols denote simulation data and open symbols denote experimental data. Experimental results courtesy of Ref. 11.

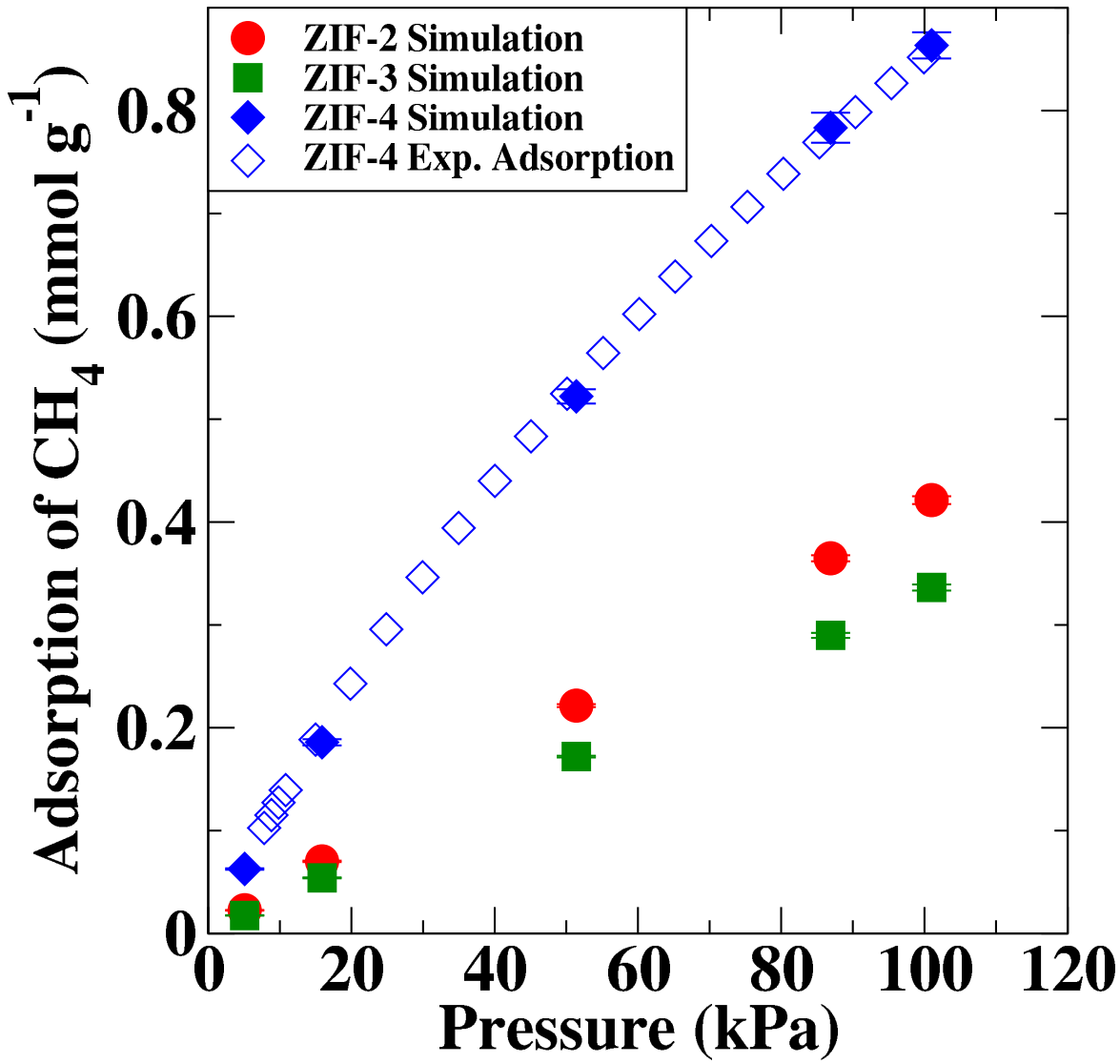

Figure 4.17: Results of GCMC simulations for CH_4 adsorption of ZIFs 2-4 up to 101.0 kPa. Filled symbols denote simulation data and open symbols denote experimental data. Experimental results courtesy of Ref. 11.

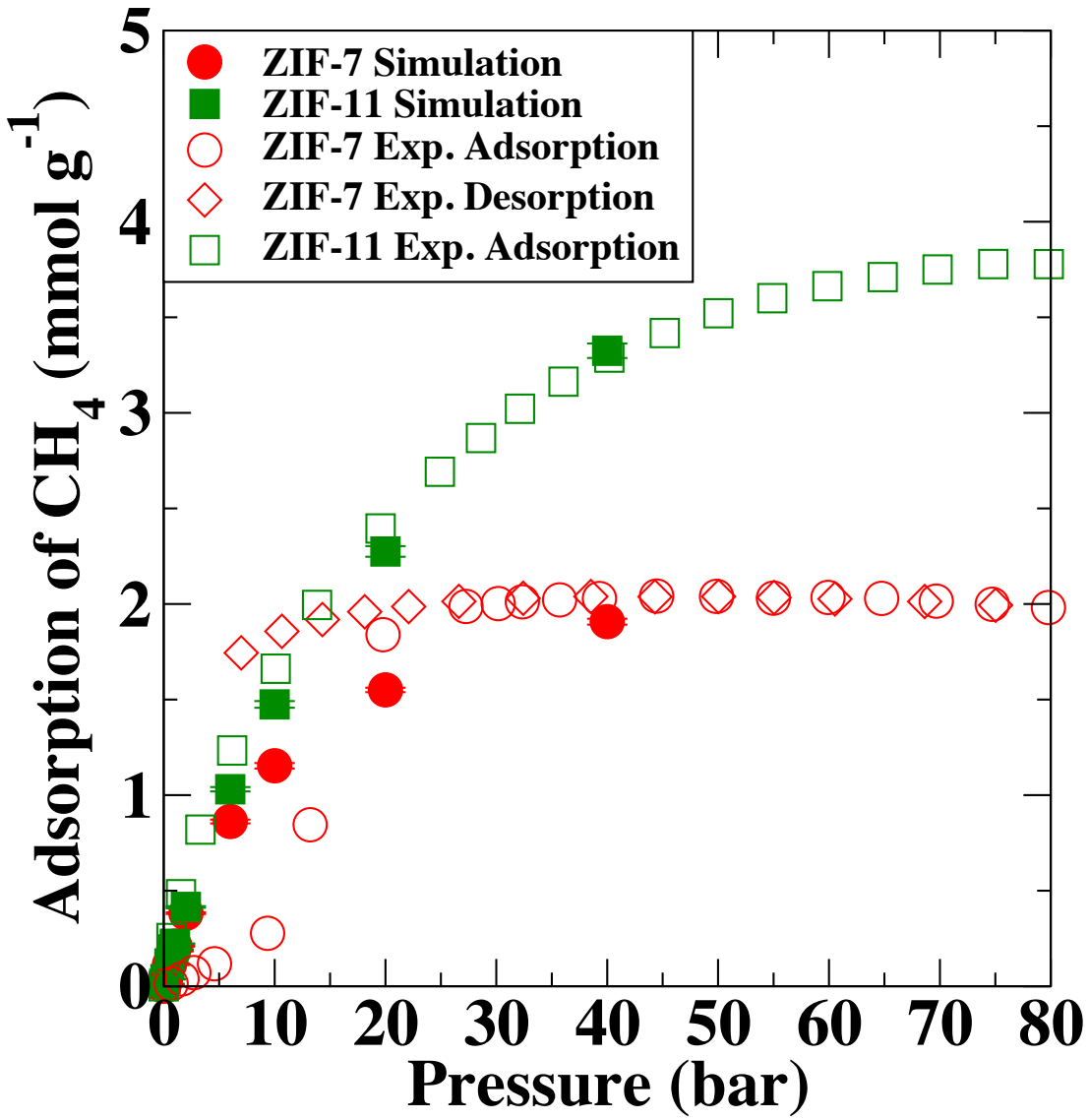

Figure 4.18: Results of GCMC simulations for CH_4 adsorption of ZIF-7 and -11 up to 40.0 bar. Filled symbols denote simulation data and open symbols denote experimental data. Experimental results courtesy of Ref. 11.

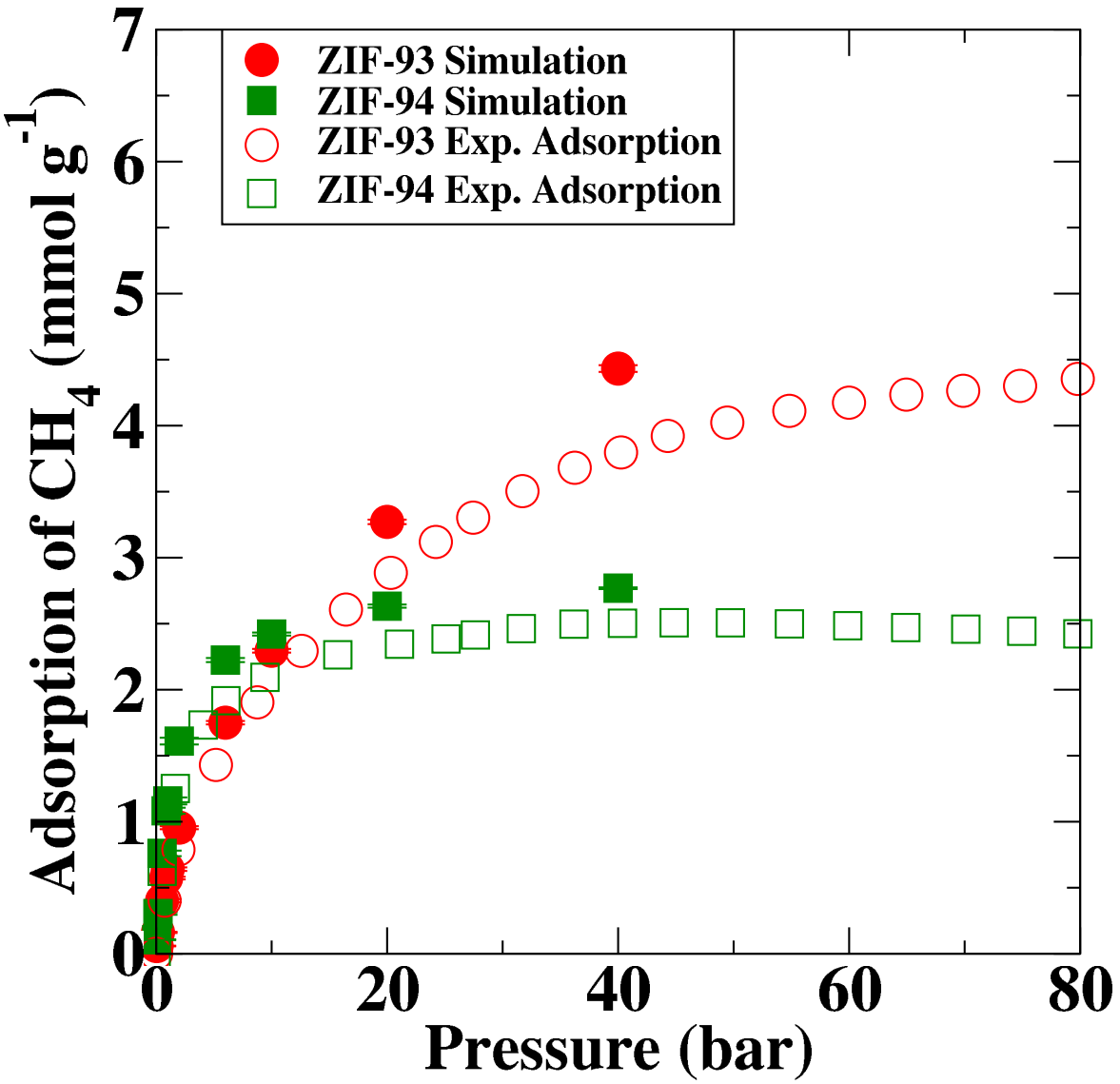

Figure 4.19: Results of GCMC simulations for CH_4 adsorption of ZIF-93 and -94 up to 40.0 bar. Filled symbols denote simulation data and open symbols denote experimental data. Experimental results courtesy of Ref. 11.

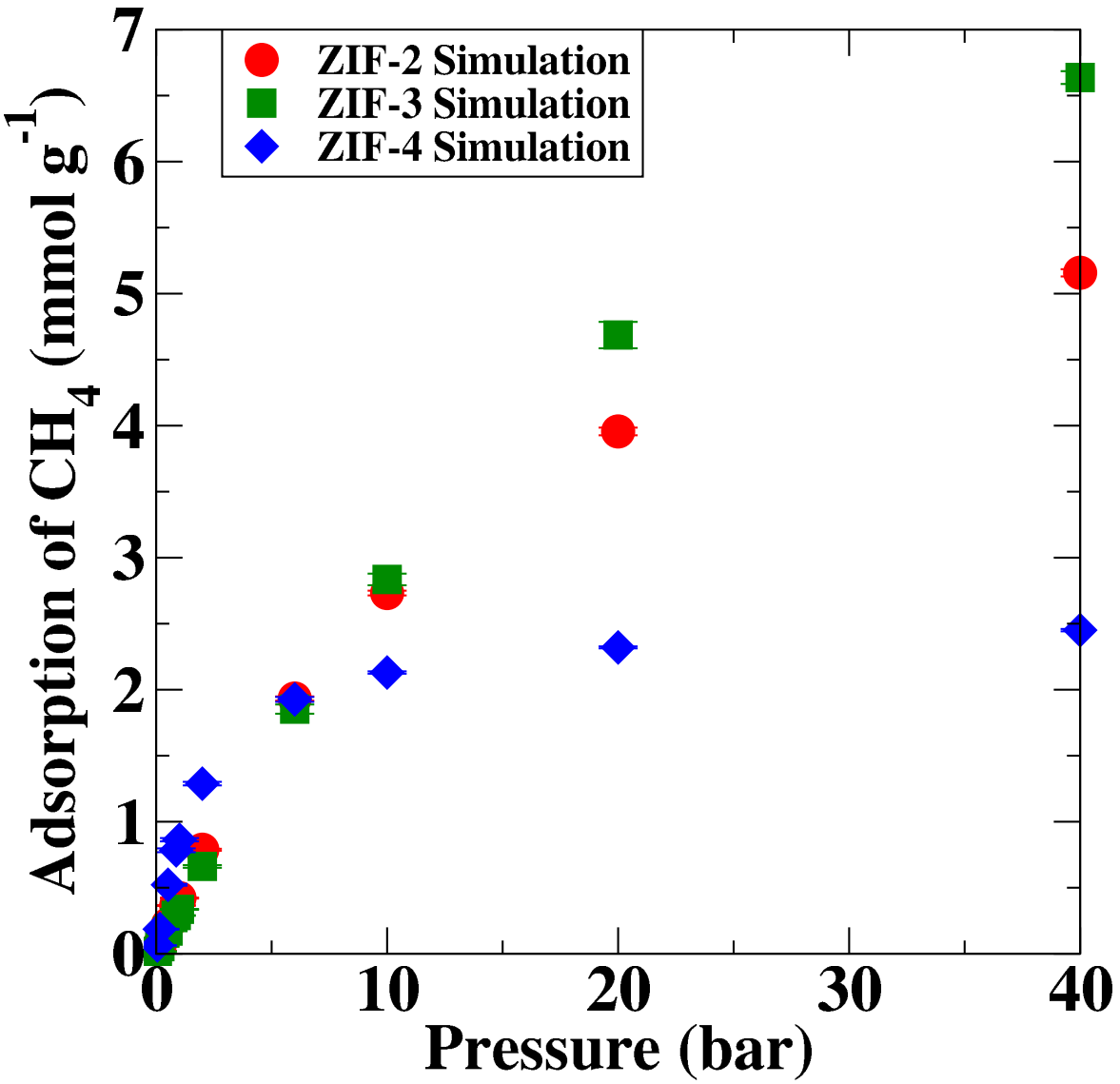

Figure 4.20: Results of GCMC simulations for CH_4 adsorption of ZIFs 2-4 up to 40.0 bar. Filled symbols denote simulation data.

Both experiment and simulation demonstrate that the ZIFs have qualitatively different behavior at low and high pressures for a majority of our results with respect to adsorption. For ZIFs-7 and -11, ZIF-7 adsorbs more CO_2 molecules than ZIF-11, while the same is true for ZIF-94 with respect

to ZIF-93. We observe that the trends are reversed at higher pressure, leading to the conclusion more than one factor determines the adsorption behavior of a ZIF. Because ZIF-11 and ZIF-93 have larger pore volumes than ZIF-7 and ZIF-94, respectively as shown in Table 4.1, we hypothesized that non-bonding interactions predominate at lower pressure, while pore size controls adsorption at higher pressures. For ZIFs 2-4, the trends in adsorption with respect to pressure are harder to reconcile with what we know about these systems, but we can find possible explanations for these anomalies. At low pressure, we find that ZIFs-3 and -4 have isotherms that are very nearly identical, while ZIF-2 has lower adsorptions. For CH_4, ZIF-11 not only exceeds ZIF-7 with respect to adsorption at high pressure, as was the case for CO_2 adsorption, ZIF-11 also has about the same adsorption of CH_4 as ZIF-7 does. In contrast, at low pressure ZIF-93 and -94 have the same qualitative relationship for adsorption. We observe no qualitative difference in trends at high pressure with respect to our data at CO_2. This demonstrates that the functional group of the system has little contribution toward adsorption at higher pressure.

ZIF	topology	pore volume (cm^3 g^{-1})
2	CRB	0.597
3	DFT	0.646
4	CAG	0.297
7	SOD	0.214
11	RHO	0.445
93	RHO	0.464
94	SOD	0.229

Table 4.1: Structural characterization of ZIFs. Calculated using program PLATON. PLATON forms a grid encompassing the ZIF and all points in the grid that are within 1.2 of the vdW volume of the system are counted as contributions to the pore volume[17].

One of the key advantages of employing simulations is the ability to determine the contribution of the electrostatics of the ZIF with respect to gas adsorption. This gives us the ability to test our hypothesis regarding adsorption behavior at varying pressures. For our purposes, we will focus only on CO_2 adsorption, because as stated earlier there are no charges on CH_4 in our model. The

following formula is used

$$Contribution = \left(1 - \frac{Simulation_{\text{nocharge}}}{Simulation_{\text{charge}}}\right) * 100. \tag{4.4}$$

For ZIFs 2/3/4, 7/11, and 93/94, as pressure increases, the contribution from charge decreases. The contribution decreases because, as the pressure increases, more CO_2 molecules adsorb in the system and steric constraints play a larger part in adsorption compared to electrostatics. From an analysis of these three groups of ZIFs we observe that for ZIFs with the same functional group, the structure with the largest pore volume in the set also tends to have the lower contribution to adsorption (with respect to the other ZIFs in the group) from charge at the highest pressure. ZIF-3 has a larger contribution from charge than ZIFs 2 or 4, but this larger contribution may arise from the smaller pores of ZIF-3 (as seen in Fig. 4.6) that would predominately contribute toward adsorption at lower pressures.

In addition to examining the effect of charge, computer simulations can also be used to obtain structural information that is often difficult to access through experiment. Structural information can be obtained by plotting density maps of the center-of-mass of the molecules in the ZIFs. We plotted density of the 'C' atom of CO_2 from the simulation to determine where this molecule preferentially adsorbs, at both 1.01 bar and 40.0 bar. In Figure 4.25, we observe that the main adsorption sites for ZIF-93 are isolated pockets, while CO_2 molecules take up much more space in ZIF-94. At 40 bar, the pores of ZIF-93 are saturated with CO_2, providing a stark contrast to the snapshot from lower pressure. ZIF-94 shows a much less striking contrast. This behavior of ZIF-94 can be explained by noting the larger pores ZIF-93 has, as shown in Fig. 4.8. The larger pores of ZIF-93 allow for saturation to occur at larger pressures. We can also observe the same qualitative behavior for ZIFs-7 and -11 and ZIFs-2-4, in Figures 4.24 and 4.26, respectively. The map at lower pressure of ZIF-3 can also explain why adsorption for ZIF-2 was highest at low pressures, even though ZIF-3 has the largest pore volume of the three. As shown in Figure 4.26, ZIF-3 possesses both very large and very small pores. Adsorption in ZIF-3 is significant at atmospheric pressure, most likely arising from the close interactions the guest molecules have

with the framework. Figure 4.26 corroborates this hypothesis because we observe CO_2 molecules prefer to adsorb in the smaller pores at 1.01 bar. Because ZIF-4 has a total small pore volume, our snapshots provide additional credence toward our explanation of the adsorption behavior of the ZIFs.

To understand our adsorption isotherms for CH_4, we also constructed density maps for CH_4 for all of the ZIFs that we created for CO_2 adsorption. In figure 4.28 at high pressure the pores of ZIF-93 are not filled, unlike the case for CO_2. This can also be found for ZIF-11 in Figure 4.27. We note that for ZIF-3, the smaller pores that were partially occupied by CO_2 are almost empty when CH_4 act as the guest molecules. We propose that an explanation for this arises from the large LJ diameter of CH_4, because unlike CO_2, the molecule has a spherical LJ diameter (3.73 Å) which is smaller than that of the LJ diameter for CO_2 (8.823 Å) along its longer axis, but larger that the LJ diameter of CO_2 along the smaller axis of CO_2 (3.033 Å) . ZIF-93 contains a smaller concentration of CH_4 than ZIF-94, because the larger pores have very weak interaction with the CH_4 molecules because of the lack of partial charges of the guest molecule. The pores of ZIF-7 have little adsorption (Fig. 4.7), which can be explained by the small pore sizes that contribute to

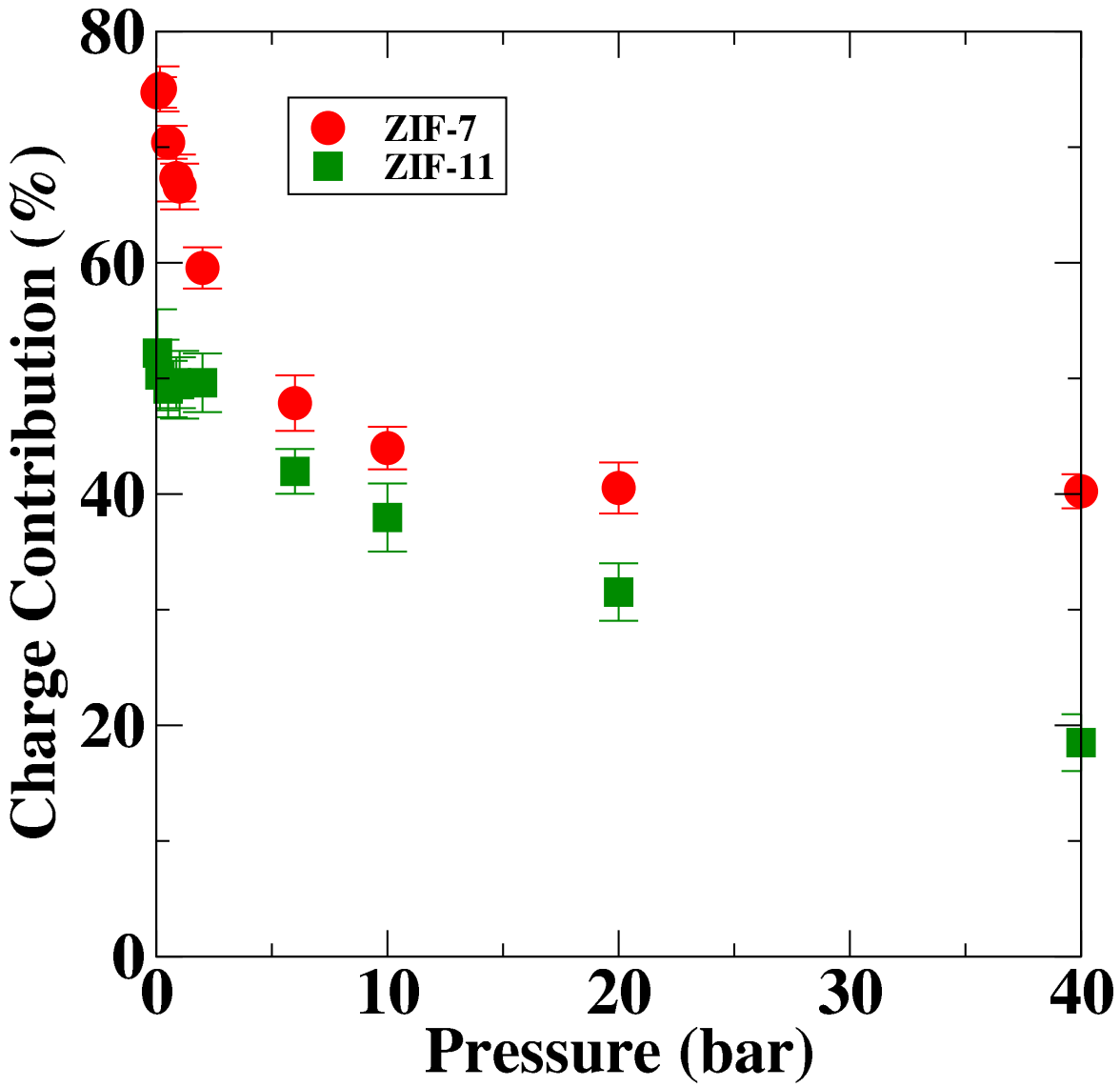

Figure 4.21: Charge Contribution for ZIF-7 and -11 for adsorption of CO_2.

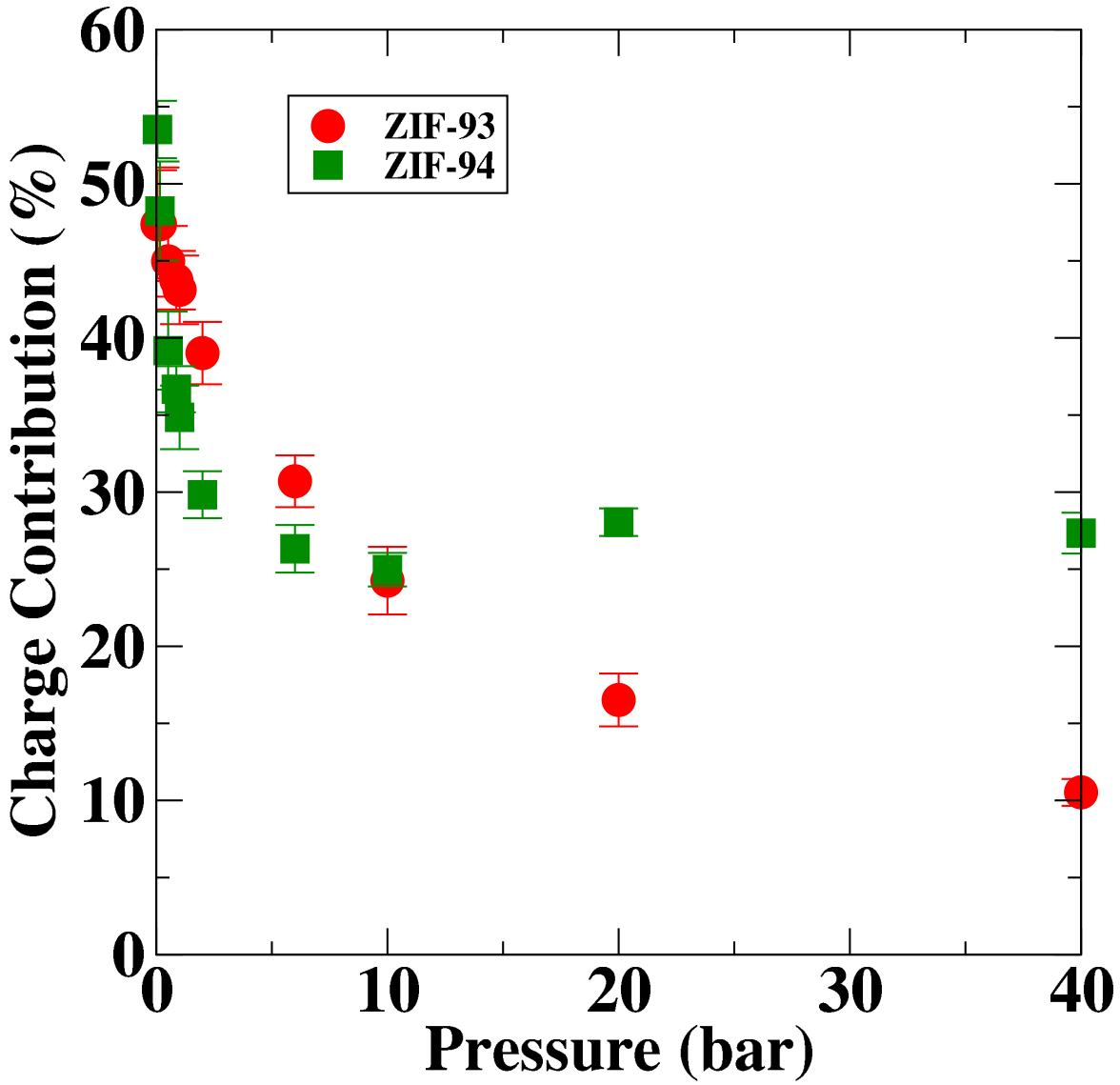

Figure 4.22: Charge Contribution for ZIF-93 and 94 for adsorption of CO_2.

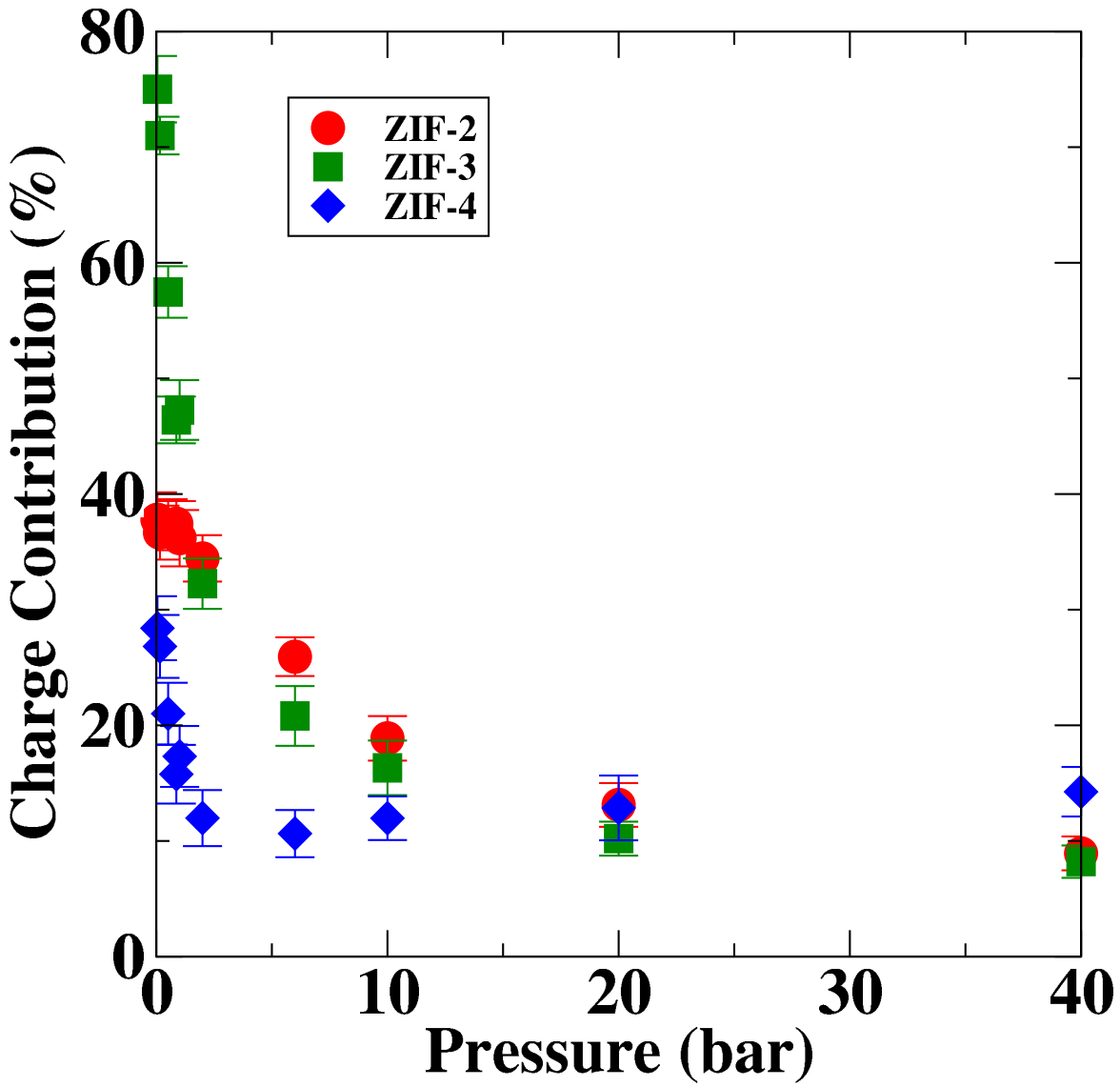

Figure 4.23: Charge Contribution for ZIFs 2-4 for adsorption of CO_2.

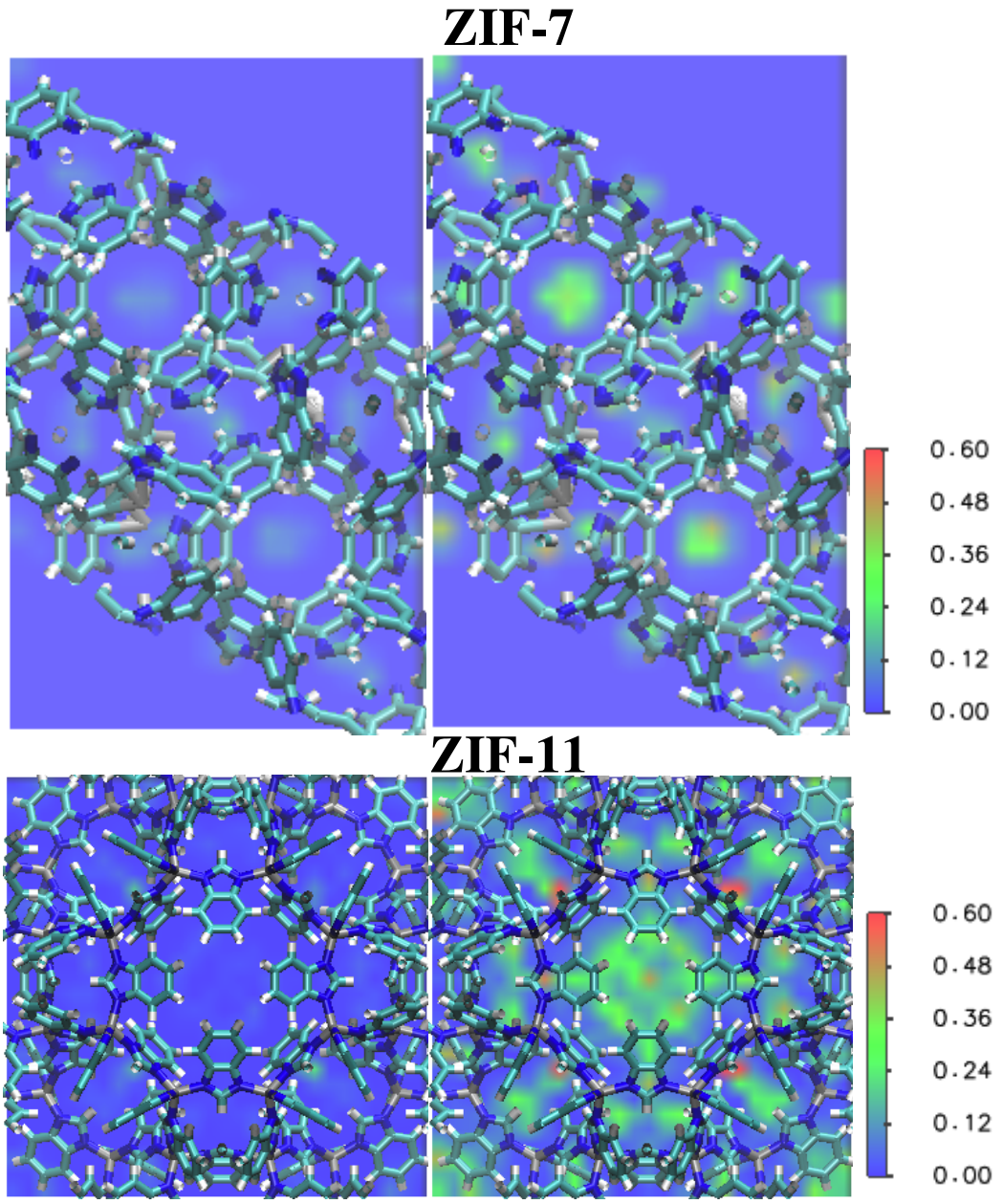

Figure 4.24: Density Maps for ZIF-7 and -11 for CO_2; Image dimensions for ZIF-7: 20 Å x 32 Å, Image dimensions for ZIF-11: 28 Å x 28 Å. Figures on left are at 101.0 kPa and figures on right are at 4000 kPa.

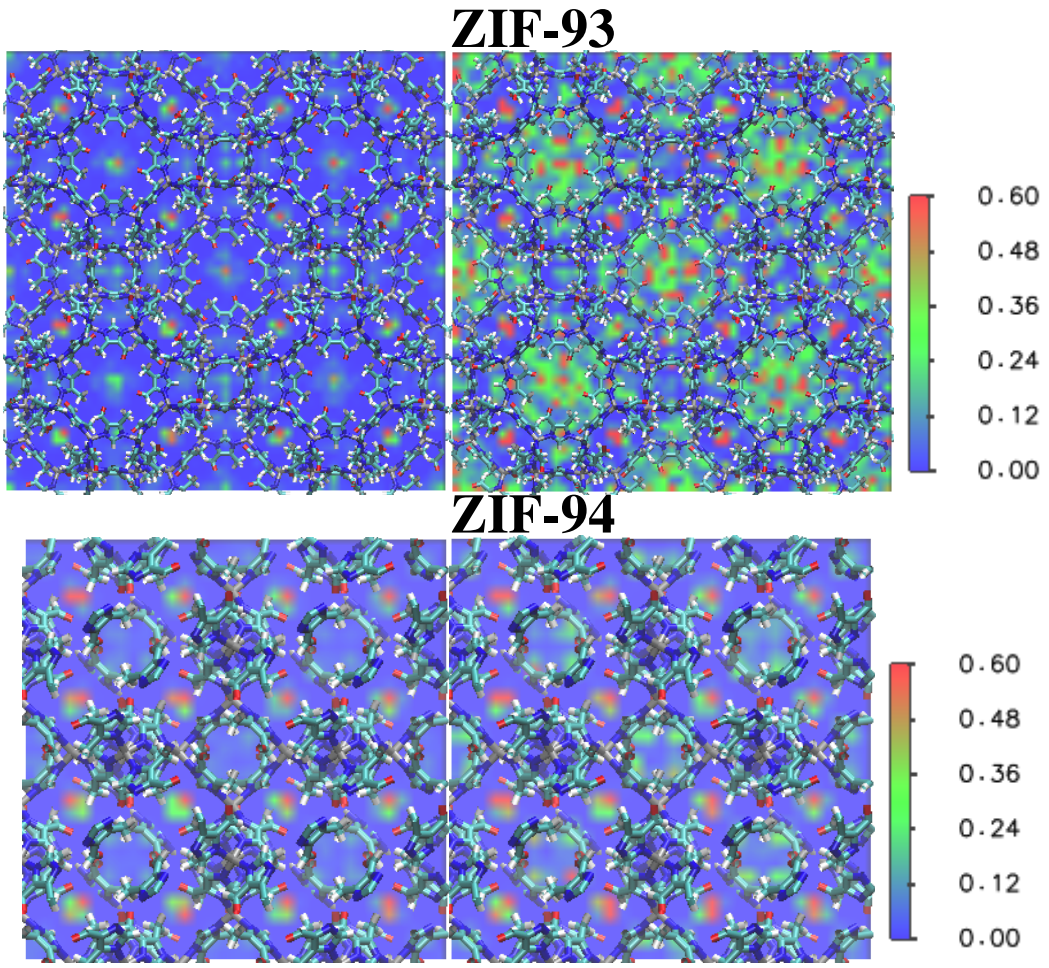

Figure 4.25: Density Maps for ZIF-93 and 94 for CO_2; Image dimensions for ZIF-93: 57 Å x 57 Å, Image dimensions for ZIF-94: 33 Å x 33 Å. Figures on left are at 101.0 kPa and figures on right are at 4000 kPa.

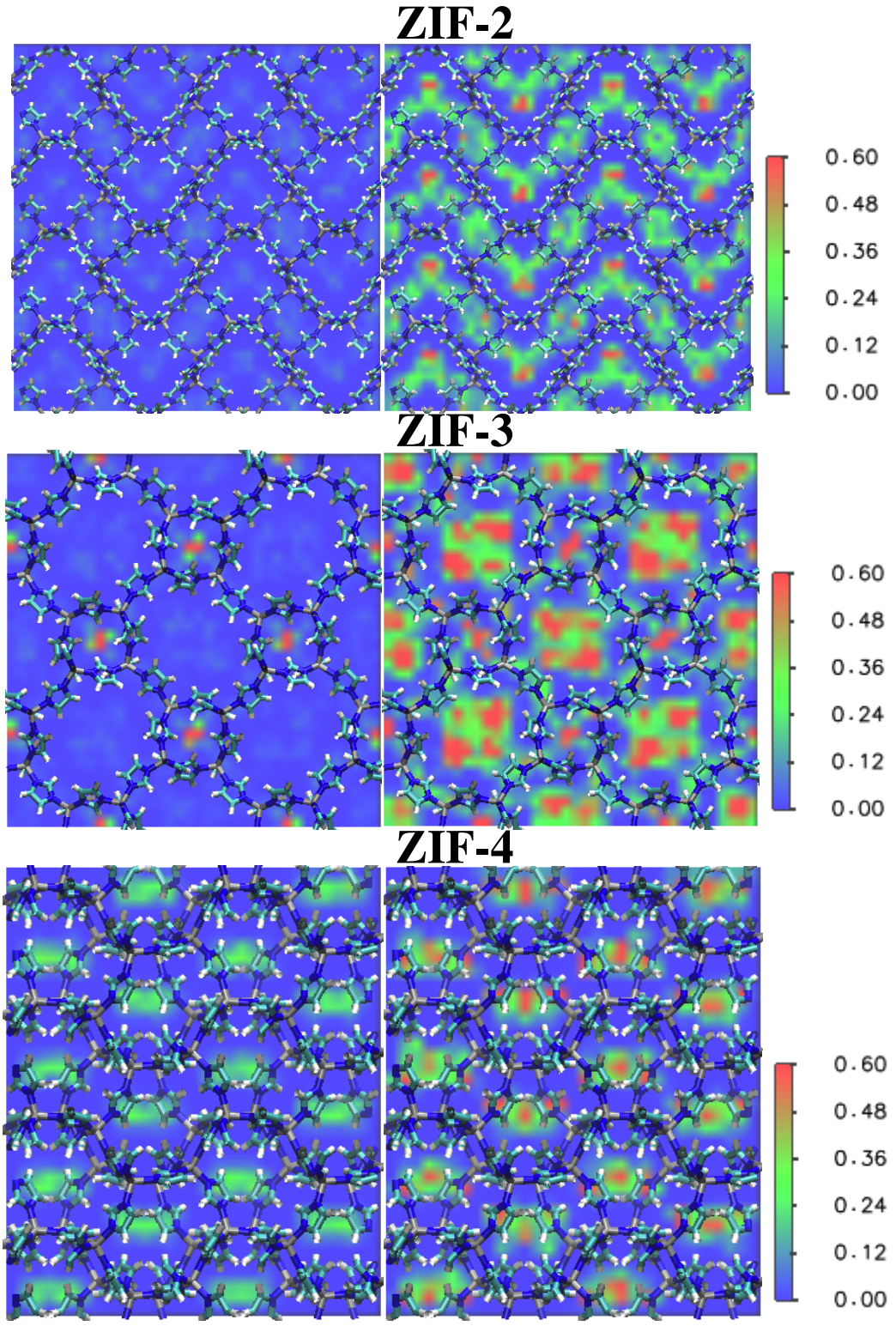

Figure 4.26: Density Maps for ZIFs 2-4 for CO_2: Image Dimensions for ZIF-2 : 49 Å x 49 Å, Image Dimensions for ZIF-3: 38 Å x 38 Å , Image Dimensions for ZIF-4: 31 Å x 37 Å. Figures on left are at 101.0 kPa and figures on right are at 4000 kPa.

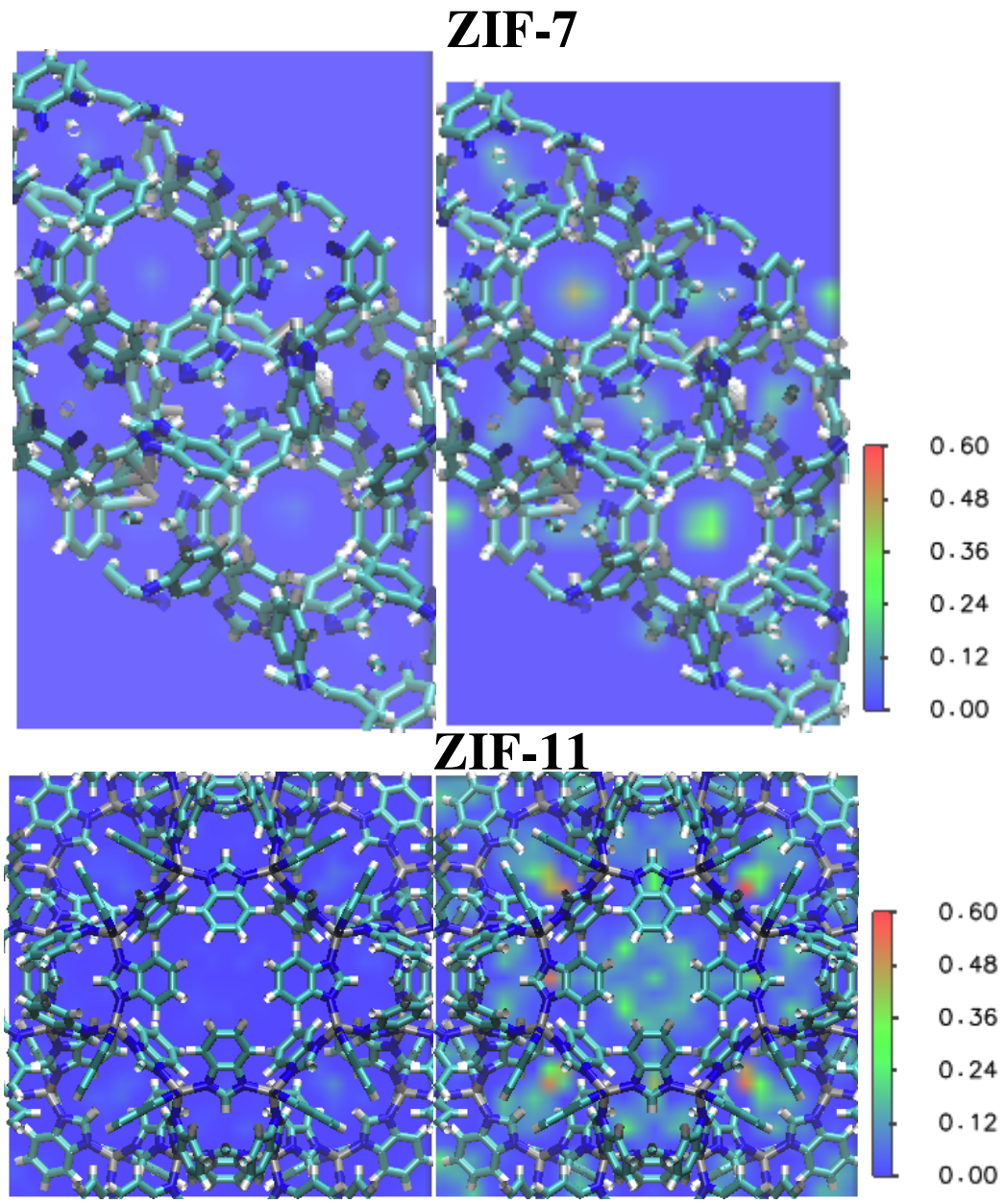

Figure 4.27: Density Maps for ZIF-7 and -11 for CH_4; Image dimensions for ZIF-7: 20 Å x 32 Å, Image dimensions for ZIF-11: 28 Å x 28 Å.

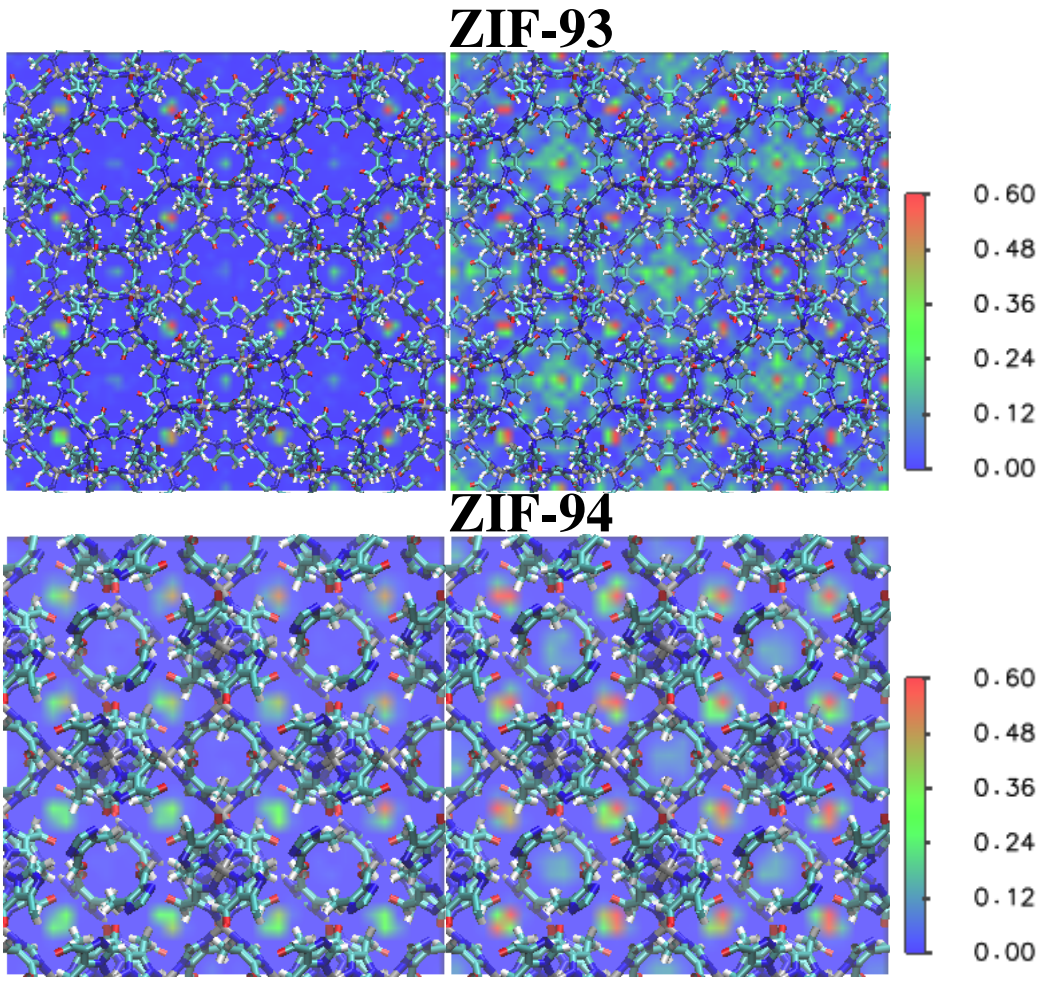

Figure 4.28: Density Maps for ZIF-93 and 94 for CH_4; Image dimensions for ZIF-93: 57 Å x 57 Å, Image dimensions for ZIF-94: 33 Å x 33 Å. Figures on left are at 101.0 kPa and figures on right are at 4000 kPa.

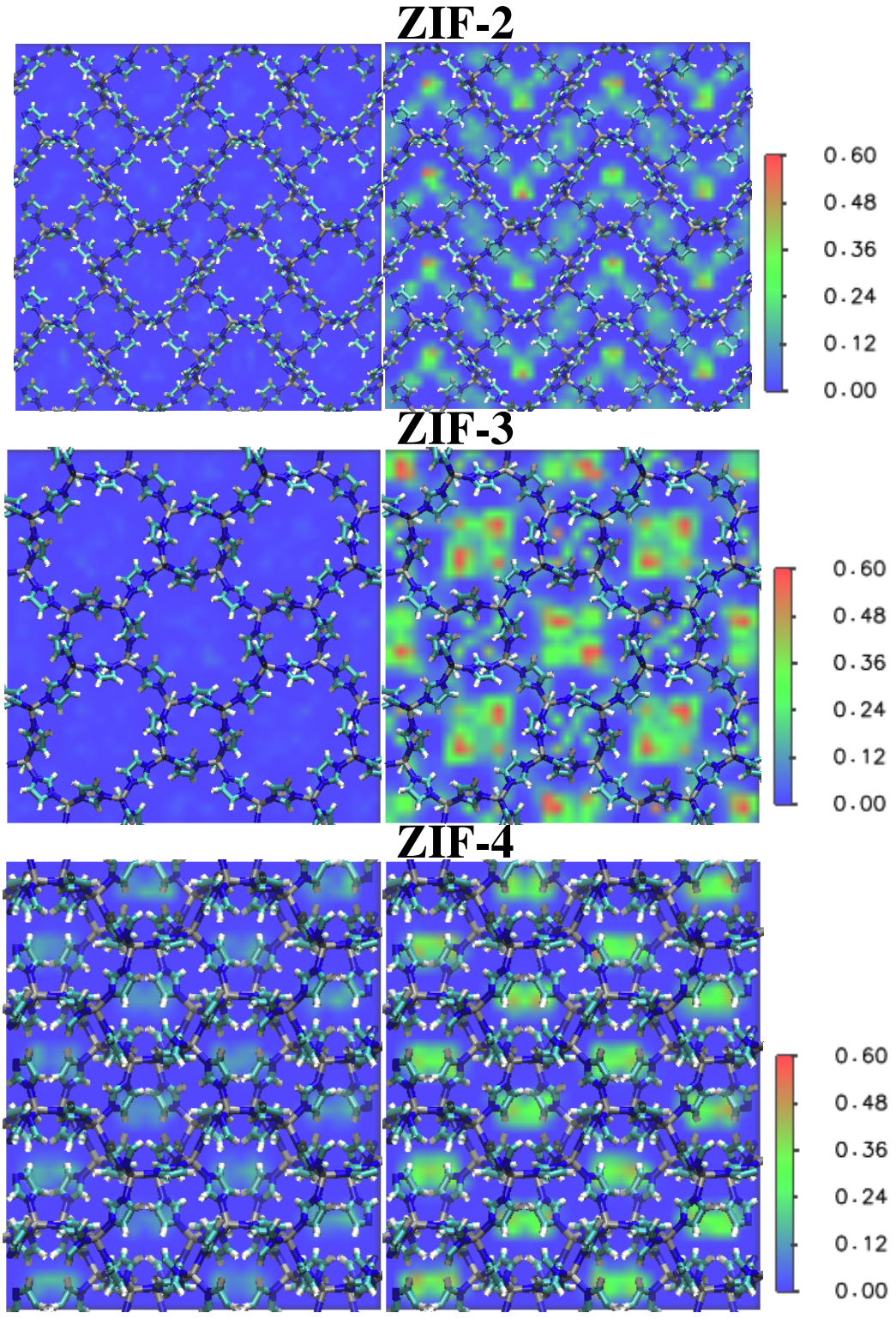

Figure 4.29: Density Maps for ZIFs 2-4 for CH_4: Image Dimensions for ZIF-2 : 49 Å x 49 Å, Image Dimensions for ZIF-3: 38 Å x 38 Å , Image Dimensions for ZIF-4: 31 Å x 37 Å. Figures on left are at 101.0 kPa and figures on right are at 4000 kPa.

steric hinderance of CH_4 adsorption.

For ZIF-7 and -11, we calculated the surface areas using the BET technique. We obtained surface area values of 406(26) and 609(11) m^2 $g^{-1}$for ZIF-7 and ZIF-11 respectively.

4.3 Toxic Gas Adsorption Simulations

ZIFs can also be used to adsorb toxic gases such as H_2S. We performed some analysis for adsorption of H_2S by the same set of RHO ZIFs examined for CO_2 adsorption in Ref. 7 and for CH_4 adsorption in Ref. 144. We choose this set so that we can examine the effect that functional groups have on adsorption. Adsorption is plotted at pressures up to 1.01 bar. To interpret the data, we will consider the calculated BET surface areas of these five ZIFs. Table 4.2 displays the surface areas of these ZIFs.[7] ZIF-25 possesses the largest adsorption, while ZIF-71, which has the lowest adsorption, has the second-lowest surface area. Surface area correlates with the amount of non-bonded interactions that can occur in a system, making surface area an important variable to account. However, electrostatic interactions do not necessarily correlate with surface area, thus we will also examine the effect of electrostatics on adsorption.

The effect of electrostatics on the adsorption of H_2S for the five RHO ZIFs is plotted in Figure 4.32. ZIF-71 has the lowest percent charge contribution, indicating that electrostatics plays little role in adsorption. This agrees with examination of percent contribution for CO_2 in Ref. 7, which was explained by noting the symmetrical arrangement of the functional groups on the imidazolate. We note that ZIF-25 also shows little contribution from electrostatics toward adsorption, which logically follows because this ZIF also has a symmetric arrangement of functional groups. We note that competitive effects appear to dictate adsorption between charge contribution and experimental surface area, with one exception. ZIF-71 has the second-lowest surface area and the lowest contribution from electrostatics, thus explaining its lowest adsorption. In contrast to the data for charge contribution for the previous set of ZIFs for CO_2 in this chapter, the effect of charge appears to grow larger with respect to pressure.

We also examine the adsorption of H_2S for ZIFs 2-4, and as in the previous section, we can determine the effect of topology on adsorption. As shown in Figure 4.33, adsorption in ZIF-3 is approximately the same at the lowest pressure as ZIF-2, despite the smaller pores that would seem to lead to a heightened interaction between framework and H_2S molecules, and thus higher adsorption. One possible explanation is that , as was the case for CH_4, the smaller pores of ZIF-3 do not readily adsorb H_2S because of size constraints. This leads to the only pores that are not sterically hindered from accepting these molecules have poor interactions with them. We base this finding on the pore diameter of the sulfur in the LJ model (3.72 Å) and the pore distribution for ZIF-3 in Fig. 4.6. In Figure 4.34, there is an anomalously low point at the lowest pressure for ZIF-2. One explanation we can give is that because the adsorption numbers are relatively small in this instance, differences between a framework with charges and without them may significantly vary depending on when the data is sampled.

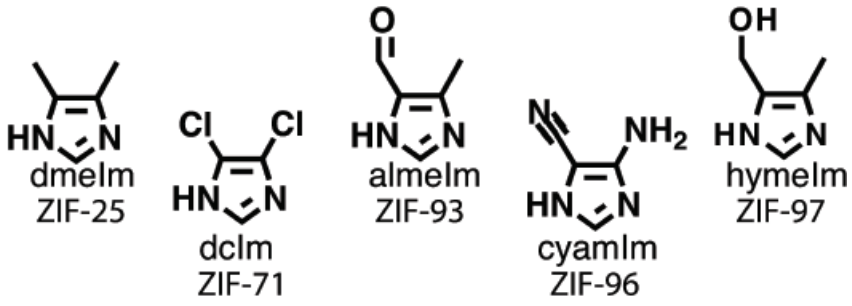

Figure 4.30: Functional groups for ZIF-25, -71, -93, -96 and -97. From Ref. 7.

ZIF	Surface area (m^2 g^{-1})
-25	1110
-71	652
-93	864
-96	960
-97	564

Table 4.2: Surface area of RHO ZIFs. From Ref. 7.

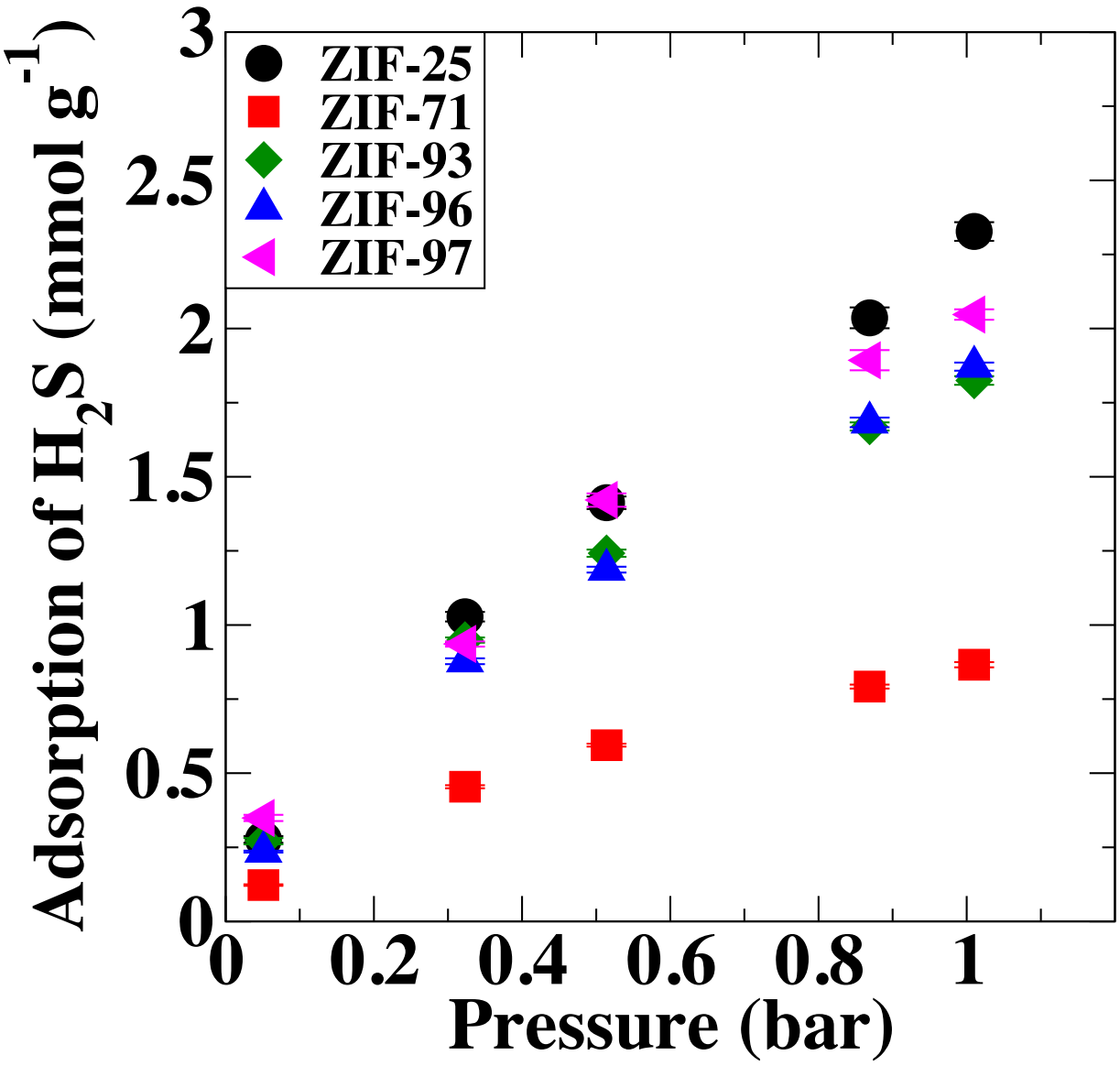

Figure 4.31: Adsorption of H_2S.

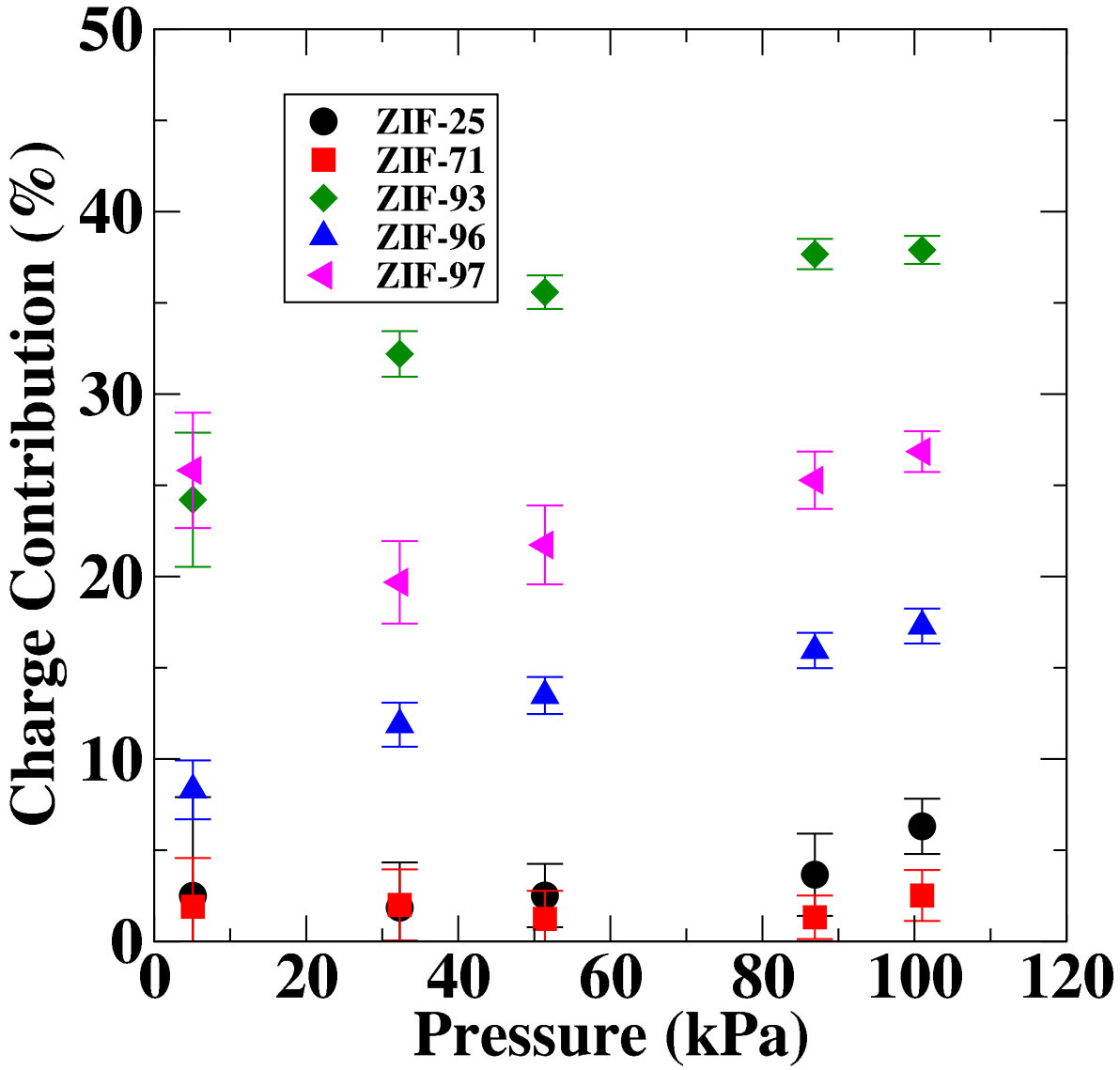

Figure 4.32: Percent of charge contribution toward adsorption of H_2S for ZIF-25, -71, -93, -96 and -97.

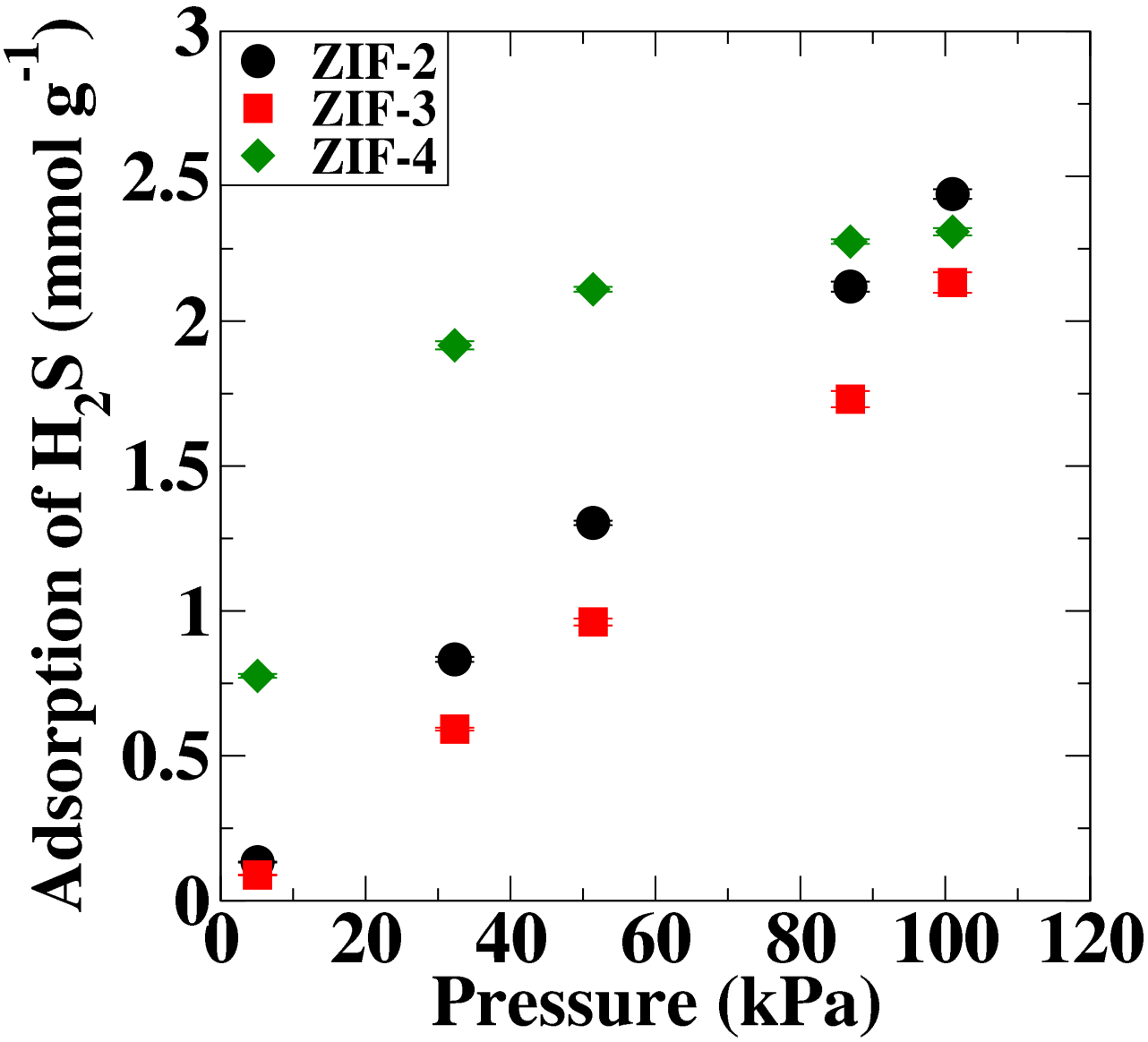

Figure 4.33: Adsorption of H_2S for ZIFs 2-4.

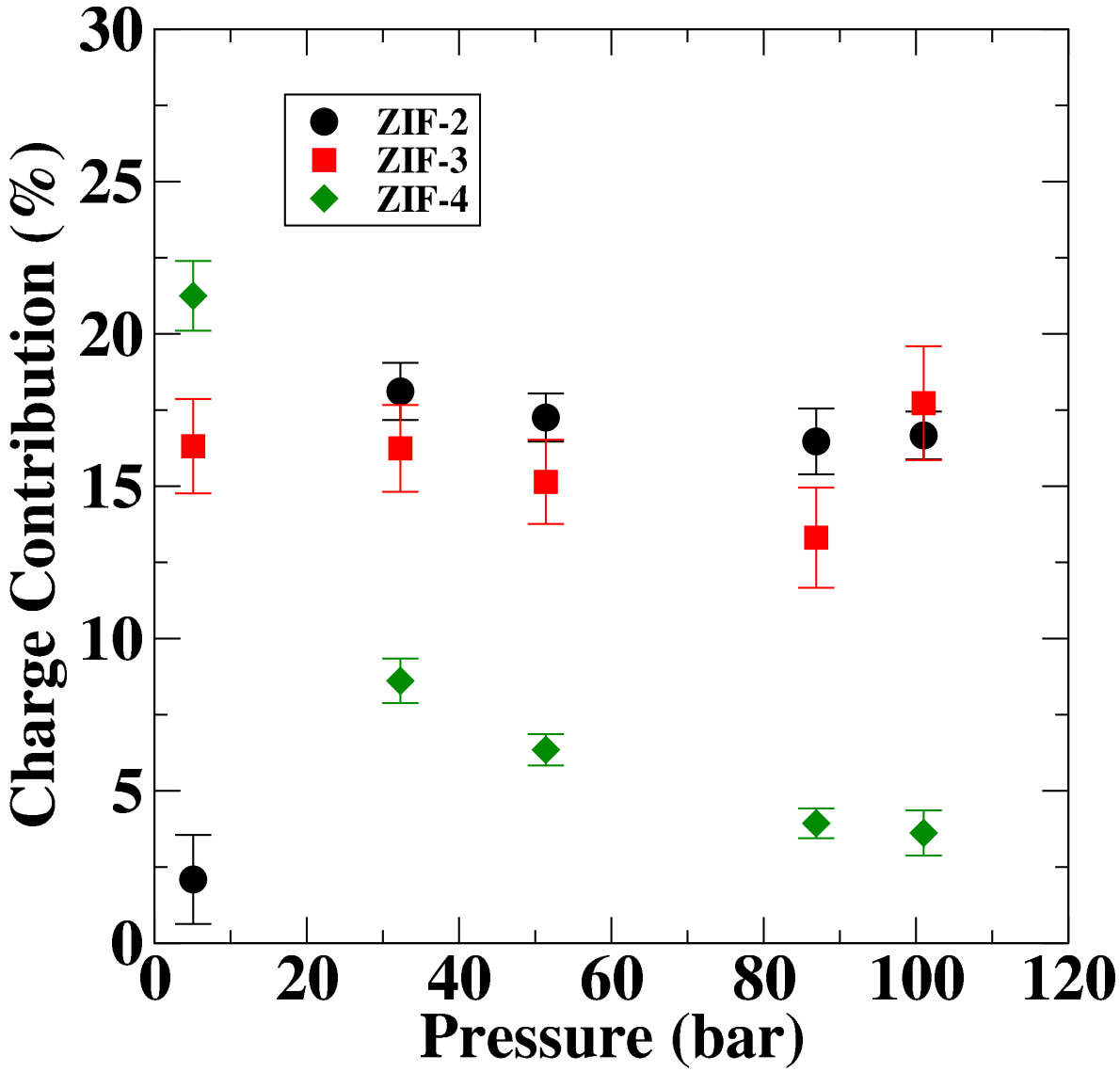

Figure 4.34: Percent of charge contribution toward adsorption of H_2S for ZIFs 2-4.

As of now, there is no experimental data on adsorption of H_2S for the ZIFs studied in this section.

4.4 Conclusion

Zeolitic Imidazolate Frameworks have the potential to serve as carbon capture and separation systems for industry. Simulations provide a means to examine the adsorption isotherms of ZIFs and to understand the atomic behavior that occurs during adsorption. As noted in Chapter 3, other researchers have used computer simulations to examine the adsorption properties of various ZIFs. Our work, however, is in a significantly smaller class of articles examining the effect to topology on adsorption of CO_2 and CH_4.

Our results agreed with experiment well, with the exception of ZIF-7. This anomaly can be explained by noting that ZIF-7 changes structure during experimental adsorption experiments, a situation not accounted for in our simulations, which assumed a rigid ZIF framework . Comparing the sets of ZIFs of 7/11 and 93/94, we observed that ZIFs with smaller pore volume had greater adsorption of CO_2 than those with larger pore volumes at lower pressures, while these trends were reversed at higher pressures. This can be explained by electrostatics for the former condition and sterics for the latter. We made maps plotting density of the guest molecules in the frameworks and observed that CO_2 molecules preferred to adsorb in smaller pores at lower pressure and at higher pressure went toward larger pores. For CH_4, we conclude, using the density maps created as basis, that the size and lack of partial charge for CH_4 make smaller and larger pores unfavorable for adsorption, respectively. We also examined the effect of removing charge from the ZIFs, and found that for the sets 7/11 and 93/94, the ZIF with larger pore volume had a larger contribution from charge at most to all pressures. For ZIFs 2-4, the small pores for ZIF-3 lead to significantly higher contribution toward adsorption at low pressures, which is belied by the overall pore volume. This discrepancy stems from the small pores that lead to a heightened guest molecule-host framework interaction.

Because ZIFs can also be used to capture gases harmful to human health, we have simulated the adsorption of H_2S for two sets of ZIFs: (25,71,93,96,97) and (2-4). For the former set of ZIFs, we observed that volume and effect of electrostatics contributed to the overall adsorption, with ZIF-25 having the largest volume and also greatest adsorption of H_2S. For trends in electrostatics, we note

that ZIF-25 and -71 show relatively little contribution from charge, which corresponds with the symmetric functional groups of these ZIFs. For ZIFs 2-4, we conclude that pore size becomes a bottleneck for ZIF-3 limiting adsorption.

Follow-up research can be done for both parts of our chapter. ZIF-7 showed the largest discrepancy with respect to experiment, which we attribute to the deformation the ZIF undergoes in experiment. Thus, in the future we can determine if we can simulate this ZIF using a flexible model to determine if we observe better agreement with experiment. We can also examine the effect of using a different model for CH_4, specifically a model in which the hydrogen atoms are explicit. This model would not only have the geometry of a CH_4 molecule, it could incorporate electrostatic interactions. For our work on H_2S, experimental work performed on this system would show if our simulations are reasonably accurate.

Part II

Energy Storage

Chapter 5

Overview on Background Literature on Energy Storage Systems

In Chapters 3 and 4, we explored the issues of gas capture and separation. In the next three chapters we will shift focus to the topic of energy storage. Renewable resources are critical in our society because of looming energy shortages, however many such sources, e.g. solar and wind, have the problem that they are intermittent. Thus, one may end up generating energy when not needed but unable to meet energy demand at other times. Because of this, energy storage devices serve a vital role. As will be shown, energy devices can be roughly categorized into two classes that differ in energy and power density: capacitors and batteries.

5.1 Energy Storage Systems

The first class of devices is that of electrostatic capacitors (to be referred hereafter as simply "capacitors"). *Capacitors* are composed of two metal plates separated by an insulator and energy is stored in these systems via electrostatic interactions. In principle, the system can be charged and discharged (a process known as a cycle) for an indefinite number of times. Such systems also can have relatively high power density compared to other storage devices. Unfortunately, capacitors have relatively low energy densities. The energy that a system can store is related to the

capacitance (C) of the system. In terms of the capacitance, the energy of a capacitor is given by Ref. 190

$$E = \frac{1}{2}CV^2 \tag{5.1}$$

where V is the applied voltage difference. The capacitance can be expressed using the following equation

$$C = \frac{A\varepsilon\varepsilon_0}{d} \tag{5.2}$$

where d is the distance between plates, A is the surface area of the plate, ε is the dielectric constant of the insulator, and ε_0 is the vacuum permittivity constant.

The other class is that of *batteries*. Unlike capacitors, batteries are often composed of electrodes separated by an electrolyte solution. Energy is released as chemical energy in the form of redox reactions that can occur at the electrodes. The cycle life (number of times the system can be charged and discharged) is often limited, stemming from the degradation of the system as the system is discharged and recharged many times. Because energy storage is related to the physical movement of ions, the power density of batteries is significantly smaller than that of capacitors. However, one advantage batteries have is that they have excellent energy densities.

The relative benefits and shortcomings of energy storage devices can be summarized visually in a so-called Ragone Plot (Figure 5.1). In this 2-d plot energy storage devices are classified by power and energy density, (though cycle life is also important for energy storage systems). Capacitors and batteries occupy opposite ends of the plot. One would like to use a device that had good energy density, but also good power density, so that the device does not release heat during the charge/discharge cycles. One application of note for this type of device is in hybrid automobiles.[191] Electrochemical capacitors (colloquially known as "supercapacitors"), are such a class of devices.

5.2 Supercapacitors

The category of supercapacitors may be further divided into two distinct subclasses. The first, *Electric Double-Layer Capacitors* (EDLCs), are similar to traditional capacitors in that energy is

stored through charge separation. However, instead of metal plates, the layers are the electrode and the nearest layer of ions, forming a "double layer." Because the distance between these layers is significantly smaller than that of capacitors, capacitance is greatly increased.[192] The nearest ionic layer in solvent can attract a layer of alternating charges to balance the first layer, but over-screening may occur which leads to alternating layers eventually vanishing in bulk solution.[193–195]

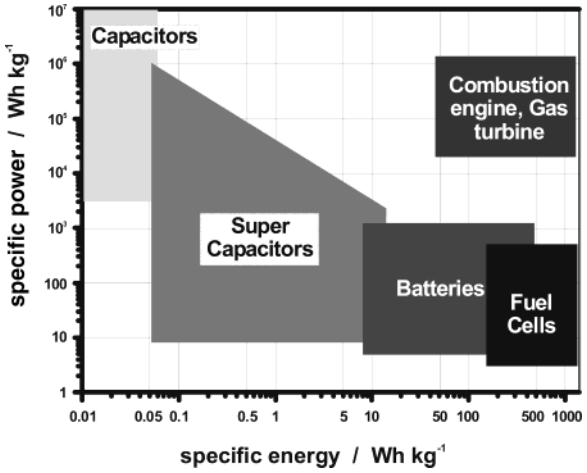

Figure 5.1: Ragone Plot. From Ref. 12. Energy storage systems plotted with respect to specific power and specific energy.

The second class of supercapacitors are *pseudocapacitors*, which have more similarities with batteries than with capacitors, despite their name. Redox reactions occur as with batteries, but mostly on the surface of the electrodes, which leads to greater power density than batteries, but poorer energy density.[192,196] As Conway[190] notes, pseudocapacitors also have double layers near the electrodes, but a pseudocapacitor is distinct in that its energy primarily comes from chemical reactions.

In what follows, we will give a few examples of research (both experimental and theoretical) that has been done in the field to give the reader an idea of the ways in which these systems can be studied, and then explore the properties of bulk solvents, specifically their dielectric constants.

Chimola, et al.[197] found that for a carbide-derived carbon supercapacitor, the capacitance showed anomalous behavior with respect to pore size. Previously, common thought was that the pore needed to be able to accommodate an ion with the ion's accompanying solvation shell. In

contrast to this, Chimola, et al. observed that capacitance displayed an anomolously large peak at pore sizes smaller than those needed to accommodate the solvation shell. Computer simulations have been found useful in exploring how capacitance is related to the atomistic details of the pore system of the supercapacitor. Feng and Cummings[198] observed, using MD simulations, that a capacitance peak occurred in addition to the peak at small pore sizes. To explain this phenomenon, the authors hypothesized that the ions near the walls of the slit pore create a 'wave' occurrence which creates its own EDL. The type of solvent has also been found to play an integral part, with cations and anions unequal in size and charge causing different levels of 'screening', affecting the relative potential.[199] In experiment, pore size distribution may give a misleading view on the effect of pore size on capacitance. Thus simulations, because they allow a singular pore size, can give a more accurate view of varying the pore.[200] Finally, there is evidence that certain types of supercapacitors (specifically based on nickel foam) can exceed 3000 F g^{-1},[201] though that claim has been disputed.[202]

5.2.1 Continuum Modeling of EDLCs

As shown in the previous section, supercapacitors have been amenable to study through experimental methods. However, using continuum models enables researchers to examine simplified versions of various systems to easily explore and optimize the variables that contribute to the properties of interest; for example, capacitance. Continuum modeling can model how capacitance varies with respect to dielectric constant of the electrolyte solvent. One example of a type of continuum modeling is based on the Gouy-Chapman equation[196,203,204]:

$$\nabla \cdot (-\varepsilon_0 \varepsilon \mathbf{E}) = -2FZc_b \sinh\left(\frac{eZ\psi}{k_B T}\right) \tag{5.3}$$

where F is the Faraday constant, Z is the valency of the ions in solution, c_b is the ionic concentration in the bulk of the solution, and ψ is the electric potential of the EDLC. Using Eq. 5.3, the potential of as system can be determined using inputs provided by the modeler. This equation can be modified by accounting for the interaction of the ions with the electrode wall.[196,204–206]

This is necessary because it accounts for the fact that the ions have finite sizes, which leads to ion exclusion. The modified equation can be expressed as

$$\nabla \cdot (-\varepsilon_0 \varepsilon \mathbf{E}) = -FZc_b \frac{2\sinh\left(\frac{eZ\psi}{k_B T}\right)}{1+2m\sinh^2\left(\frac{eZ\psi}{2k_B T}\right)} \tag{5.4}$$

where

$$m_i = 2d^3 N c_b \tag{5.5}$$

where d denotes the diameter of the solvated ion, N_{A} denotes Avagadro's constant and c_{b} is the molar concentration in the bulk.

To calculate capacitance for the 'diffuse' layer of an electrode, the following equation[13,196,203] is used

$$C = \frac{Q}{\psi_{1/2} S} \tag{5.6}$$

in which S is the surface area of the electrode, $\psi_{1/2}$ is the potential difference from the electrode to the center of the EDLC system and Q is the charge. To calculate the total charge, the following equation is used[203]

$$Q = \int \varepsilon_0 \varepsilon \mathbf{E} \cdot \mathbf{n} \mathrm{d}A \tag{5.7}$$

in which $\mathbf{n}$ is the 'normal vector' at the interface of anode and solution. In the above equation, it would be optimal to use a value of ε that is not constant, but varies with external stimulation, in this instance, applied electric field. The effect of field can be ascertained through solving an equation for this effect, or molecular simulations can be performed to examine the dielectric constant with respect to electric field.

The variable ε in Eq. 5.4 depends on the electric field, thus one can not assume that this is a constant value. Experiment has difficulty obtaining the dielectric constant with respect to electric field, especially at higher fields. Thus, a means to examine this relation will be critical for continuum modelers to more accurately perform their work.

Solvent	Chemical Formula	Structure
Ethylene Carbonate (EC)	$C_3O_3H_4$	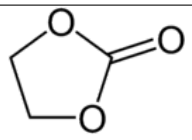
Propylene Carbonate (PC)	$C_4O_3H_6$	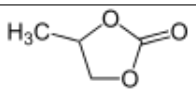
Acetonitrile (MeCN)	C_2H_3N	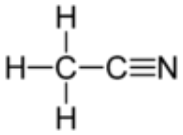
Dimethyl Carbonate (DMC)	$C_3O_3H_6$	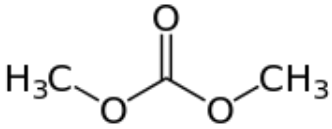

Table 5.1: Chemical information on organic solvents. Images from Wikipedia.

5.3 Electrolyte Solvents used for Supercapacitors

Before proceeding with investigations into solvent properties, we will first discuss the different types of solvent systems often considered in the literature. The three principal classes of electrolyte solutions are those based on *aqueous* and *organic* solvents and *ionic liquids*. The electric potential window in which bulk water is stable is 1.229 V,[12,192] which puts a limit on the use of aqueous solutions. Organic solvents have a larger window of stability with respect to voltage, although they typically have lower dielectric constants than water.[192,207,208] As was the case for organic solvents, ionic liquids have a wider stability window than water.[13,192,209,210] Ionic liquids also have the advantage of low flammability, which will make it a safer choice in mass use.[211,212] They also benefit from not requiring a solvent[210], unlike the previous two systems, though one can add a solvent (in Ref. 210, the authors noted that combining acetonitrile with ionic liquid provided good specific energy and serviceable 'maximum power') Ionic liquids have the disadvantage of high viscosity, which will impede the movement of ions in the solvent.[199,208,213]

5.3.1 Dielectric Constant

The property of the dielectric constant models the reaction of a system to an electric field. The dielectric constant is a key property needed to determine in order to calculate the capacitance of a capacitor. Understanding the dielectric constant is important because an EDLC can be approximated as a capacitor. One method to calculate the dielectric constant is by using the following equation

$$\varepsilon = n^2 + \frac{\langle M^2 \rangle - \langle M \rangle^2}{\varepsilon_0 k_B V T} \tag{5.8}$$

where M is the total dipole of the system at a given time and n is the index of refraction of the system studied. The property n^2 is the dielectric constant of the system under an electric field at infinite frequency, $E(\infty)$y. At infinite frequency, the contribution to the dielectric constant comes from the polarization of the charges. For the MD simulations in the next two simulations, we use non-polarizable charges, and thus set n=1.

5.3.2 Dielectric Constant of Solvents under Electric Field

Previous research has been done to find an equation to model the effect of an applied electric field on the dielectric constant of an electrolyte solvent.[203,214–220] In 1951, Booth derived two equations modeling the effect of electric field on the dielectric constant of water. Booth's first equation, based on work by Onsager,[221] has the form

$$\varepsilon = n^2 + \left(\varepsilon_0 - n^2\right)(3/\beta E)\left[\coth(\beta E) - \frac{1}{\beta E}\right] \tag{5.9}$$

where n is the index of refraction for the particular system, ε_0 is the dielectric constant at zero field, E is the electric field and β is a parameter dependent on the properties of the solvent. To determine β, Booth proposed the following relationship of β to the the dipole moment of the solvent molecule

$$\beta = \frac{5\mu_v}{2kT}\left(n^2 + 2\right). \tag{5.10}$$

However, the derivation of the relation relies on specific properties of water, which means that its applicability for other solvents is unclear and as we will see, incorrect. For the duration of this

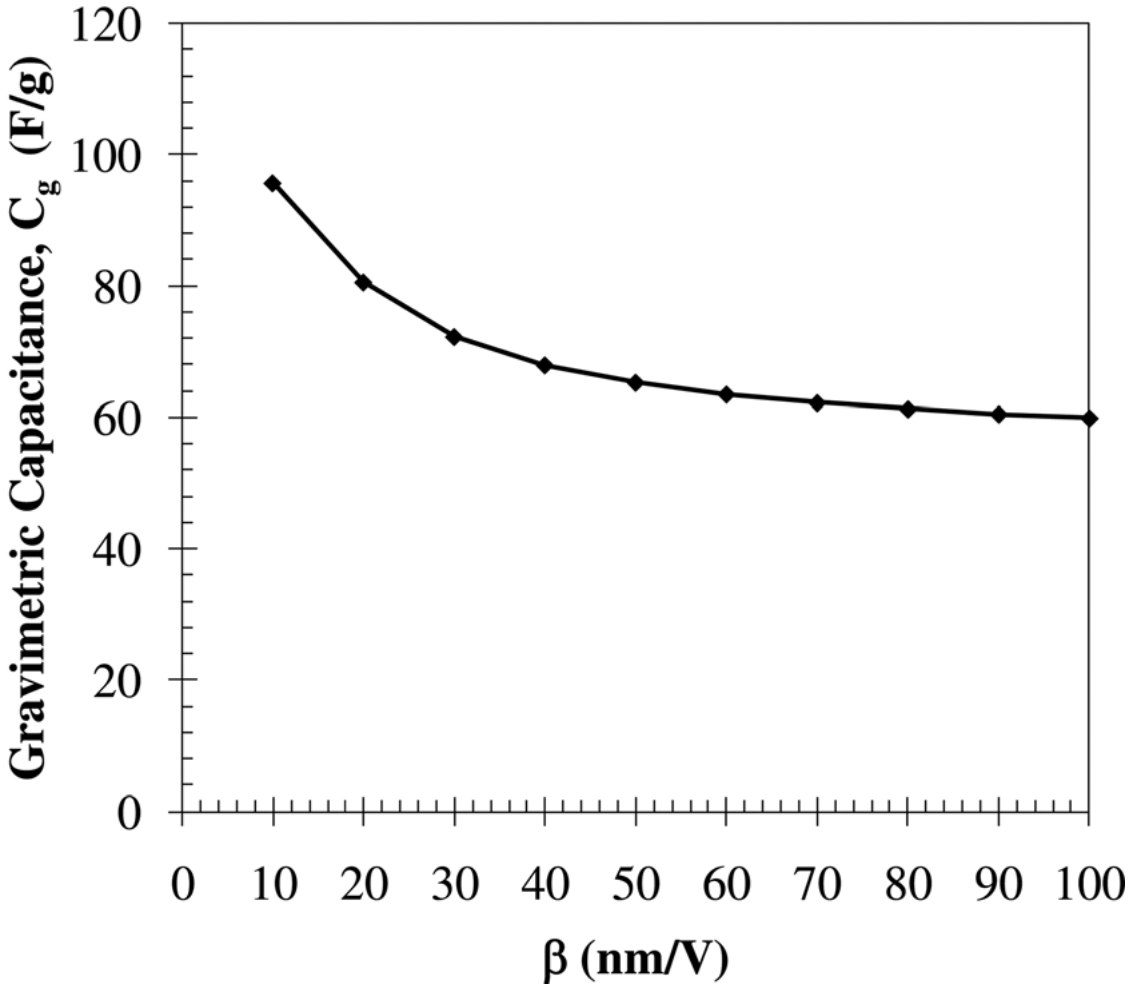

Figure 5.2: Effect of β on capacitance of solvent system composed of TEMA-BF_4 salt in propylene carbonate. From Ref. 13.

manuscript, we refer to Eq. 5.9 when we discuss the Booth Model. As noted earlier, work performed using atomistic simulations can be very beneficial for continuum modeling, and the above equation represents such a connection. Figure 5.2 shows that varying β of a propylene carbonate solution containing the salt TEMA-BF_4 will affect the capacitance of the EDLC calculated using the modified Gouy-Chapman equation (Eq. 5.4). To explain this, we note that a larger β will lead to the dielectric constant decreasing at a higher rate with respect to electric field. Because capacitance relies on dielectric constant, it then follows that the capacitance will decrease.

We noted above that Eq. 5.10 was derived specifically for water, thus we may have significant error applying this to organic solvents. Because of this, we fit our values for dielectric constant

with respect to electric field to obtain β, as was done in Ref. 203 for PC. In Ref. 203, they use Eq. 5.10 to calculate β for MeCN. In Chapter 6, we compare their value with ours. For the simulations in later chapters, note that we assign the value of 1 to n, which is equivalent to the system having no electron polarization. In the literature, there appear to be no atomistic simulations for the determination of the effect of applied electric field on dielectric constants and fitting to a Booth Model for DMC, EC and MeCN. Research has also been devoted to examining the effect of electric field on water. The authors of Ref. 222 used another equation in Booth's paper.[223] Good agreement was found with simulations also performed in Ref. 222, but a later paper[224] noted that the equation used was one that Booth later corrected. Significant error occurred when that correction was factored into the equation.

5.3.3 Dielectric Constant of Salt Solutions

The solvent in an EDLC often consists of a solvent and electrolyte (with room-temperature ionic liquids acting as both solvent and electrolyte). When performing continuum modeling, it is critical to understand the effect that the presence of ions can have on the dielectric constant. One widely observed phenomenon is that the dielectric constant tends to decrease with the addition of salt molecules. This phenomenon is called *dielectric decrement*. One explanation of the mechanism of dielectric decrement is that the ions of the dissolved salt form their own electric field, attracting the solvent molecules. This causes the dielectric constant to decrease, because the solvent molecules attracted to the ions are partially unable to contribute to collective dipole motion.[14,225–232] This is a rough approximation and other phenomena can occur. In 1977, a phenomenon known as 'kinetic polarization deficiency' was proposed in Ref. 233. Hubbard and Onsager state that this is caused by two factors: 1) The solvent is disrupted in its motion by the movement of the ion and thus has a delayed 'equilibrium polarization' and 2) The ions have competing forces of an applied electric field and the movement of the solvent molecules.

MD was used to simulate the dielectric constant of 'aqueous NaCl solutions' using a non-polarizable model and moderately good agreement was found with respect to experiment.[234] The

main problem noted was that the simulations were insufficiently long to achieve equilibrated $\langle M^2 \rangle$, (the average of the square of the total dipole of the system) which will affect the value obtained using Eq. 5.8. Simulations have also been used to calculate the dielectric constant of aqueous solutions containing biological molecules.[235,236] In Ref. 236, the dielectric constants of the various constituents of the solution (ions, water, sugar, phosphate) are calculated. To account for the effect that the electrolyte will have on the volume, and thus the dielectric constant, the volume that each constituent occupies is calculated so that the dielectric constant is not underestimated.

In addition to simulations, equations have originated to model the behavior of the dielectric constant. One simple equation uses the approximation noted above, relating the dielectric decrement solely to the effect of the ability of the ions to attract the solvent. The equation[14] is

$$\varepsilon = \varepsilon_{\mathrm{w}} + 2\delta c \tag{5.11}$$

where ε_{w} is the dielectric constant of water, c is the concentration of the salt and δ is a constant dependent on the salt. Figure 5.3, in Ref. 14, plots both experimental dielectric constant of aqueous NaCl solution, and a fitting of the data to Eq. 5.11.

Research on energy storage has been extensive and multiple threads can be followed for multiple topics, among them the electrical properties of the solvent system. MD has been applied to examine the effect of salt concentration on the dielectric constant, but there is a considerable gap in this field, specifically that pertaining to organic solvents. One difficulty in calculating dielectric constant is the time investment needed to ensure one has simulated an equilibrated system.

Understanding how the dielectric constant is affected by salt concentration and electric field is important to fully understand EDLCs. For both of these stimuli, MD can be used to study the trends in dielectric constants. In Chapter 6, we examine the effect of electric field on the dielectric constant of several organic solvent systems. In Chapter 7, we examine the effects that several salt systems have on the dielectric constants of several solvents, specifically focusing on acetonitrile.

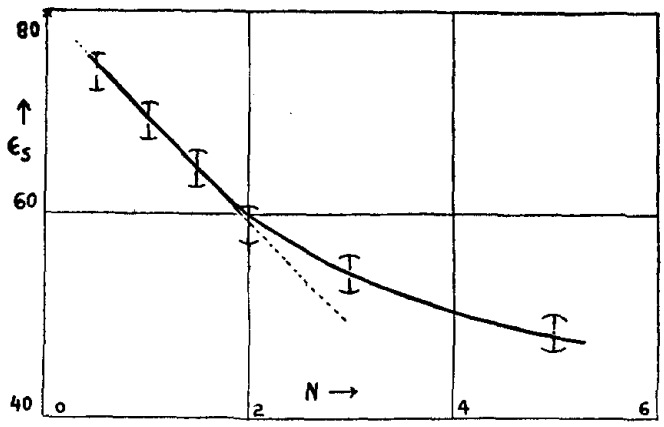

Figure 5.3: Dielectric constant with respect to normality, *N*. From Ref. 14.

Chapter 6

Effect of Electric Field on the Dielectric Constant of Organic Electrolyte Solvents

6.1 Introduction

In this chapter, we examine, using molecular-dynamics (MD) simulations, the effect of applied electric field on both pure and mixed organic electrolyte solvents, specifically acetonitrile (MeCN), propylene carbonate (PC), ethylene carbonate (EC), dimethyl carbonate (DMC) and EC/DMC mixtures. First, the force fields used are validated at zero field through the comparison of calculated density and dielectric constant with experiment. We then examine the effect of applied electric field on dielectric constant and fit the data to the Booth Model. For the systems examined, the Booth model gave a reasonable fit to our simulation data for low and moderate electric fields and we were able to calculate the values of β (Eq. 5.9) that will be useful in continuum model calculations. For MeCN and systems composed of predominately EC we observed anomalously low dielectric constants at high electric fields; due to the freezing of the solvent. at high electric field. This freezing was observed through the analysis of system snapshots. As long as the systems exhibiting freezing (electrofreezing) were excluded from the fits the Booth model was shown to give good representation of the data.

6.2 Simulation Procedure

All of the simulations reported in this and the following chapter are performed using the code LAMMPS.[237] A Nosé-Hoover thermostat is employed for all production runs to calculate dielectric constant in order to sample from a canonical (NVT) distribution. Equilibrium densities are calculated by adding an Andersen barostat to sample from an isothermal-isobaric distribution (NPT). We use the code Packmol[238] to create starting configurations for our systems. To implement this code, geometrical constraints (such as bond lengths) and minimum distances between atoms are input. The molecules created are continuously rotated and displaced until minimization is reached with respect to the input geometry. We used Towhee to convert the coordinates into a data file for LAMMPS. Simulations consisting of EC, PC and DMC used an initial minimization.The coordinates for the data file were rounded by Towhee to the nearest 0.00001 Å. A temperature of 298.0 K is used for all simulations with the exception of those for pure EC and EC/DMC mixtures. Note that the class of mixed solvents includes one simulation for EC and one for pure DMC. Thus, there will be one simulation at 298 K and another at 313 K for DMC. For all simulations, a damping parameter of 100 fs is used for the Nosé-Hoover thermostat. Unless otherwise stated, the target pressure of the Anderson barostat it set at 1.0 atm. A damping parameter of 100 fs is used for the Anderson barostat for all simulations, except for simulations of acetonitrile, for which a damping parameter of 500 fs is used. The larger damping parameter for MeCN was used because the simulations were unstable at the lower values. We used Lennard-Jones parameters to describe the van der Waals forces in our simulations, and point charges for the electrostatics. Simulations are performed with electric fields ranging from 0 to 4.0 V/Å in order to fit the Booth Models using equilibrated systems obtained from prior *NPT* simulations (for the 'mixed' systems) and *NVT* simulations (for 'pure' systems). Without loss of geometry, the electric field is along the z direction. Long-range electrostatic interactions were calculated using particle-particle-particle mesh solver.[31] We used a switching function for the Lennard-Jones and Coulombic interactions, with an inner cutoff of 10.0 Å and and an outer cutoff of 10.1 Å. We used a timstep of 1.0 fs.

The AMBER force field[239] is used to model the LJ interactions for EC and PC. Charges for

PC are from Ref. 219 and charges for EC are from Ref. 240. We use a large force constant for PC and EC to keep the bonds and angles relatively rigid, with some exceptions. For these noted exceptions, we used parameters from Amber (force constants, bond lengths and angles) for bonds C5-H4, C5-H5, C5-H6 and C4-C5 and angles C4-C6-H4, C4-C6-H5 and C4-C6-H6 in PC (refer to Table 6.5). For DMC, we use another large force constant make the bonds and angles relatively rigid (refer to Table 6.3). For DMC, we use the LJ and charges from Wheeler.[241] We also use Wheeler's terms for the dihedral parameters for DMC, but different conditions are used to obtain them compared to the ones we employ in our simulations, namely, we do not use modified 1-5 Lennard Jones parameters and Wheeler did not use Lorentz-Berthelot mixing. Despite these differences, we observe reasonable agreement with the density Wheeler observed. We observed a dielectric constant of 2.94(4) and density at 0.1 MPa of 1.0556(16) g/mL, compared to Wheeler's values of 1.63(2) and 1.065 g/mL, respectively. The values in parentheses denote the statistical errors (95 % confidence level) in the last digit shown. Note that Wheeler used the experimental n^2 for DMC, but we substituted this with n^2=1 in order to compare our values. Though Wheeler's and our dielectric constant values are significantly different, we also note that our value is closer to that of experiment. We use Ref. 242 for our force field. For MeCN, we use a force constant of 8888 kcal/mol to maintain relative rigidity for the angle and SHAKE[243] to maintain rigidity for the bonds. We model hydrogens implicitly for DMC and MeCN, and explicitly for EC and PC. We use model our bonds and angle for all systems harmonically. For DMC, we use the following equation to model the dihedrals

$$E = \sum_{n=1}^{6} A_n \cos^{n-1}(\phi) \tag{6.1}$$

where A_n are the force constants and ϕ is the dihedral angle. We modified the LAMMPS source code to use Eq. 6.1.

Atom	Color
Oxygen	Red
Carbon	Black
Nitrogen	Blue
Hydrogen	White

Table 6.1: Legend for colors used for atoms in chapter.

Atom Type	σ (Å)	ε (kcal/mol)	q (e$-$)
N	2.95	0.119503	-0.398
C1	3.55	0.119503	0.129
C2 (Methyl)	3.75	0.195268	0.269

Bond Type	r (Å)	k_r (kcal/Å^2)
C2-C1	1.54	(SHAKE used)
C1-N	1.16	(SHAKE used)

Angle Type	θ (°)	k_r (kcal/rad^2)
C2-C1-N	180.	8888.

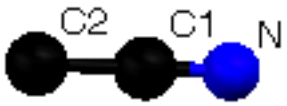

Table 6.2: LJ and charge parameters for MeCN.

Atom Type	σ (Å)	ε (kcal/mol)	q (e−)
O1	2.97	0.1882	-0.48
C1	3.65	0.1101	0.84
O2	3.00	0.1700	-0.47
C2 (Methyl)	3.80	0.1699	0.29

Bond Type	r (Å)	k_r (kcal/Å^2)
O1-C1	1.202	1111.
C1-O2	1.334	1111.
O2-C2	1.433	1111.

Bond Type	θ (°)	k_r (kcal/rad^2)
O1-C1-O2	122.38	1111.
O2-C1-O2	115.02	1111.
C1-O2-C2	115.24	1111.

Dihedral Type	A_1 (kcal)	A_2 (kcal)	A_3 (kcal)	A_4 (kcal)	A_5 (kcal)	A_6 (kcal)
All	9.9637	1.3219	-12.1284	-1.0130	3.4933	0.9680

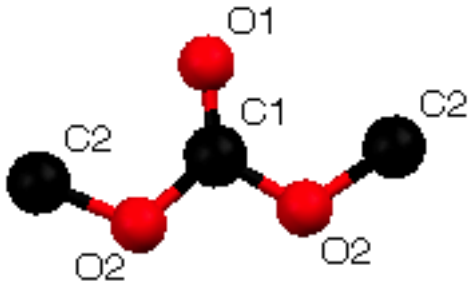

Table 6.3: Parameters for DMC.

Atom Type	σ (Å)	ε (kcal/mol)	q (e−)
O1	2.96	0.210	-0.5481
C1	3.4	0.0860	0.8499
O2	3.00	0.170	-0.4081
C2	3.4	0.1094	0.0954
H	2.47	0.0157	0.0809

Bond Type	r (Å)	k_r (kcal/Å^2)
O1-C1	1.202	1021.584
C1-O2	1.363	1021.584
O1-C2	1.442	1021.584
C2-C2	1.542	1021.584
C2-H	1.094	1021.584

Angle Type	θ (°)	k_r (kcal/rad^2)
O1-C1-O2	124.5	1021.584
C1-O2-C2	110.56	1021.584
O2-C1-O2	110.62	1021.584
O2-C2-C2	106.3	1021.584
O2-C2-H	108.72	1021.584
C2-C2-H	111.57	1021.584
H-C2-H	109.21	1021.584

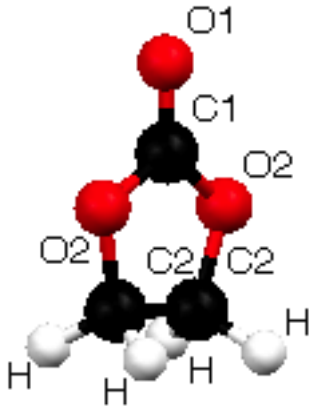

Table 6.4: Parameters for EC.

Atom Type	σ (Å)	ε (kcal/mol)	q (e−)
O1	2.96	0.210	-0.5522
C1	3.4	0.0860	0.8481
O2	3.00	0.170	-0.4066
O3	3.00	0.170	-0.406
C4	3.4	0.1094	0.1119
C5	3.4	0.1094	0.096
H1	2.47	0.0157	0.086
H2	2.47	0.0157	0.080
H3	2.47	0.0157	0.079
C6	3.4	0.1094	-0.1111
H4	2.65	0.0157	0.0659
H5	2.65	0.0157	0.0522
H6	2.65	0.0157	0.0568

Bond Type	r (Å)	k_r (kcal/Å^2)
O2-C4,O3-C5	1.442	1021.584
C1-O2,C1-O3	1.363	1021.584
C4-C5	1.542	1021.584
C4-H1,C5-H2,C5-H3	1.094	1021.584
C4-C6	1.335	490.
C1-O1	1.202	1021.584
C6-H4,C6-H5,C6-H6	1.09	340 .

Bond Type	θ (°)	k_r (kcal/rad^2)
O2-C4-C5,O3-C5-C4	106.3	1021.584
O2-C4-H1	108.72	1021.584
O2-C4-C6	117.82	1021.584
O2-C1-O3	110.62	1021.584
O2-C1-O1,O3-C1-O1	124.5	1021.584
C4-O2-C1, C5-O3-C1	110.56	1021.584
C4-C5-H2, C4-C5-H3, C5-C4-H1	111.57	1021.584
C4-C6-H4, C4-C6-H5, C4-C6-H6	109.5	35.
C5-C4-C6	111.63	1021.584
H1-C4-C6	105.22	1021.584
H2-C5-H3	109.21	1021.584
H4-C6-H5, H4-C6-H6, H5-C6-H6	109.61	1021.584

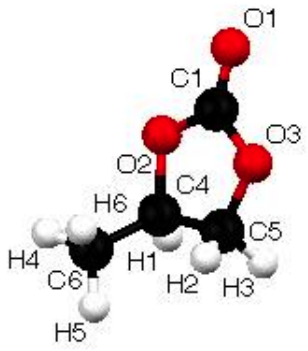

Table 6.5: Parameters for PC.

6.3 Validation of Force Fields

	Experimental Density (g/mL)	Calculated (g/mL)
EC (40 °C)	1.32199[15]	1.3244(9)
PC (25 °C)	1.19758[244]	1.2639(14)
MeCN (25 °C)	0.7762[245]	0.7801(7)
DMC (25 °C)	1.06350[246]	1.0534(9)

Table 6.6: Experimental and Simulation Densities

	Experimental ε	Calculated ε
EC	90.03[15] (40 °C)	106(7) (40 °C)
PC	64.92[247] (25 °C)	55(2) (25 °C)
MeCN	35.95[248](25 °C)	31.9(4) (25 °C)
DMC	3.20[15] (25 °C)	2.94(4) (25 °C)

Table 6.7: Experimental and simulation Dielectric Constants for Pure Solvents.

To validate the force fields used, we calculate density and dielectric constants for pure solvents and compare them with experimental results. As shown in Tables 6.6 and 6.7, we find excellent agreement for the densities of bulk solvents. The agreement for the dielectric constant is less quantitative, but given the relatively simple force field used, we believe the force fields our suitable to model these solvents.

We also verify that our force fields reliably model EC/DMC mixtures. As shown in Figures 6.1 and 6.2, the densities of EC/DMC are in excellent agreement with experiment and dielectric constants are represented well, respectively.

x_{EC}^{exp}	ρ_{EC}^{exp}(g/mL)	x_{EC}^{exp}	ρ_{EC}^{exp}(g/mL)
0	1.041800	0	1.0350(14)
0.1021	1.065537	0.1017	1.0647(11)
0.1500	1.078070	0.15	1.0779(10)
0.2036	1.092185	0.2033	1.0931(14)
0.2500	1.104502	0.25	1.1078(9)
0.3048	1.118926	0.305	1.1217(8)
0.4054	1.145494	0.405	1.1464(11)
0.4543	1.158835	0.455	1.1623(15)
0.5057	1.172863	0.505	1.1756(9)
0.6054	1.200435	0.605	1.2059(11)
0.7045	1.228921	0.705	1.2384(7)
0.8036	1.257472	0.8033	1.2646(10)
0.9025	1.287888	0.9033	1.2911(13)
1	1.321991	1	1.3241(9)

Table 6.8: Density of EC/DMC mixtures as a function of the mole fraction of EC. Experimental data from Ref. 15 is shown for comparison.

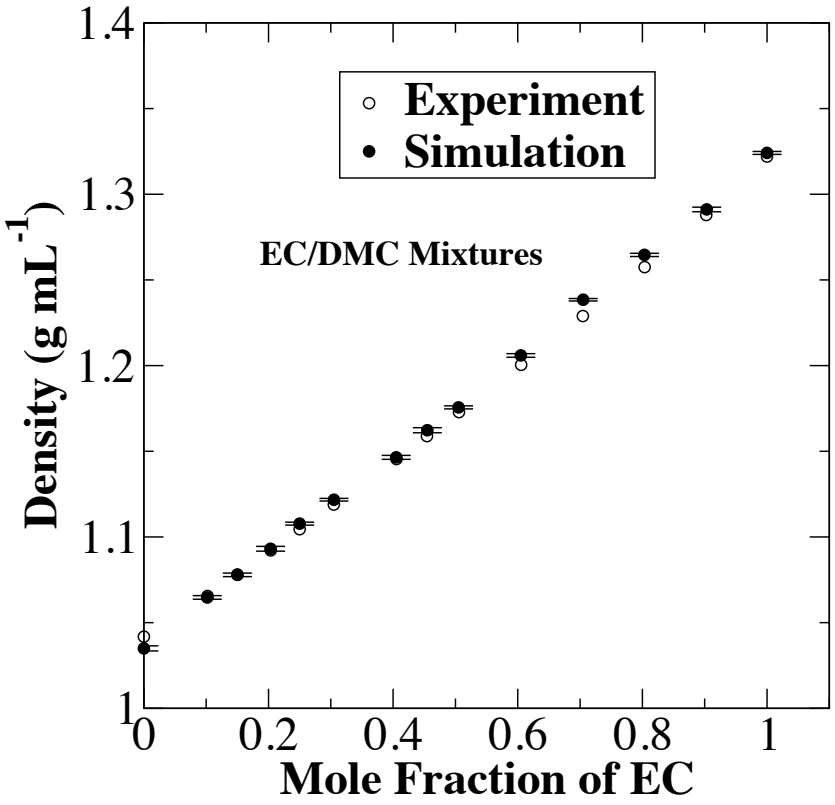

Figure 6.1: Density of EC/DMC mixtures as a function of the mole fraction of EC. Experimental data from Ref. 15 is shown for comparison.

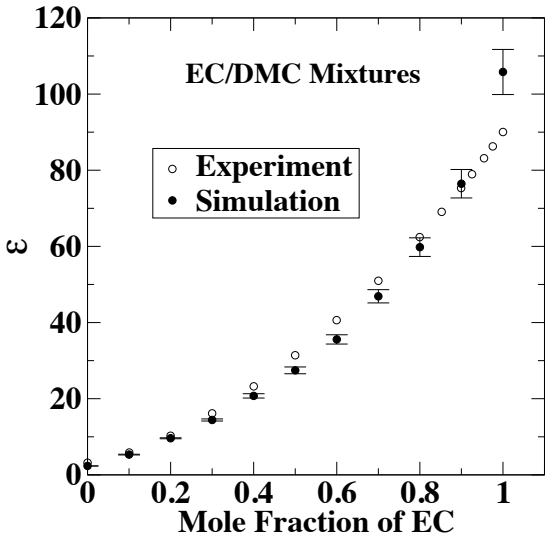

Figure 6.2: Dielectric constant of EC/DMC mixtures as a function of the mole fraction of EC. Experimental data from Ref. 15 is shown for comparison.

x_{EC}^{exp}	ε^{exp}	x_{EC}^{sim}	ε^{sim}
0	3.19	0	2.341(14)
0.1004	5.87	0.1	5.33(9)
0.1999	10.27	0.2	9.61(14)
0.3000	16.14	0.3	14.4(3)
0.4001	23.24	0.4	20.7(6)
0.4998	31.41	0.5	27.4(9)
0.5997	40.62	0.6	35.6(12)
0.7001	50.97	0.7	46.9(17)
0.7996	62.43	0.8	60(2)
0.8525	69.06		
0.8993	75.31	0.9	76(4)
0.9255	78.95		
0.9545	83.14		
0.9755	86.27		
1	90.03	1.0	106(6)

Table 6.9: Dielectric constant of EC/DMC mixtures as a function of the mole fraction of EC. Experimental data from Ref. 15 is shown for comparison.

6.4 Results for the Dielectric Constant of Pure Solvents in Electric Field

Now that our force fields have been verified, we can now examine the effect of applied electric field on the dielectric constants of our systems. In this section, we examine pure solvents. The dielectric constants, for the most part, decrease with respect to electric field, which agrees with the expectation that the dipole fluctuations are damped by their alignment with the field. The effect of electric field on dipoles causes the mean square fluctuation of dipole moment to decrease, and thus the dielectric constant.

For several systems the dielectric constants are anomalously low at high electric field. We hypothesize that this occurs because the solvent systems are freezing under these high fields. We verified this hypothesis through the visual observation of snapshots. Thus, we did not include them in the fitting. The values of the dielectric constant are fit to Eq. 5.9, and at low and intermediate fields, the Booth model fits the data well, as shown in Figures 6.3 and 6.4. Table 6.10 shows the beta values for pure solvents. Because Pratt et al. calculated β for PC, we have a value with which to compare our result for β. We compare his value with ours (13.14[203] and 11.3(7) nm/V, respectively). The differences can be attributed to the use of different force fields for PC. Because Wang, et al.[203] used Eq. 5.10 to calculate β for MeCN, we can compare their value for β with ours and determine if the value of β is significantly dependent on the method used to calculate it. Wang, et al. obtained a value of 30.2 nm/V while in contrast, we used fitting to obtain a value of 6.29 nm/V. We draw the conclusion that it is critical to correctly choose the method in which one calculates β.

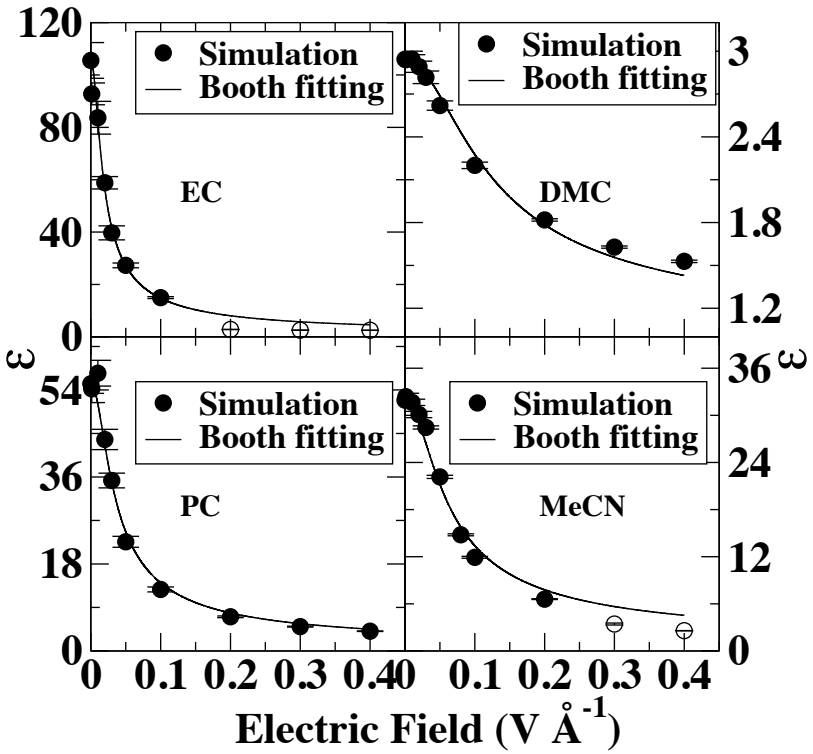

Figure 6.3: Booth models of PC, EC, DMC and MeCN. Simulations for DMC, MeCN and PC performed at 298 K, while for EC, 313 K. Open symbols are used to denote samples where crystallization ("electrofreezing") has occurred. These points were excluded from the fitting.

Solvent	β (nm/V) Fitted Value
EC	22(2)
PC	11.3(7)
DMC	3.12(18)
MeCN	6.29(18)

Table 6.10: Simulation values for β from the Booth model (5.9) for pure solvents.

DMC:EC Ratio	β(nm/V) Fitted Value
0:1	21(2)
1:9	16.0(8)
3:7	14.1(7)
1:1	10.6(5)
7:3	9.3(5)
9:1	6.1(2)
1:0	2.34(6)

Table 6.11: Simulation values for β from the Booth Model (5.9)for EC/DMC solvents.

6.5 Results for EC/DMC mixtures

In Figures 6.4, we examine the effect of electric field on the dielectric constant of varying molar ratios of EC/DMC mixture. Table 6.11 shows β for these mixtures We note that in Figure 6.4, the dielectric constant is anomalously low at high fields for systems predominately composed of EC. We attribute these values to the solvent system electrofreezing. To test this claim, we will examine the $g(r)$ plots for varying molar ratios of EC/DMC in order to understand the structuring of the system. Focus will be given to $g(r)_{\mathrm{O_c\text{-}O_c}}$, in which $\mathrm{O_c}$ is the carbonyl oxygen of EC. For systems solely containing EC in Figure 6.5, we note the appearance of a sizable peak starting at 0.15 V/Å, which coincides with the anomolously low dielectric constant for this system described earlier. Thus, we hypothesize that the large change we observe in the RDF correlates with our data for the dielectric constants. To lessen doubt concerning this correlation, we examine additional RDF plots of mixtures. These additional RDF plots also gain an additional peak between the same fields that we find that the dielectric constant suddenly changes.

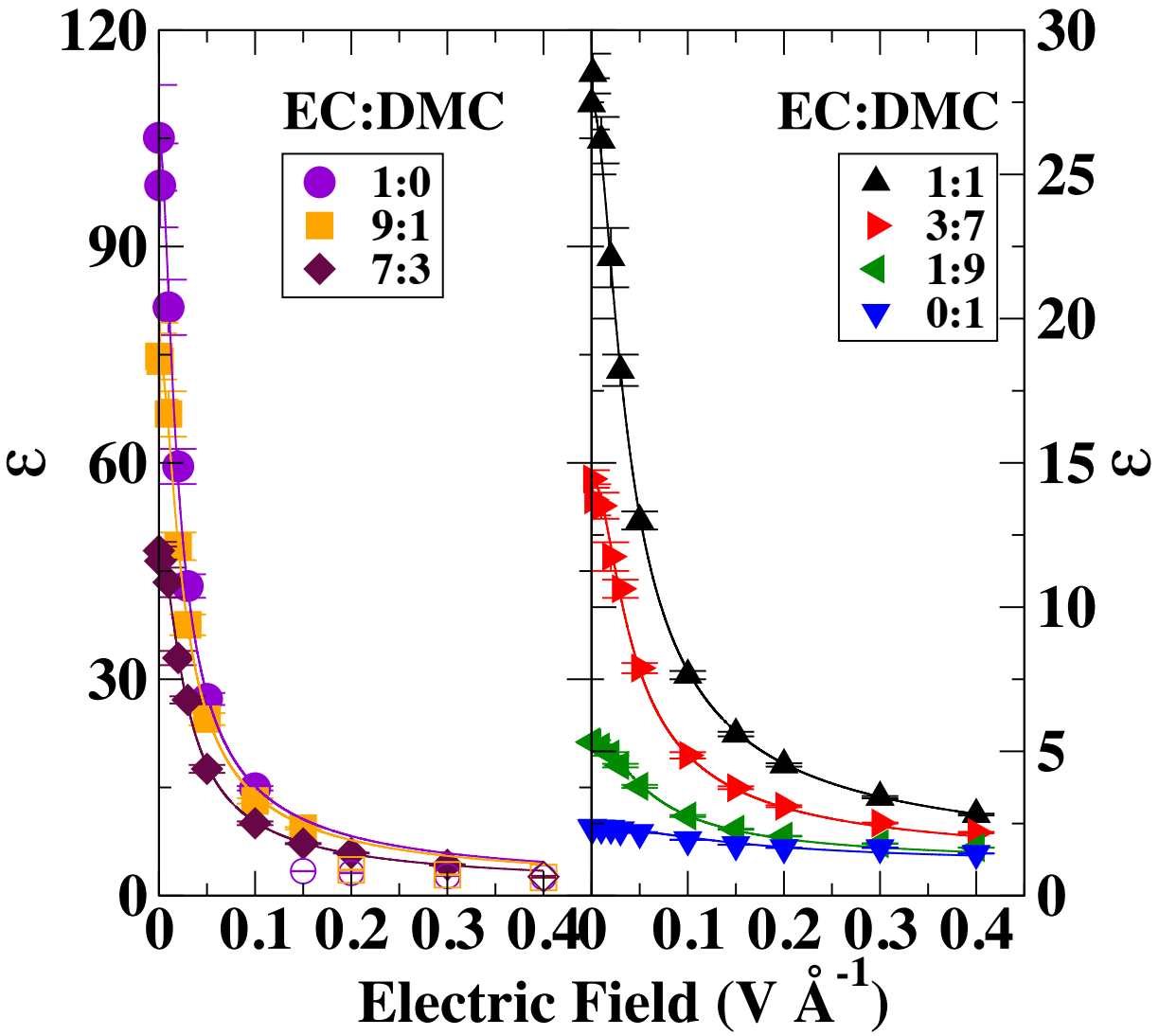

Figure 6.4: Booth Model for EC/DMC mixtures. Open symbols are used to denote samples where electric-field driven crystallization ("electrofreezing") has occurred. These points were excluded from the fitting.

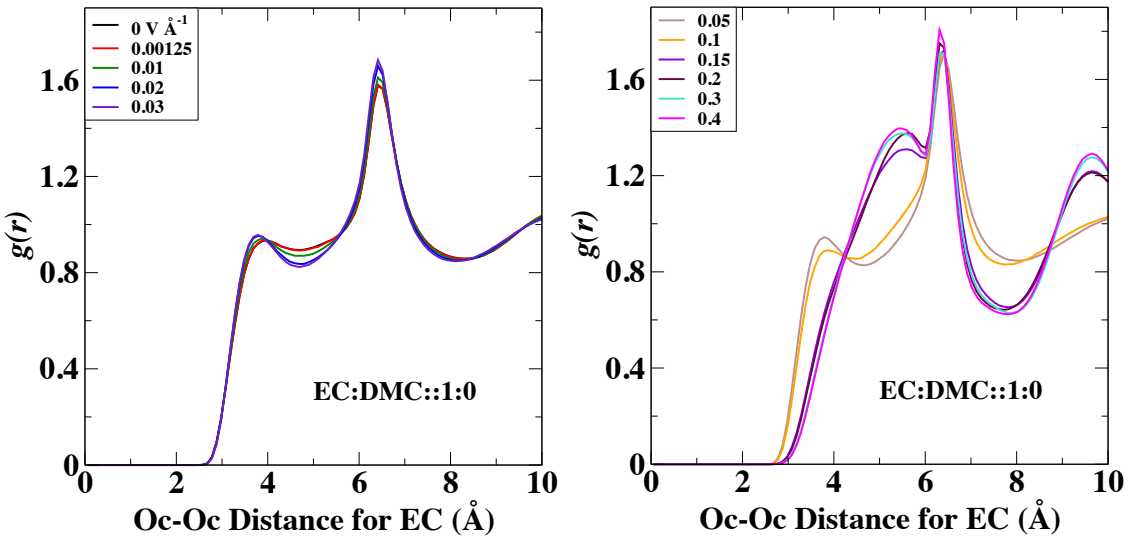

Figure 6.5: O_c-O_c RDF for EC:DMC mixture with ratio 1:0 ($x_{EC} = 1$) at a variety of electric field values

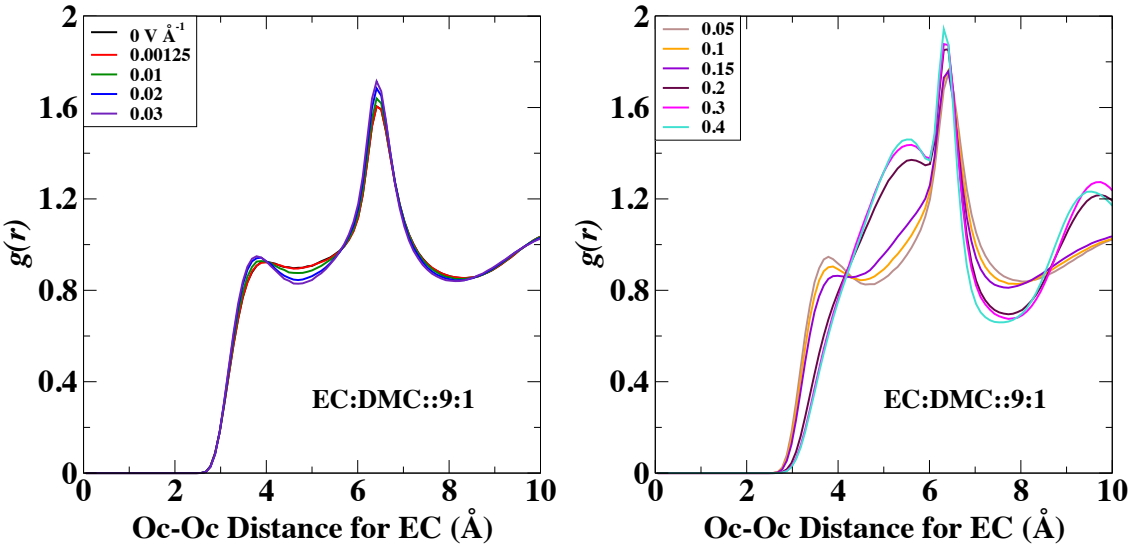

Figure 6.6: Same as Fig. 6.5 with a ratio of 9:1($x_{EC} = 0.9$).

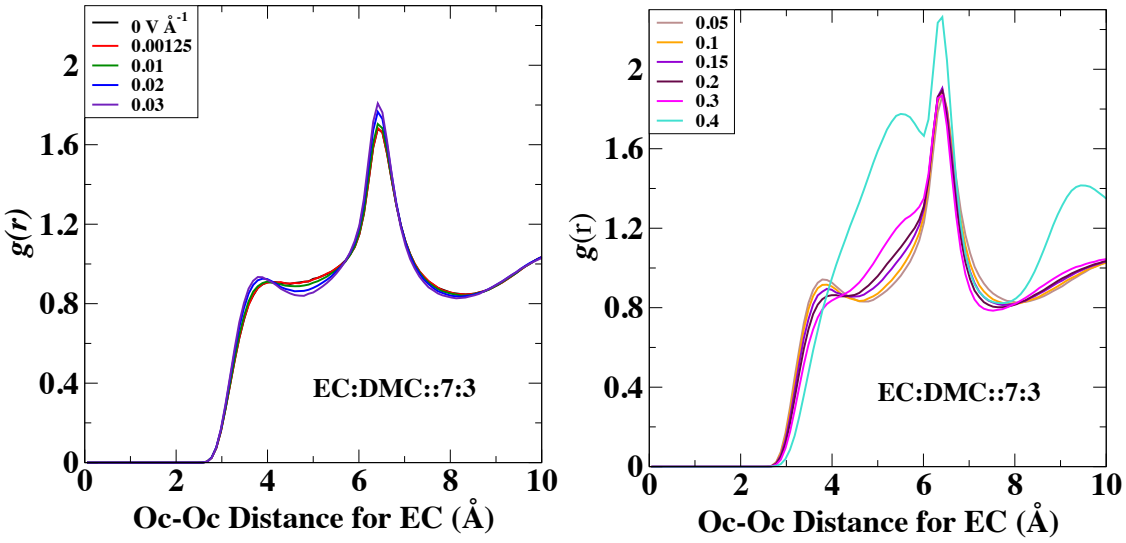

Figure 6.7: Same as Fig. 6.5 with a ratio of 7:3($x_{\mathrm{EC}} = 0.7$).

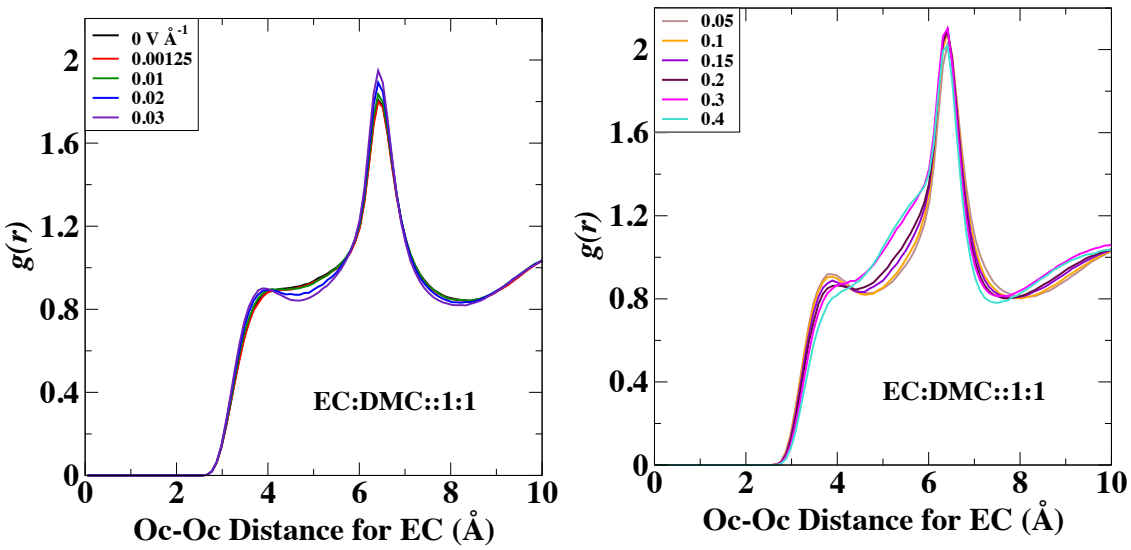

Figure 6.8: Same as Fig. 6.5 with a ratio of 1:1 ($x_{\mathrm{EC}} = 0.5$).

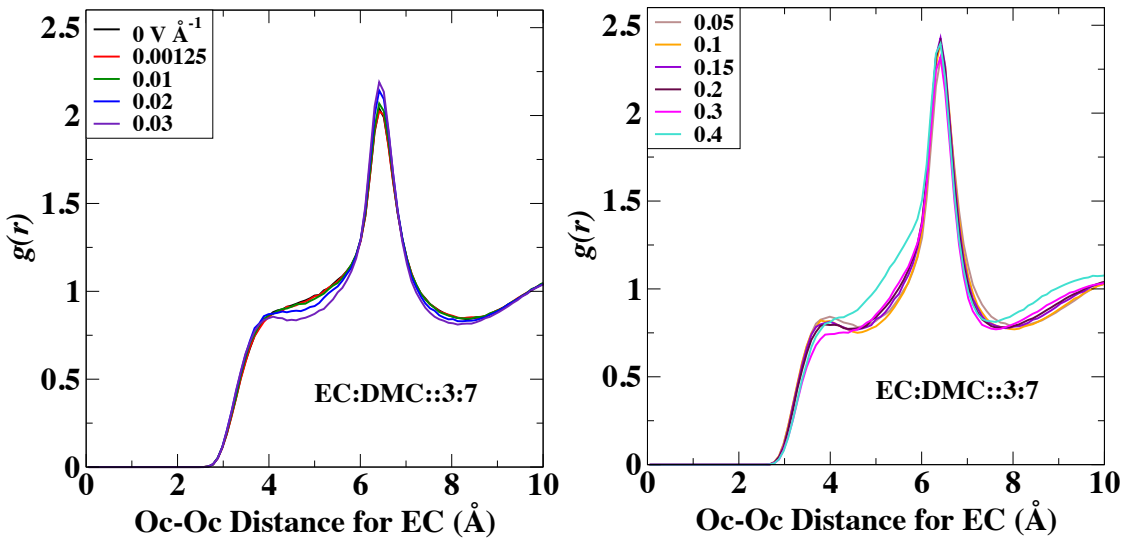

Figure 6.9: Same as Fig. 6.5 with a ratio of 3:7 ($x_{\mathrm{EC}} = 0.3$).

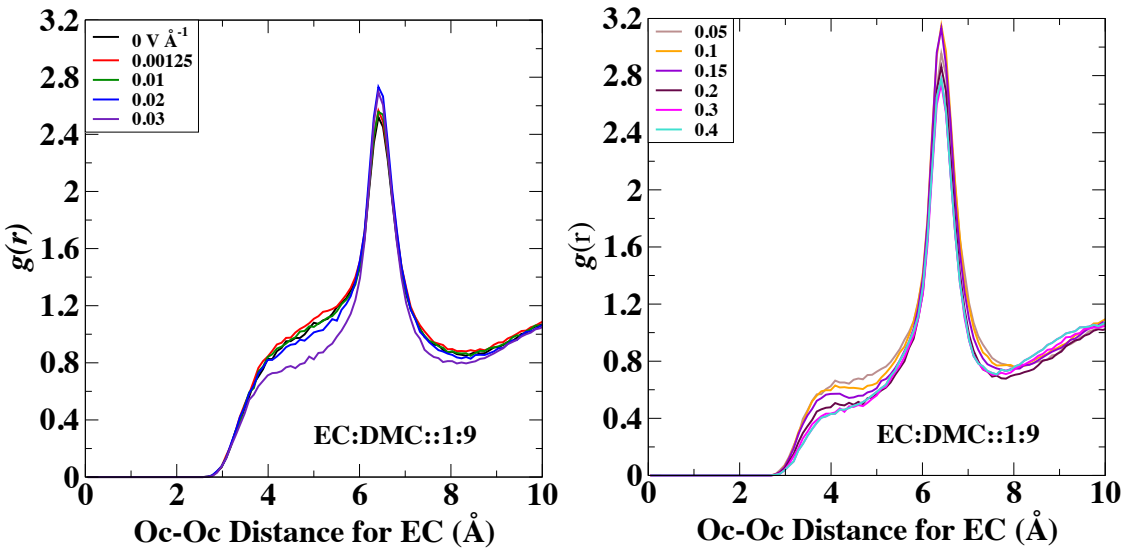

Figure 6.10: Same as Fig. 6.5 with a ratio of 1:9 ($x_{\mathrm{EC}} = 0.1$).

6.6 Electrofreezing

At fields of 0.1 to 0.15 V/Å, we notice a change in structure for pure EC in EC/DMC systems, in that structural layering occurs. This fundamental change in structure may explain the anomalous values we observe not only in this system, but all systems with these anomolously small values in

dielectric constant. We hypothesize that this layering occurred because the system is 'freezing' at these high fields. This is not unprecedented in the literature. Water has been found, in molecular simulations, to also freeze at high electric fields.[249]. We also examine snapshots for acetonitrile to determine if the origin of the anomalously low dielectric constants at high field arises from a similar cause. This structuring occurring for MeCN also correlates with our data on the dielectric constant with respect to field.

Examining the effect of electric field on dielectric constant is critical, because charging and discharging an energy storage device using an applied electric field is necessary to supply the energy of the storage system. Using MD, we have examined this effect for EC, PC, DMC, MeCN and EC/DMC mixtures. We fit our data to Booth's model and found good agreement with respect to our dielectric constant values for all systems at low field. The change in bulk structure with respect to electric field can also be found during examination of the RDF for the carbonyl oxygen atoms of EC molecules for the varying molar ratios of EC/DMC.

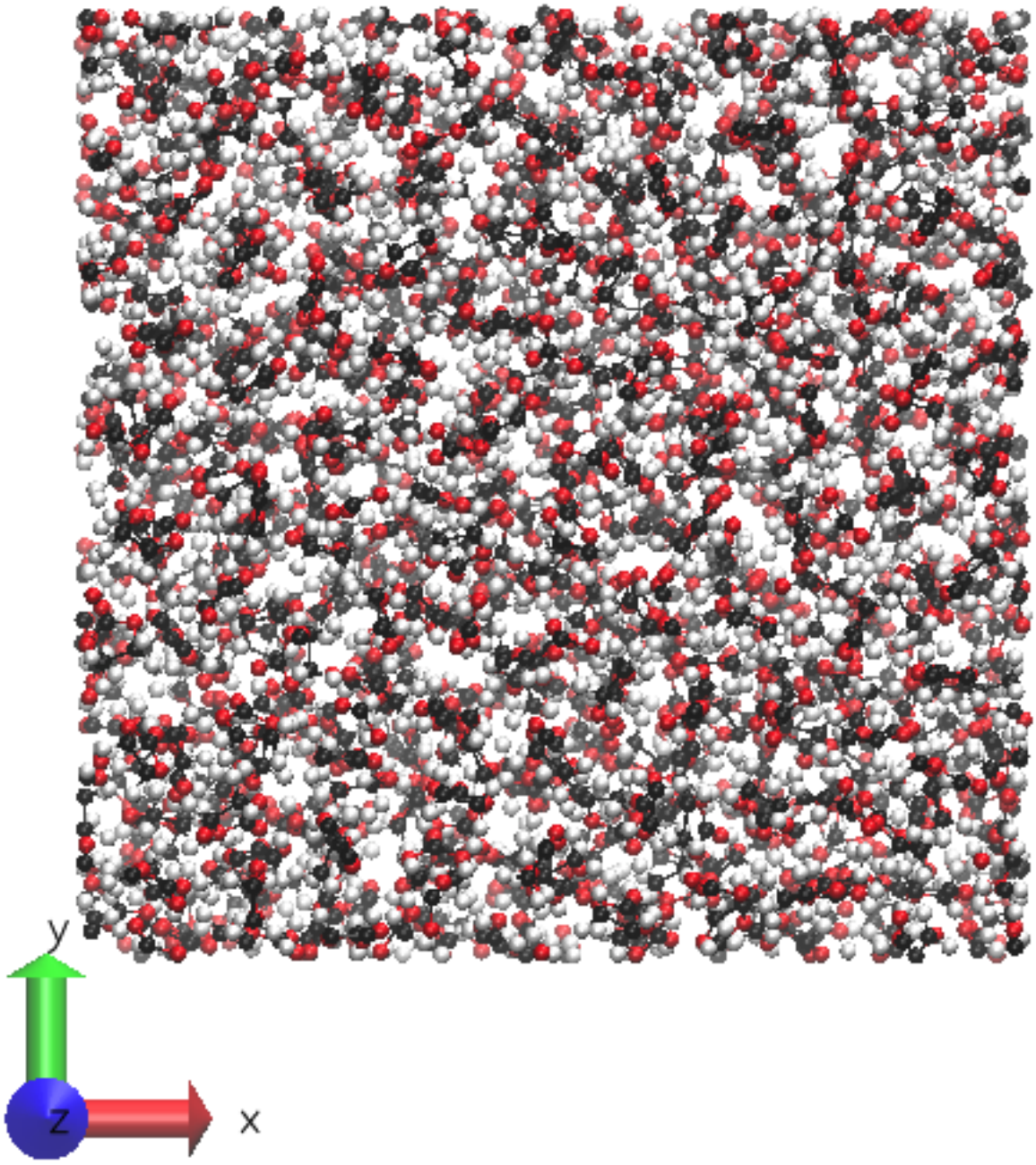

Figure 6.11: EC/DMC with molar ratio 1:0 ($x_{\mathrm{EC}} = 1.0$) under electric fields of 0.1 V/Å.

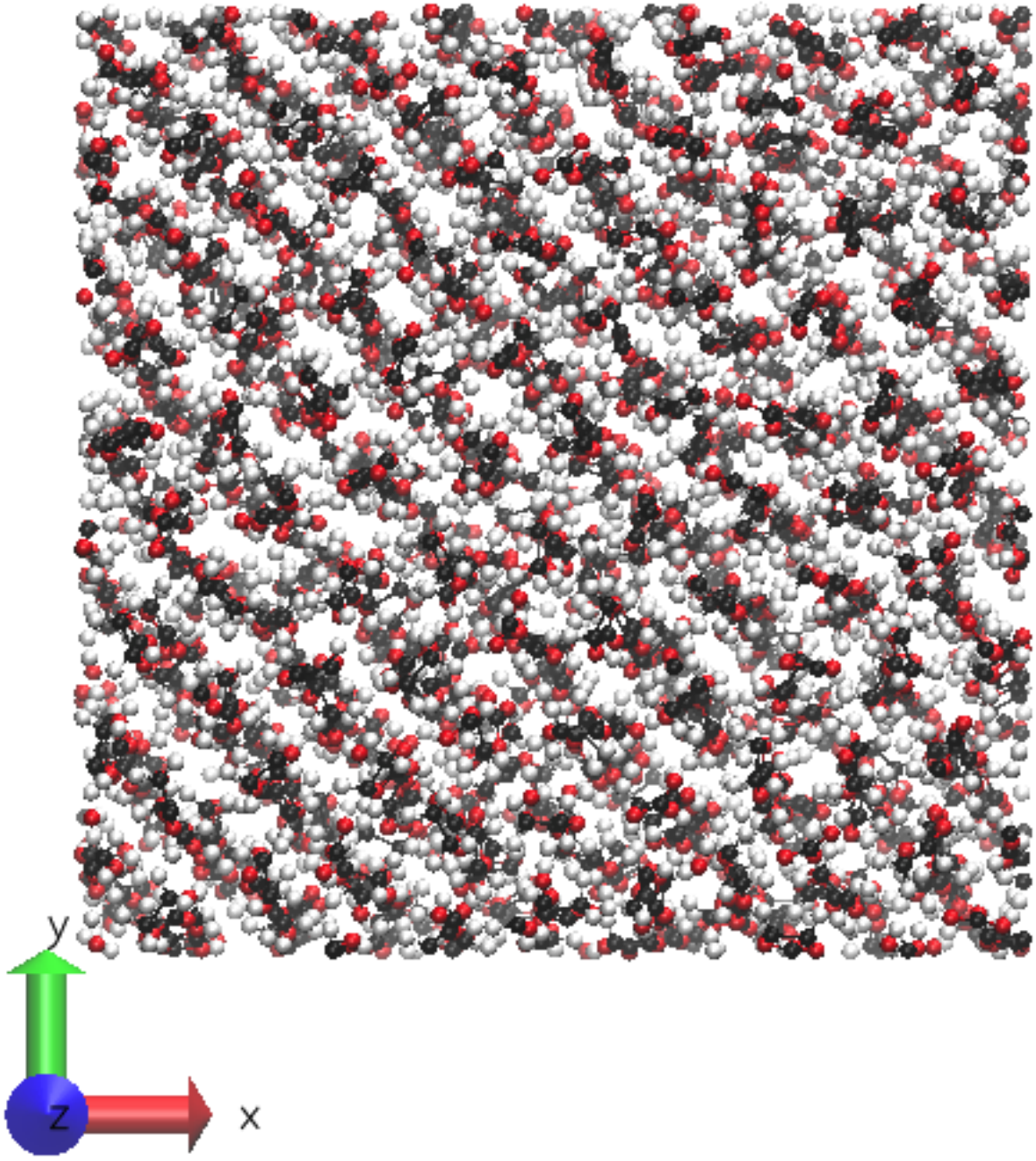

Figure 6.12: EC/DMC with molar ratio 1:0 ($x_{\mathrm{EC}} = 1.0$) under electric fields of 0.15 V/Å.

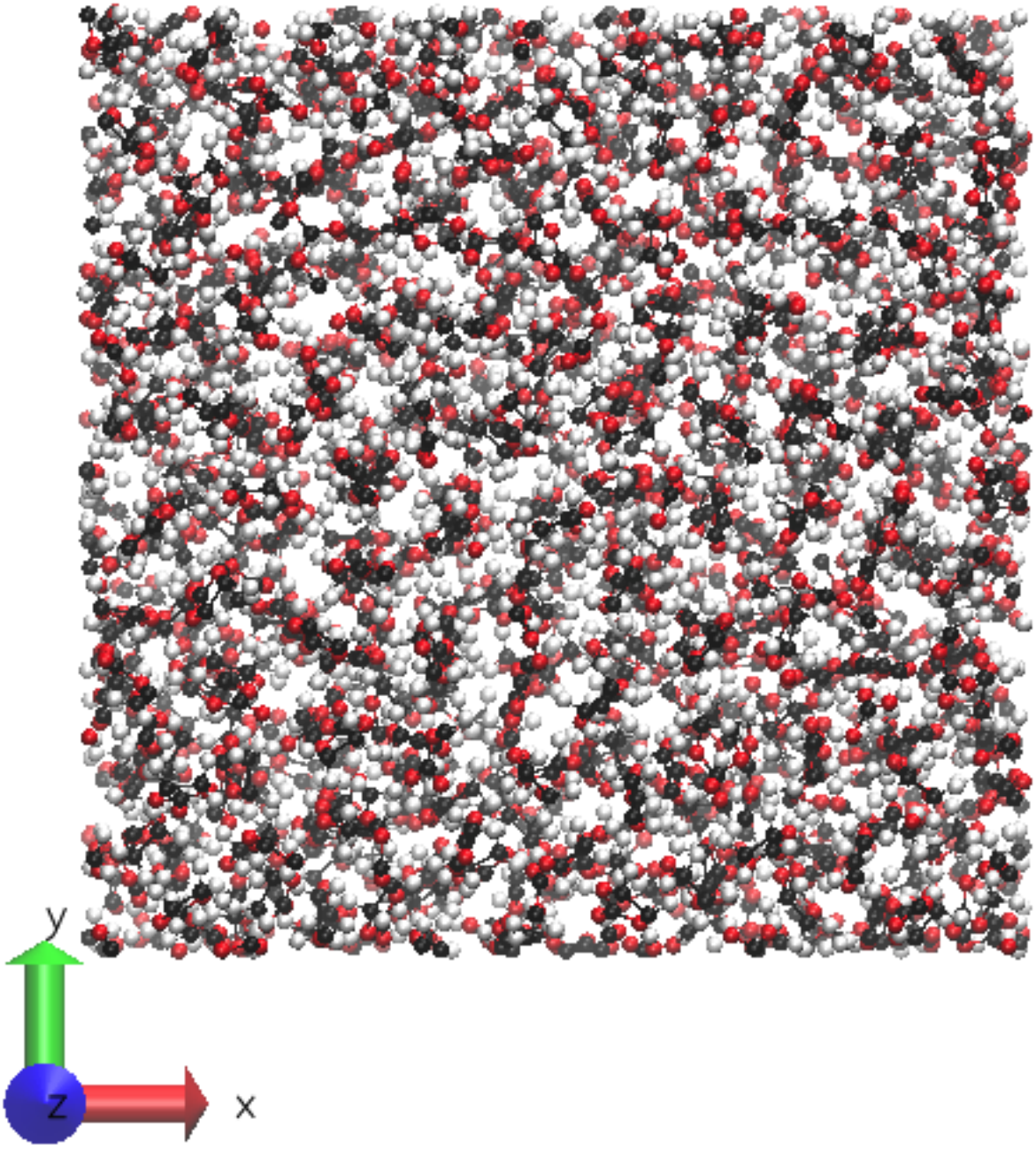

Figure 6.13: EC/DMC with molar ratio 9:1 ($x_{\mathrm{EC}} = 0.9$) under electric fields of 0.15 V/Å.

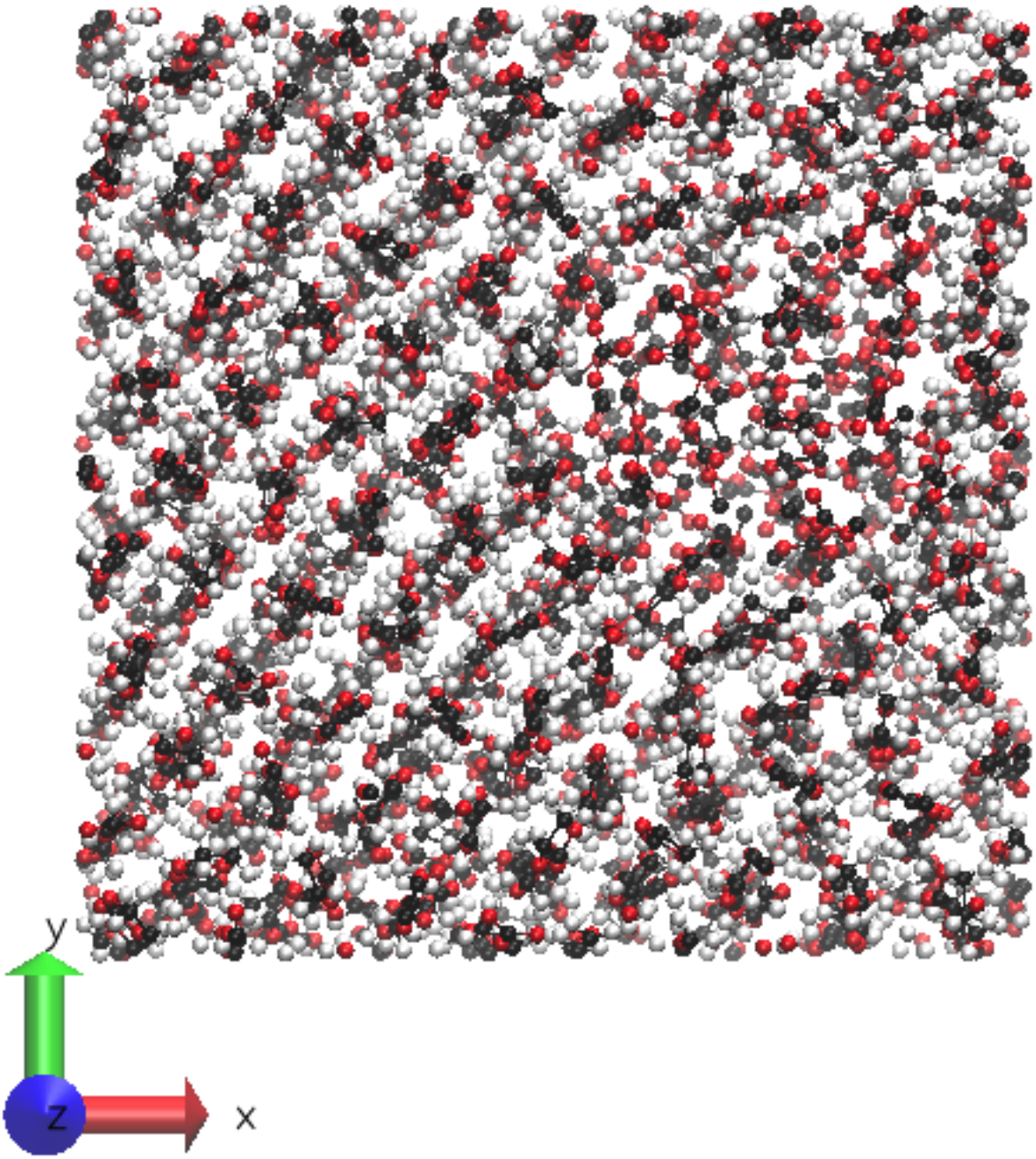

Figure 6.14: EC/DMC with molar ratio 9:1 ($x_{\mathrm{EC}} = 0.9$) under electric fields of 0.2 V/Å.

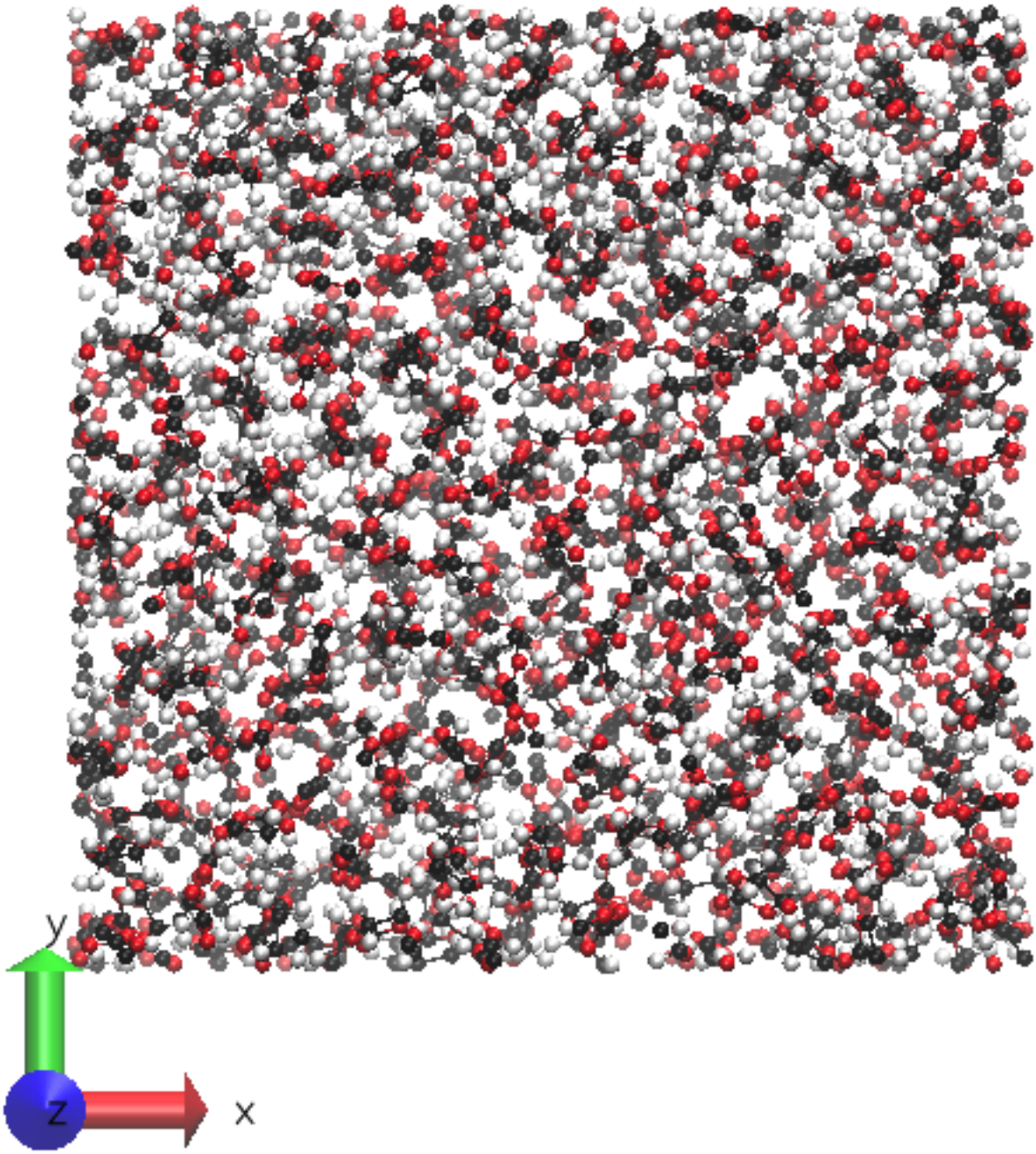

Figure 6.15: EC/DMC with molar ratio 7:3 ($x_{\mathrm{EC}} = 0.7$) under electric fields of 0.3 V/Å.

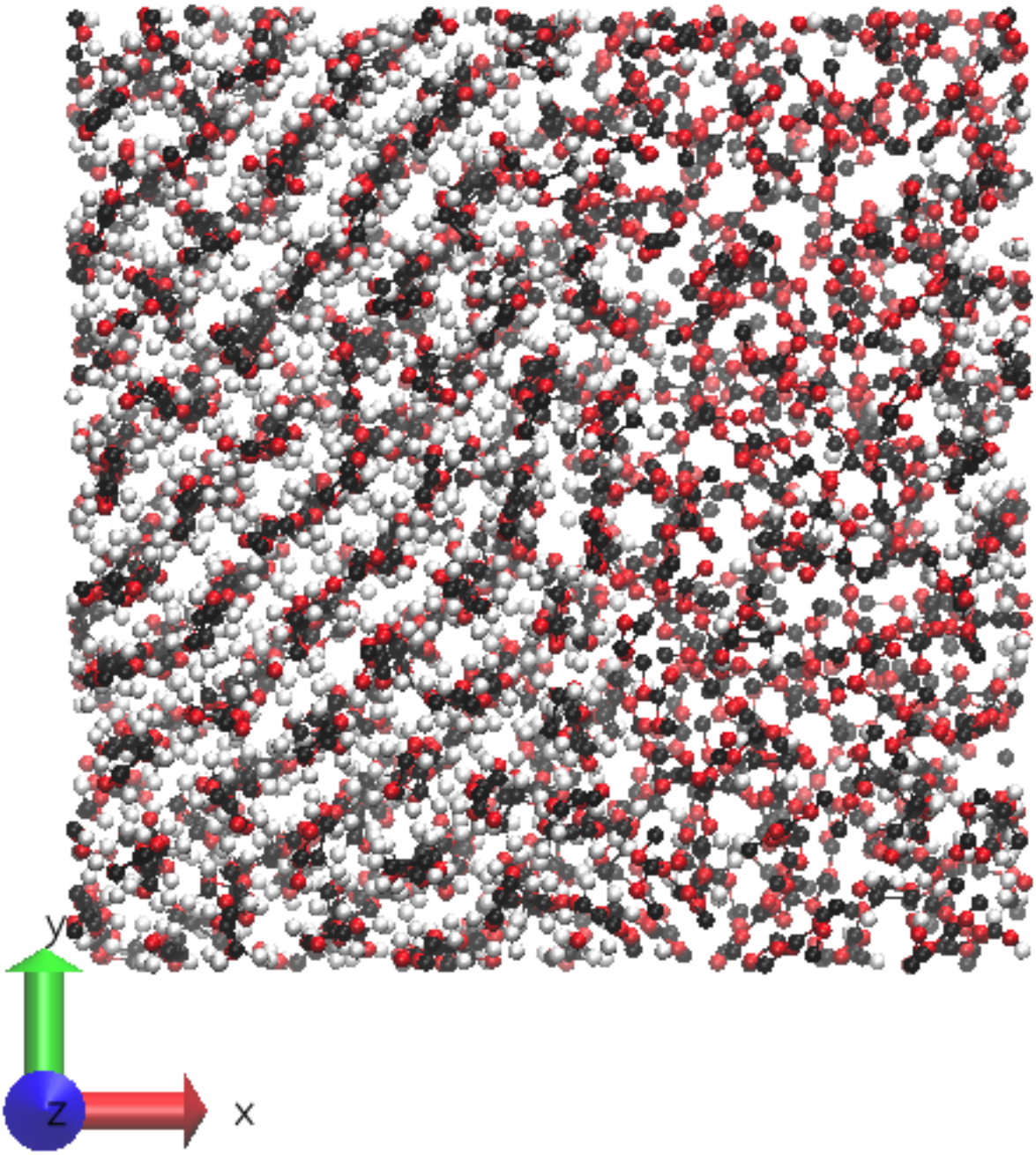

Figure 6.16: EC/DMC with molar ratio 7:3 ($x_{\mathrm{EC}} = 0.7$) under electric field of 0.4 V/Å.

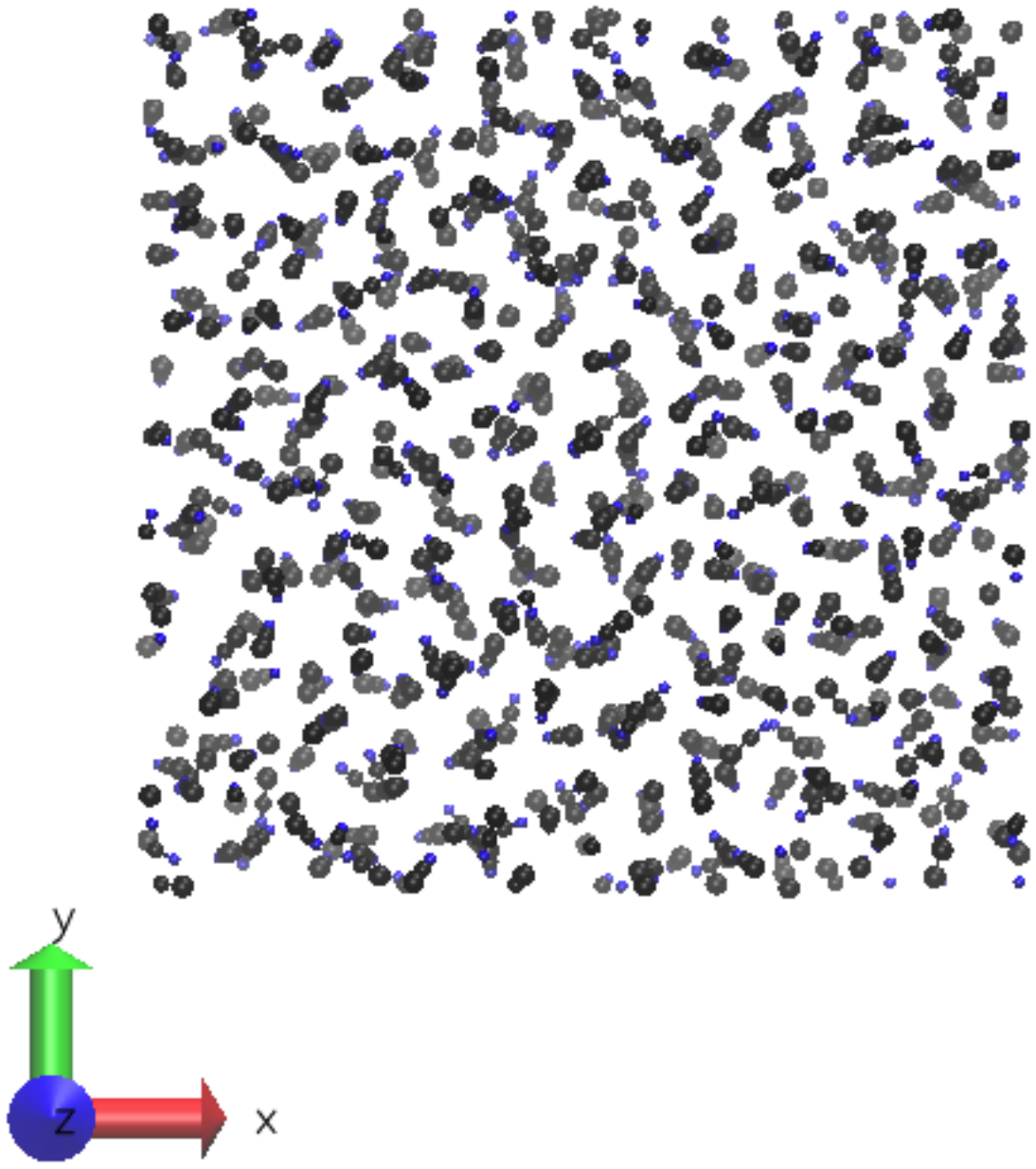

Figure 6.17: MeCN under electric field of 0.2 V/Å.

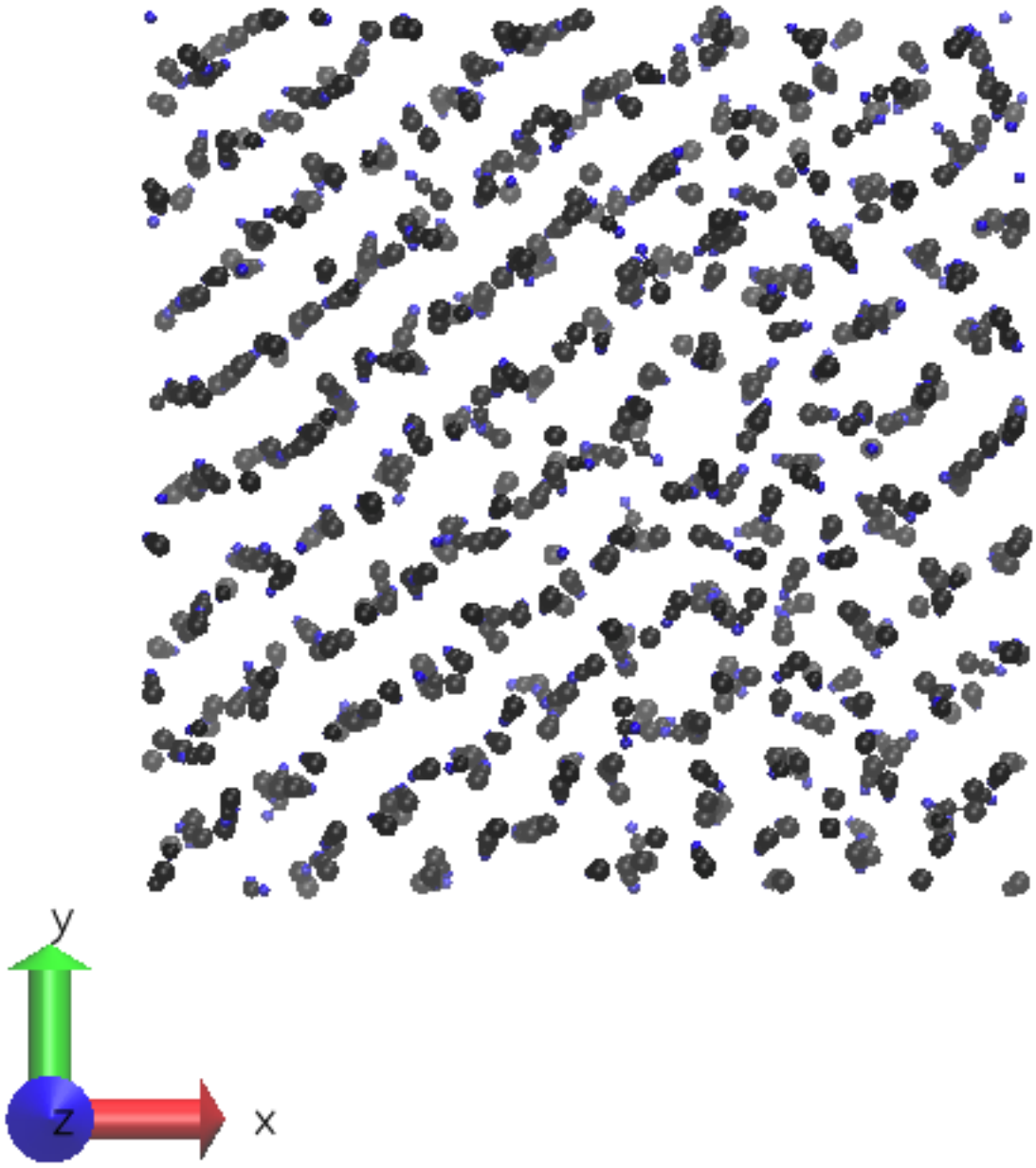

Figure 6.18: MeCN under electric field of 0.3 V/Å.

6.7 Conclusion

In this chapter, we have examined the effect of an applied electric field on both pure and mixed solvents. The effect of the electric field was investigated because understanding this effect allows for more accurate continuum modeling of Electric Double-Layer Capacitors. The solvents chosen for this investigation have dielectric constants that range from 0 to 4 V/Å. The force fields we used produced good agreement with respect to experimental values of density and dielectric constant. In contrast to Wang, et al., we fit all of our dielectric constant to the Booth Model instead of using Eq. 5.10, because the equation for the parameter modeling the effect of electric field on the dielectric constant was derived specifically for water when an electric field is applied. We demonstrated that qualitatively different values of β for acetonitrile are obtained depending on the method used to calculate β. We observe a qualitative difference in the value of β depending on the method used to calculate this variable. TThe Booth model works well as long as the systems that were observed to freeze are removed from the fitting. To explain these results we examined snapshots at the noted electric fields and discovered that the solvents become significantly more ordered, specifically that the system separated into layers, to a lesser degree for solutions containing DMC. Our Booth Model fits, for the systems that had electrofreezing at large electric fields, were fit well when these points were excluded from the fit. We also examined RDF plots for EC/DMC mixtures and that at a suitably large electric field, an additional peak appears for EC/DMC solutions having mostly EC. One hypothesis that explains these results is that the solvents have undergone 'electrofreezing', a process in which the solvent freezes under electric field. Future work is needed on this subject. These results should have immediate use for continuum models, specifically the value of β for acetonitrile we calculated.

Chapter 7

Effect of Salt Concentration on Dielectric Constant of Organic Solvents

7.1 Introduction

In this chapter, we examine the dependence of the dielectric constant on salt concentration in several organic solvents: acetonitrile (MeCN), propylene carbonate (PC) and ethylene carbonate/dimethyl carbonate (EC/DMC) mixtures. To determine that our force fields can faithfully represent existing experimental results for MeCN, we compare our data on dielectric constant and densities at several concentration with earlier experimental work for sodium iodide (NaI) and lithium bromide (LiBr) solutions. Simulations are also performed for sodium bromide (NaBr) and lithium iodide (LiI) solutions in order to determine the effect that changing one of the ions has on the dielectric decrement. The dielectric decrement is found to be significantly smaller for the NaBr solutions. Structural information was obtained through plotting the coordination numbers of the cations with respect to the nitrogen atom in acetonitrile (N(MeCN)) and large qualitative differences are observed between the NaBr solutions, and solutions of the other salts, specifically at relatively larger concentration. Snapshots of the simulations were taken to demonstrate the significantly different behavior of the ions in the solutions. We conclude that the anomolously low

dielectric decrement for NaBr is due to the extremely low solubility of NaBr in MeCN. Note that most of the NaBr precipitates out in the simulation, consistent with the experimental solubility of NaBr. We continue this chapter by examining the dielectric decrement of PC for NaI, LiBr and NaBr. There is work in the literature regarding the dielectric constant of PC solutions of NaI,[250] Li triflate[251] and Li imide.[251] Qualitative observations will be noted for the effect of molar composition of EC on the dielectric decrement.

7.2 Simulation Procedure

We begin the work by first calculating the equilibrium densities for the solvent/ion mixtures using constant *NPT* MD simulations. As in the previous chapter we used the molecular simulation code LAMMPS[237] to perform MD simulations. All simulations are performed at 298 K, with the exception of EC/DMC systems. We sued minimization for all systems save for those with MeCN. Simulations are performed with a damping parameter of 100 fs, using the Nosé-Hoover thermostat, with a time-step of 1.0 fs. An Andersen barostat is set to maintain a pressure of 1.0 atm for all *NPT* simulations (unless otherwise specified). We used the code Packmol[238] to generate initial coordinates for most of our systems, or removed ions from a run of a system to obtain a lower concentration system, the latter of which we did to obtain the systems at lowest non-zero concentration for NaI and LiBr solutions. For acetonitrile, we used a damping parameter of 500 fs because of the instability reported in Chapter 6 for a smaller damping parameter, 1000 fs used for simulations containing PC and ions (100 fs for pure PC), and 100 fs for simulations containing DMC. We used 1000 fs for the damping term for the barostat for PC systems containing ions because in a previous simulation (with a different model for NaI) the system became unstable and the simulation prematurely ended with a damping term of 100 fs. We also used 1000 fs for simulations solely containing EC and ions (100 fs for pure EC).

We examine salt solutions of NaI and LiBr at at concentrations close to those of experiment[16] in order to test our force fields. To better observe the trends we also examined several other

Atom	Color
Iodine	Green
Bromine	Purple
Sodium	Yellow
Carbon	Black
Nitrogen	Blue
Hydrogen	White

Table 7.1: Legend for colors used for atoms in chapter.

concentrations beyond those studied in the experiment. An inner cutoff of 10.0 Angstroms and and an outer cutoff of 10.1 Angstroms were used for the non-bonded interactions in our system.

For MeCN, EC, PC and DMC, we used the same force fields described in Chapter 6. For the ions, we used force field parameters from OPLS 186, because of the widespread use of the force field in the literature.

Atom Type	σ (Å)	ε (kcal/mol)	q (e$-$)
Na^+	1.897439957	1.60709	1.000
Li^+	1.259920001	6.24982	1.000
Br^-	4.623764331	0.09	-1.000
I^-	5.4	0.07	-1.000

Table 7.2: LJ and charge parameters for ions.

7.3 Validation of Force Fields

We compared our results for the dielectric constant 'decrement' for NaI and LiBr solutions (fraction of dielectric constant maintained at each concentration compared to that with no salt) with the experiment of Barthel et al.[16] We used the fraction in our plots instead of the calculated value of the dielectric constant because the dielectric constants calculated by us with respect to experiment are different and this method ensures a more accurate comparison. These results are shown in Figure 7.2. Our data for the dielectric decrement for NaI and LiBr solutions agree qualitatively with those of experiment, which is promising because we use non-polarizable point charges to describe our systems. However, this may explain the quantitative differences observed, because polarization will significantly alter the interactions between the solvent molecules and the ions.

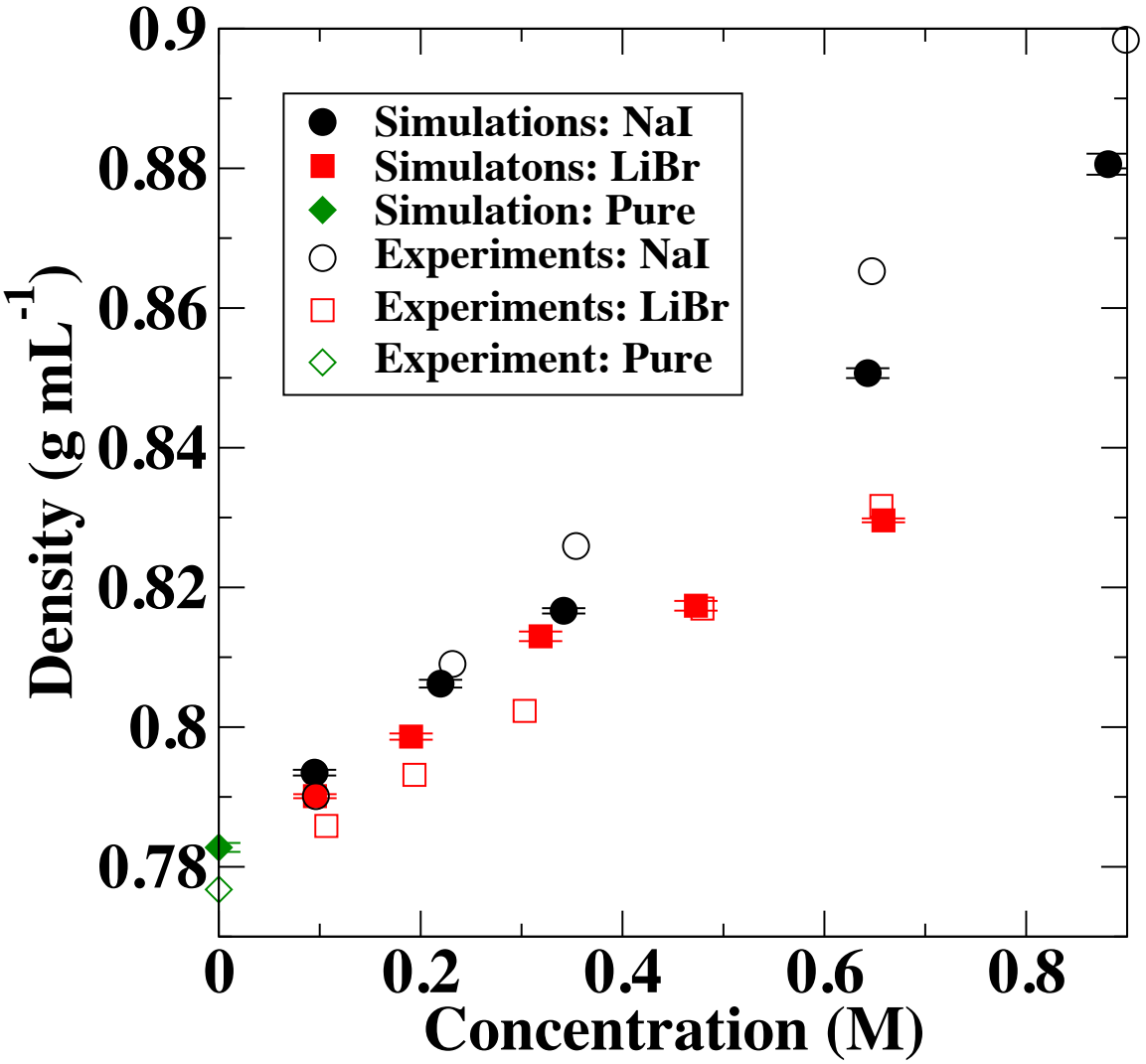

Figure 7.1: Density of salt solutions of MeCN as a function of concentration. Experimental data from Ref. 16.

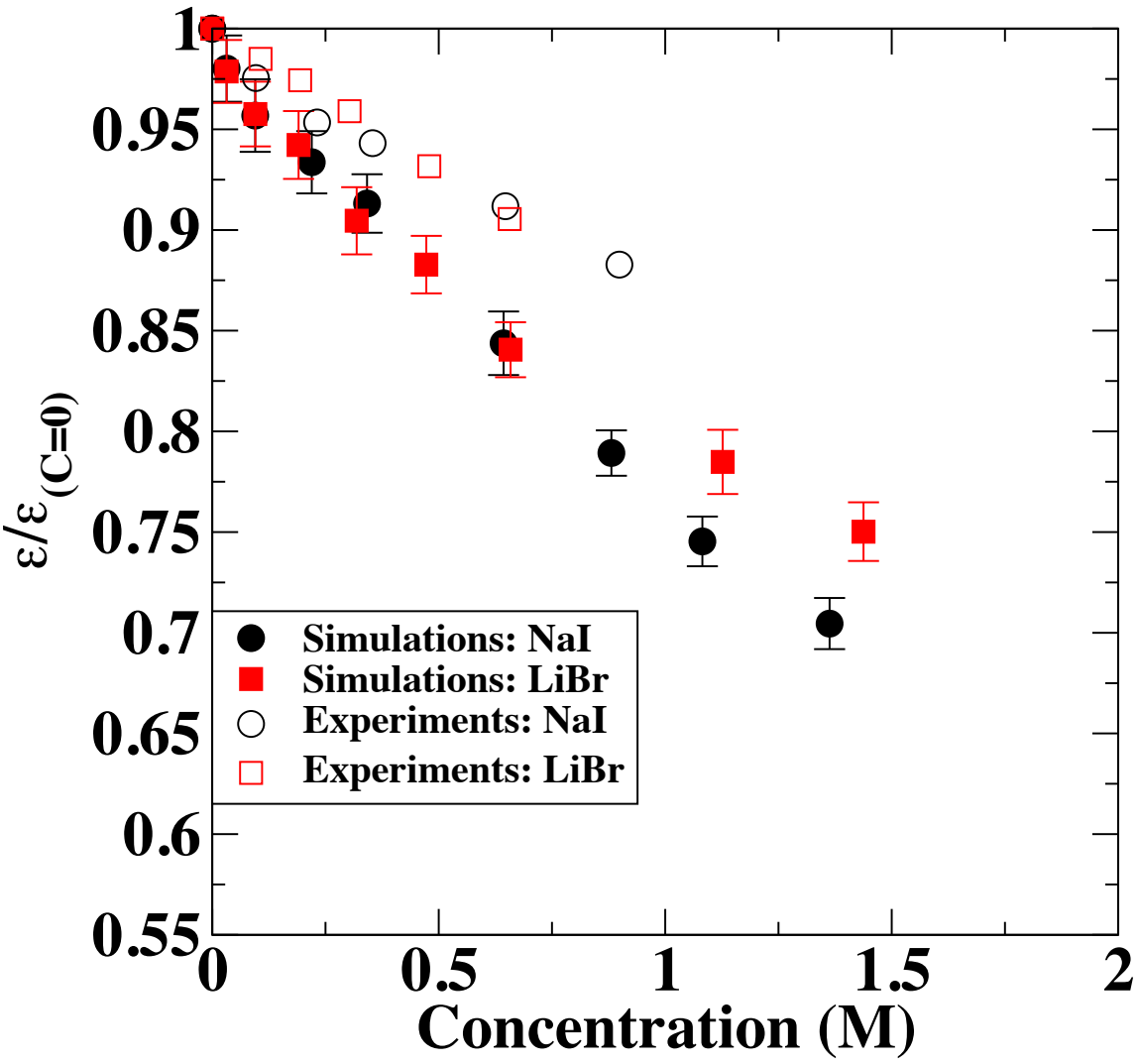

Figure 7.2: Dielectric constant of MeCN electrolyte solutions relative to that of pure MeCN as a function of salt concentration. Verified with respect to experimental data from Ref. 16.

The densities of salt solutions are calculated and show good agreement with experiment.[16]

7.4 Dielectric Decrement for MeCN Solutions

With our force fields shown to give reasonable agreement with experiment, we can calculate the dielectric constants with respect to concentration for other salt solutions, specifically NaBr and LiI solutions, to examine the effect of varying the ions. To accomplish this, we supplement our dielectric data with structural information, specifically coordination numbers. Results for the coordination number for the nitrile N in MeCN with respect to concentration are shown in Figure 7.4. We observe qualitatively different behavior for each salt regarding the effect of concentration on coordination number. We observe little change for NaI and LiI salts, even with a concentration over 1 M. As shown in Fig. 7.3 the decrement occurs at approximately the same rate with respect to concentration. We infer from this linear behavior that the number of solvent molecules surrounding one ion is relatively constant, which can be justified by noting that the mechanism of dielectric decrement has some measure of dependence on the solvent molecules becoming relatively fixed by the electric field of the ions thus a system in which the coordination number changes little would indicate that the dielectric constant should decrease in qualitatively linear trend. We expect that the coordination number of the ions will decrease, which will lead to qualitatively different behavior. For LiBr, we note that the coordination number decreases with respect to concentration. This observation gives an explanation concerning the result the dielectric decrements for NaI and LiBr solutions are similar at low concentrations, but that for LiBr becomes noticeably smaller than that of NaI at high concentration. Finally, we note that the coordination number for NaBr is significantly smaller that that of NaI, LiBr and LiI. This behavior can be explained by hypothesizing that the salt atoms are agglomerated together, making solvation significantly difficult. This also agrees with our results that the dielectric decrement is the smallest for NaBr. For LiI, we note that the coordination changes gradually, which corroborates our earlier data showing the relatively linear dielectric decrement of LiI.

Visual representations of the electrolyte solutions are created for NaI and NaBr systems at several concentrations in order to discern if we can easily note the qualitative differences in coordination number. Figures 7.5 and 7.6 show all ions and all solvent molecules within 4 Å of any

of the ions. Solutions containing NaBr appear to have significant aggregation of ions. This should inhibit the cations from achieving a larger solvation shell, which is reflected in the data for coordination numbers. For NaI solutions, we note that several solvation shells for sodium ions can be observed, which agrees with our previous data. For the snapshot of the NaBr solution at 0.35M, the ions are clustered together, which indicates precipitation is occurring.

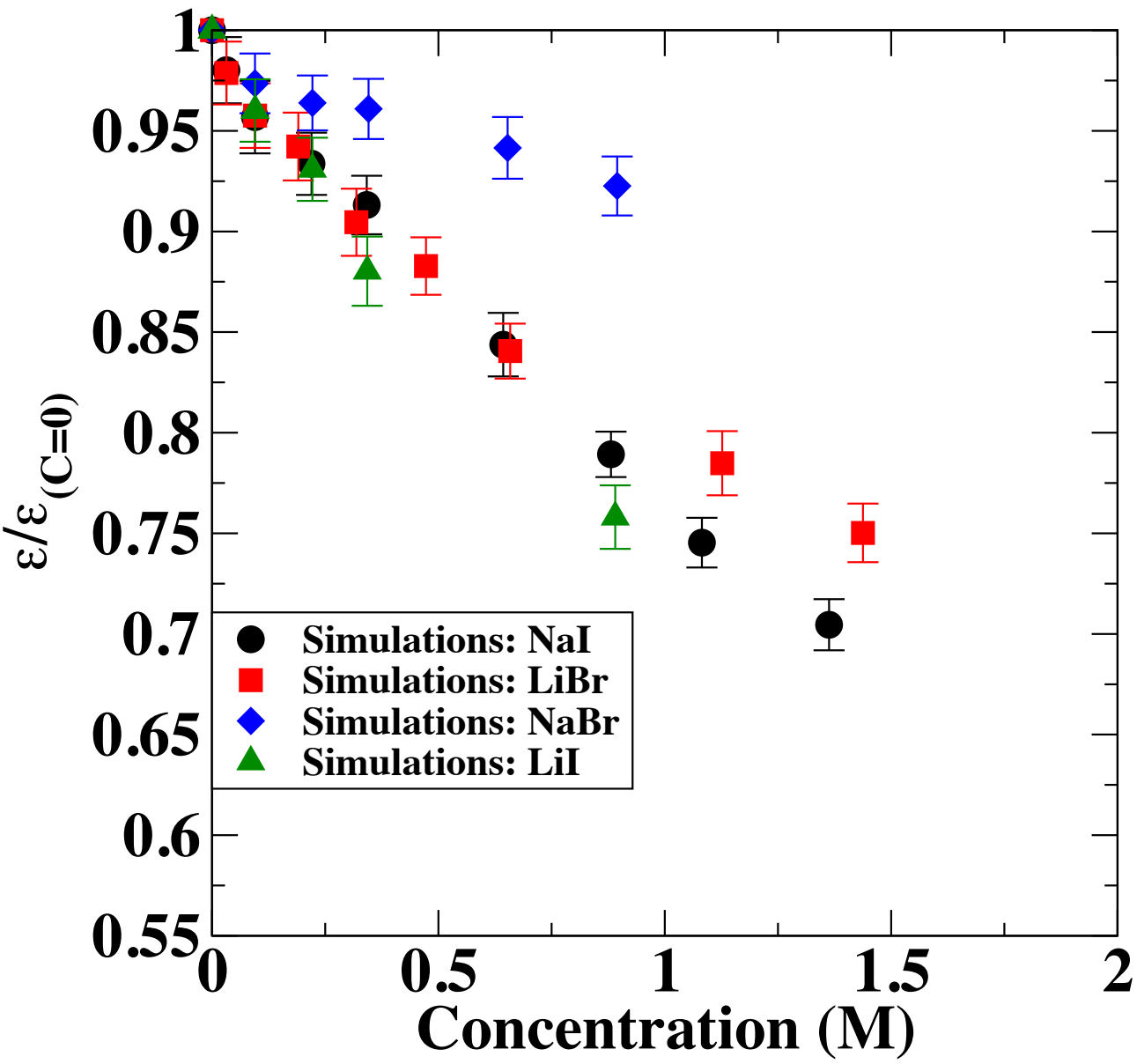

Figure 7.3: Dielectric constant of MeCN electrolyte solutions relative to that of pure MeCN as a function of salt concentration. Verified with respect to experimental data from Ref. 16.

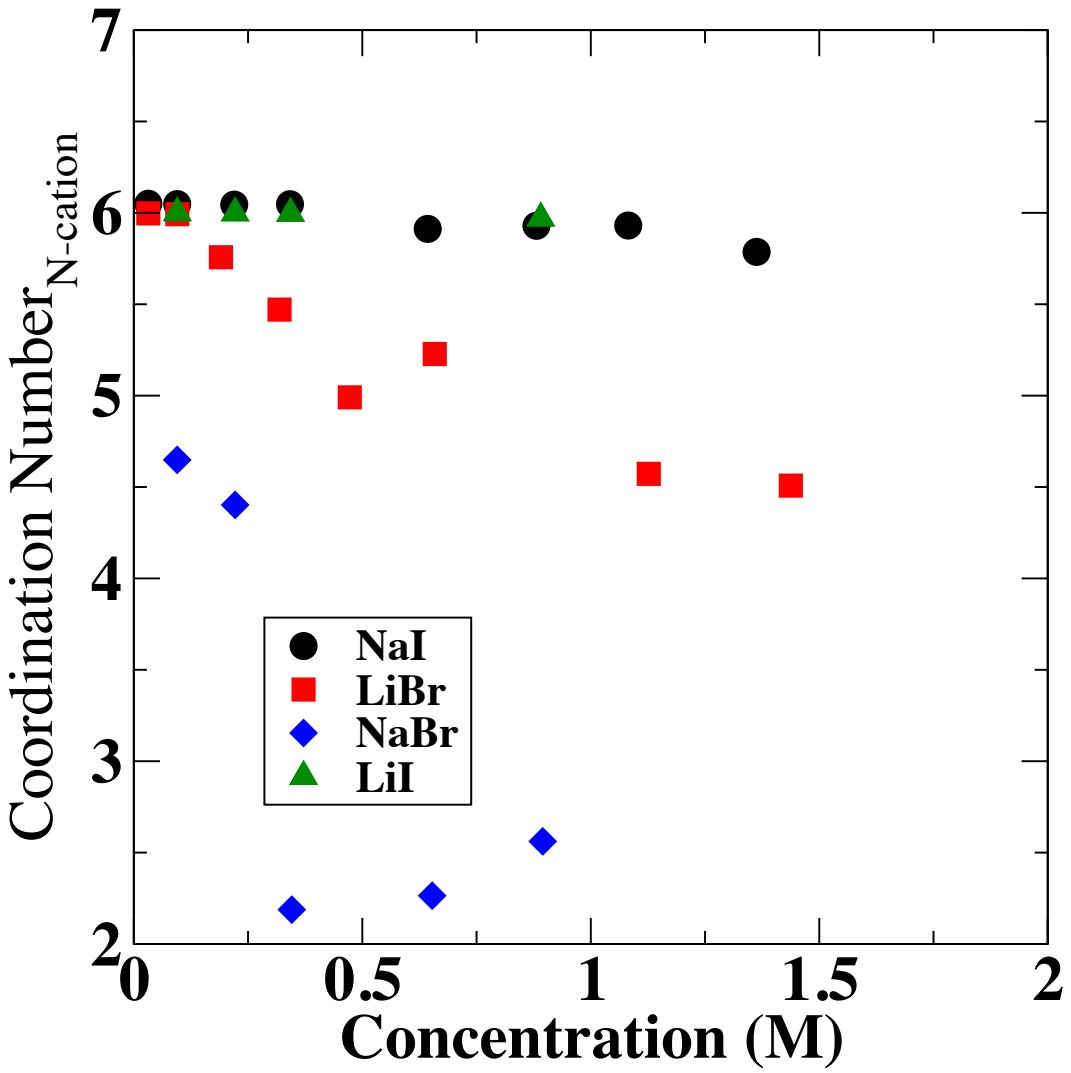

Figure 7.4: Coordination number around the cation for various MeCN/salt electrolyte solutions as a function of salt concentration.

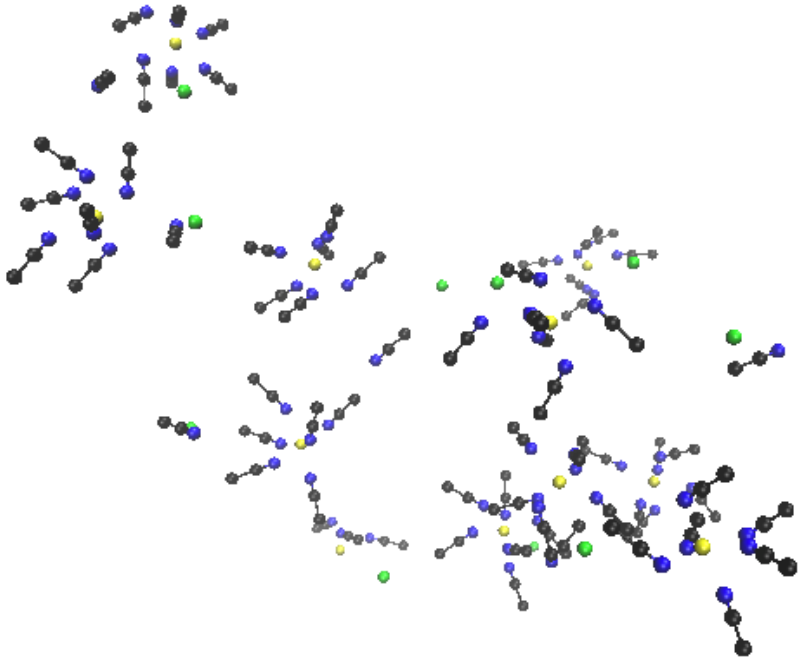

Figure 7.5: Snapshot of simulation of 0.34 M NaI/MeCN solution.

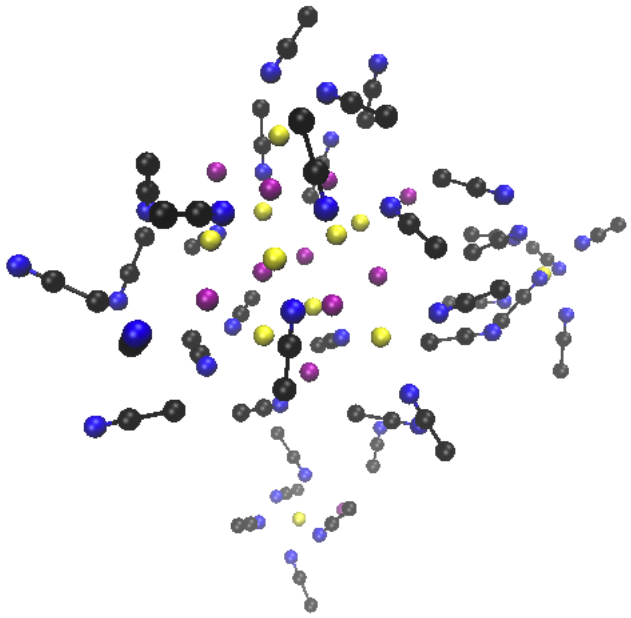

Figure 7.6: Snapshot of simulation of 0.35 M NaBr/MeCN solution.

Figures 7.7-7.12 display the coordination number of ions types with respect to one another: Na^+-Na^+, Na^+-anion, and anion-anion plots. In this way we determine if a particular type of ion aggregation is favored in the NaBr solutions. As shown in these figures, coordination numbers for NaI solutions are lower than those of NaBr solutions at shorter inter-ionic distances. Thus, solvation shells of cations should remain unperturbed at these concentrations, which is reflected in our data above with regard to coordination number. For NaBr solutions, at the three highest concentrations displayed in the plots, coordination number significantly increases at larger distances. This agrees with our observation that the coordination number dropped significantly between 0.22 M and 0.35 M. For Na-Na and Br-Br plots, the data, despite some noise, continuously increases in a significant manner. By contrast, plateauing occurs for Na-Br systems, which could indicate that solvation shells of ions is occurring.

7.5 Dielectric Decrement for PC and EC/DMC Solutions

To examine the dielectric decrement of other solvents, we also calculated the dielectric constants of PC with respect to NaI, LiBr and NaBr salt concentration and the dielectric constants of varying molar ratios of EC/DMC containing NaI. Examining solvent mixtures gives insight into how the decrement is affected by the relative molar composition of EC. For the data of PC, the effect of dielectric constant is very similar for the three salts solutions, which suggests the solvation structure is also similar. The relatively large error bars (especially for NaBr solutions) indicate the simulations can be run for a longer amount of time to achieve better convergence. Our data for most EC/DMC mixtures also have general monotonic behavior, with exceptions of solutions containing 0.9 molar fraction and 1.0 molar fraction DMC. This data suggests that few if any solvent molecules are held fixed by the electric fields generated by the ions.

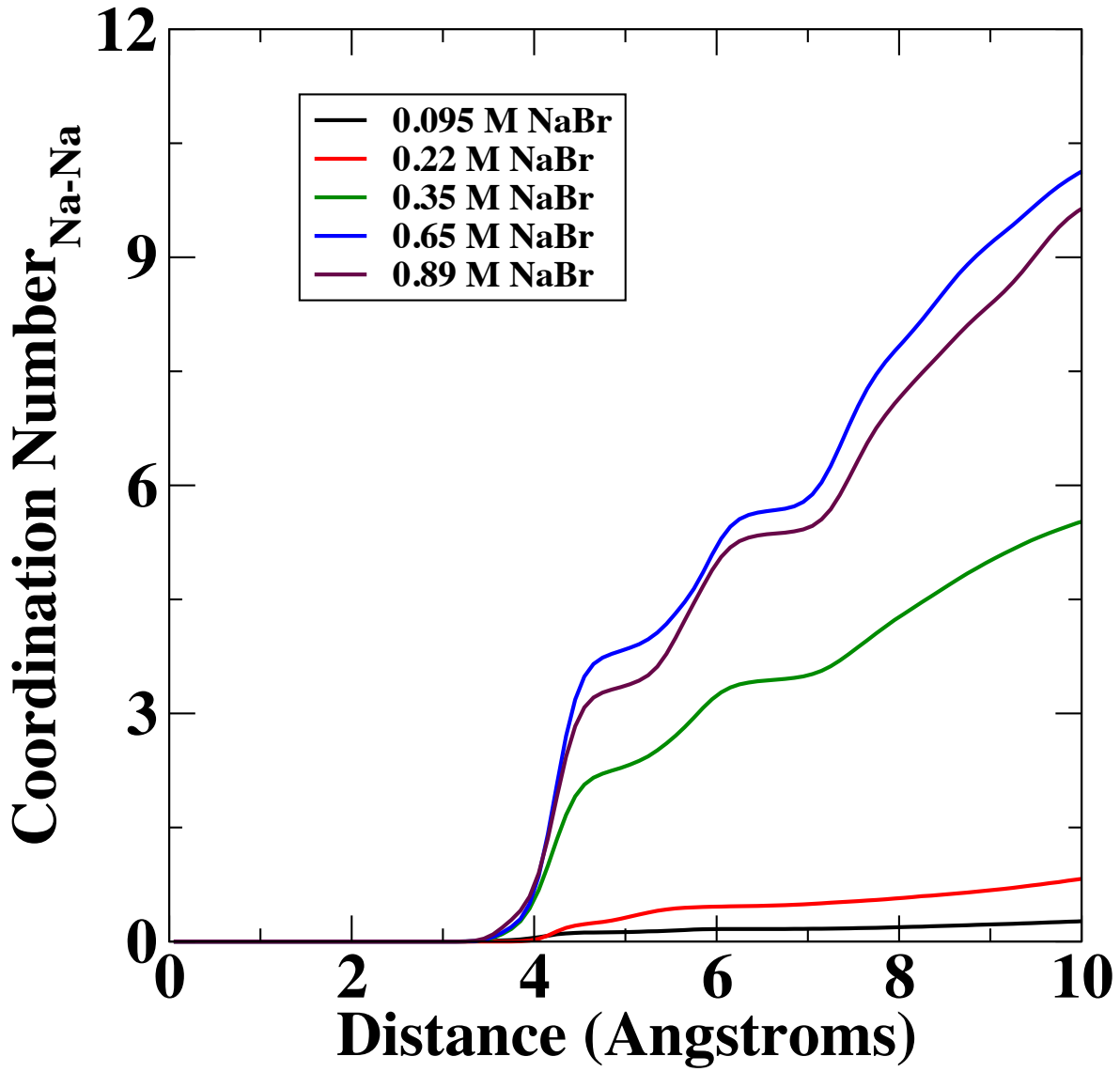

Figure 7.7: Coordination number of Na with respect to Na in MeCN solution containing NaBr.

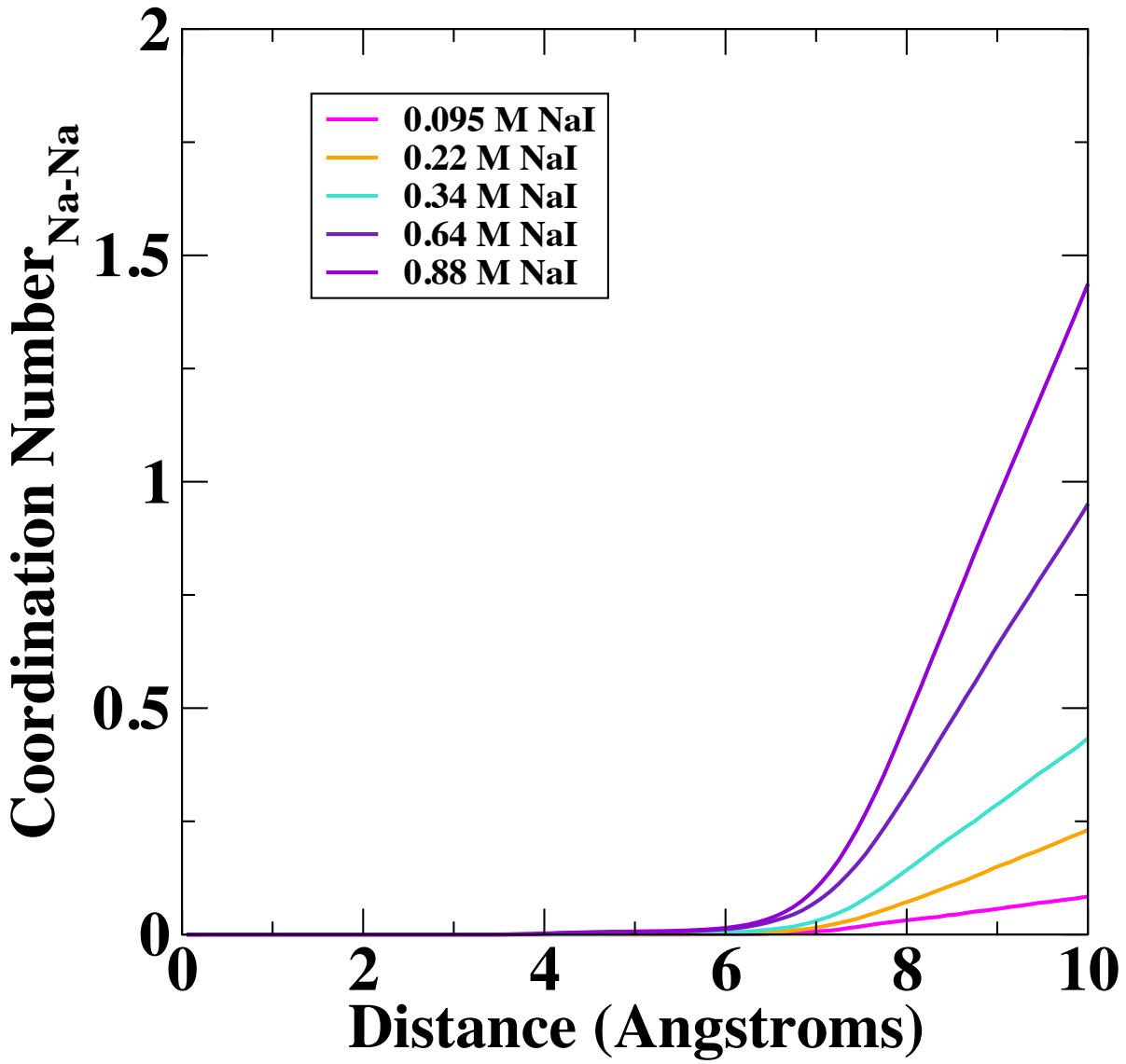

Figure 7.8: Coordination number of Na with respect to Na in MeCN solution containing NaI.

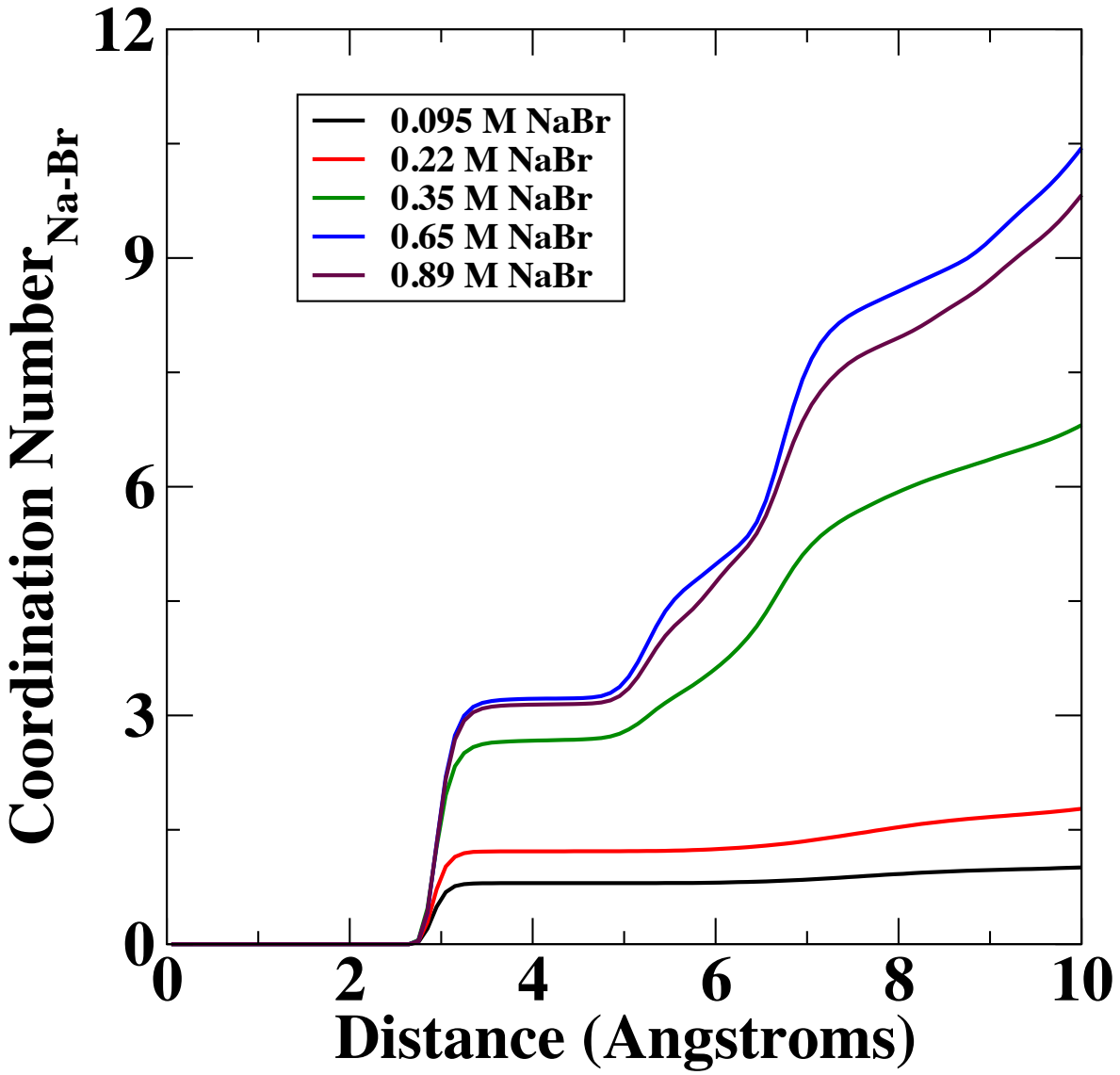

Figure 7.9: Coordination number of Na with respect to Brin MeCN solution containing NaBr.

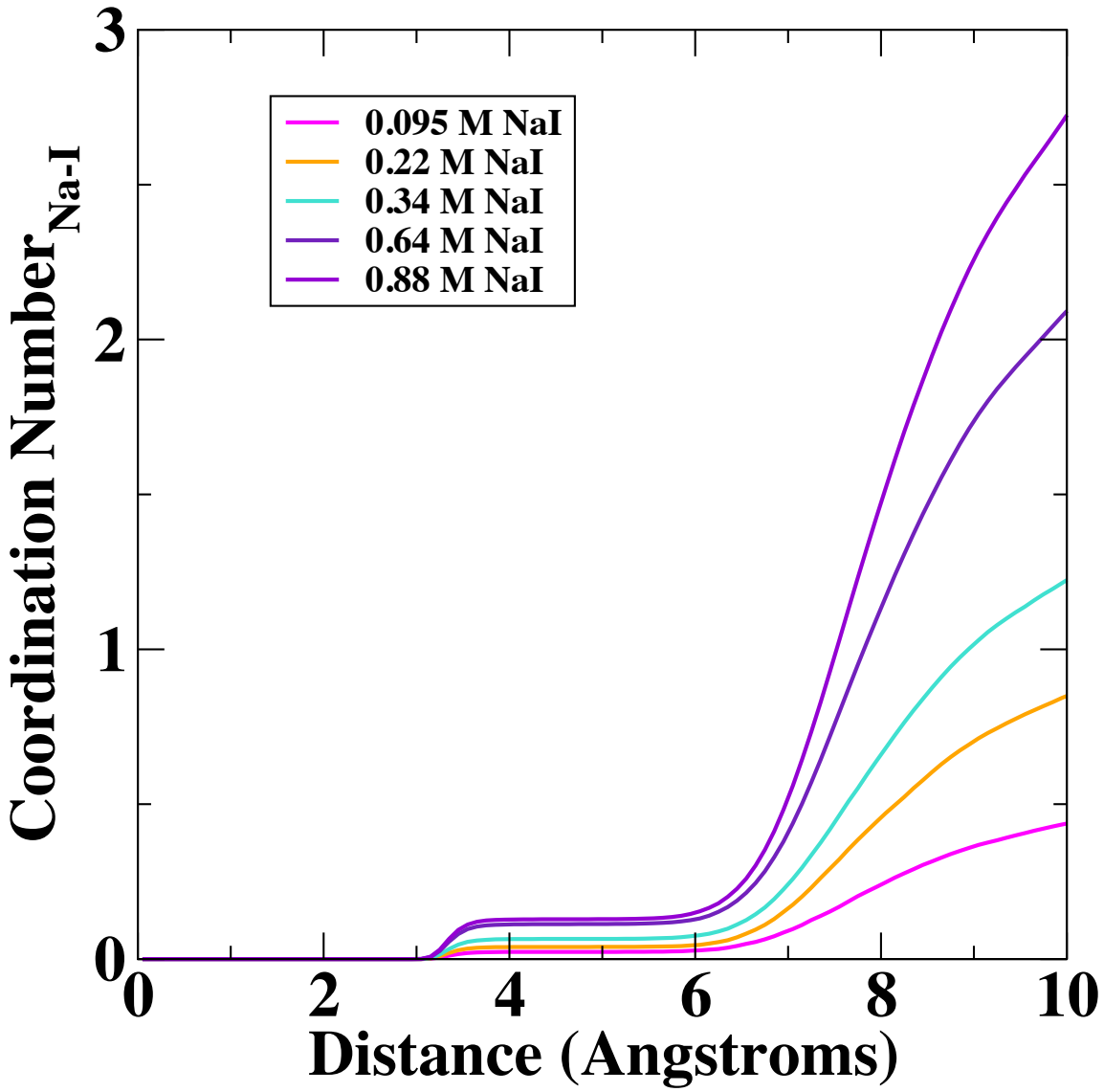

Figure 7.10: Coordination number of Na with respect to I in MeCN solution containing NaI.

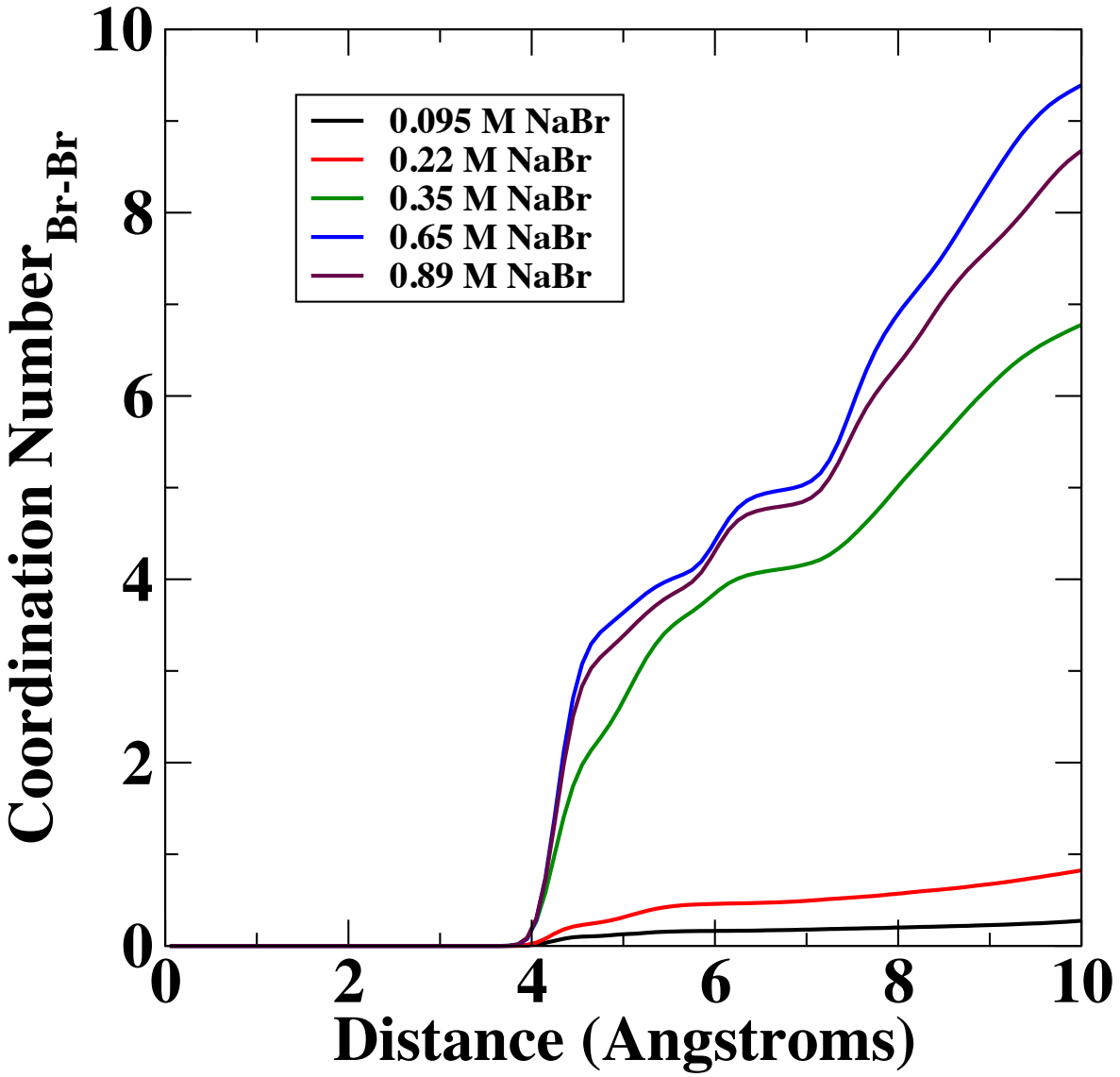

Figure 7.11: Coordination number of Br with respect to Br in MeCN solution containing NaBr.

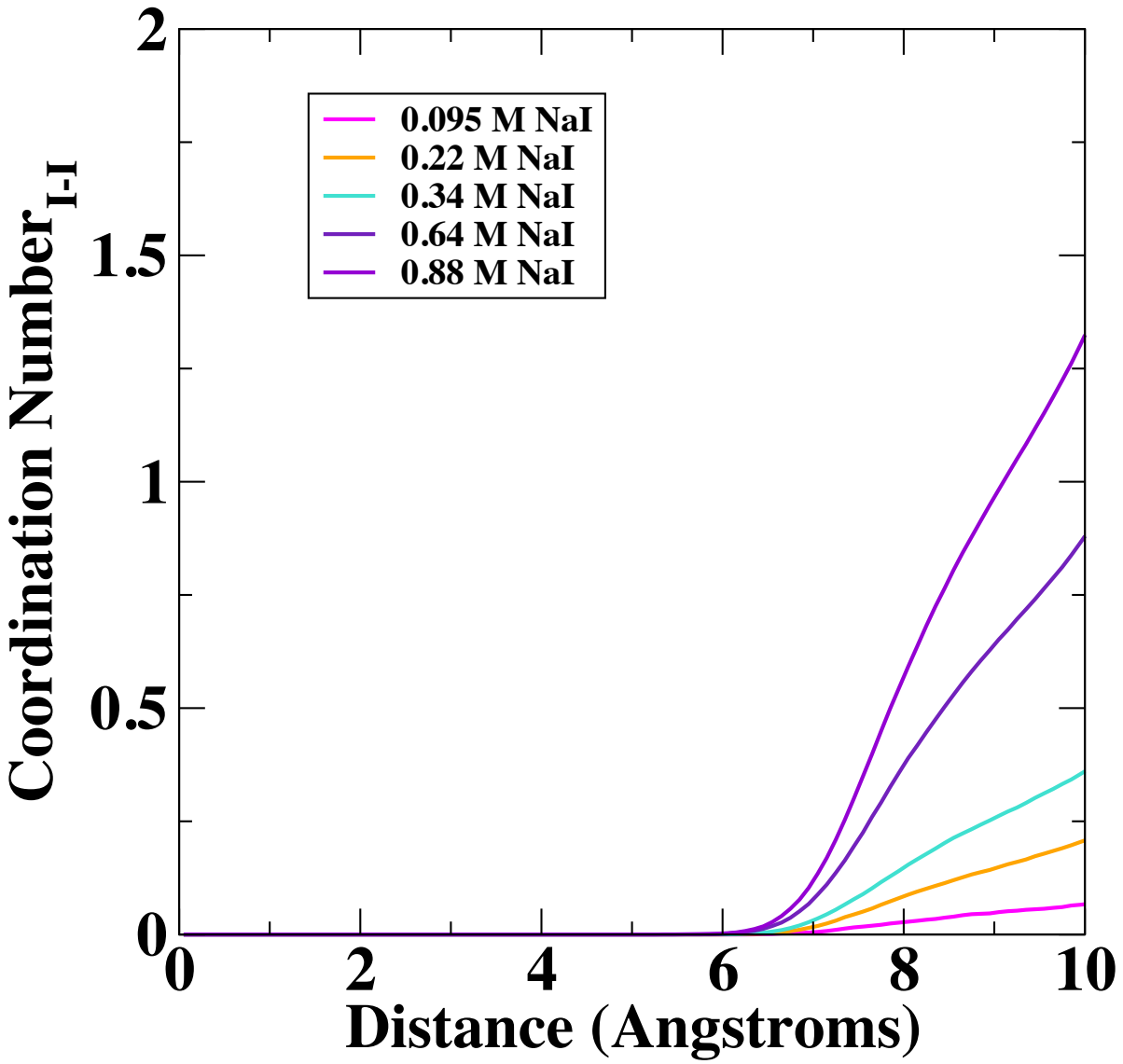

Figure 7.12: Coordination number of I with respect to I in MeCN solution containing NaI.

7.6 Conclusion

In experimental settings, ions are added to organic solvents in a supercapacitor. This has been found to affect the dielectric constant of water[14,225,252–254] and other systems.[18,252,255] Continuum modeling of EDLCs must take this change into account when using the dielectric constant of the solvent system as a parameter in calculating capacitance. There has been previous work in the literature on calculating the dielectric constant of aqueous solutions,[234,235] but we did not find research employing MD to examine the dielectric constant of organic salt solutions in the literature. For this reason, we used molecular dynamics to examine the dielectric constant of salt solutions of MeCN, PC and EC/DMC.

First, the dielectric decrement of MeCN is examined to compare our results with experiment. The salts NaI and LiBr were chosen in order to determine that calculation of the dielectric decrement using MD are in reasonable agreement with experiment. The force fields chosen for this topic demonstrated reasonable agreement with respect to experiment for NaI and LiBr solutions. With our force fields validated, we were able to examine additional salt solutions, specifically solutions containing LiI and NaBr. The dielectric constant decreased the most with respect to concentration for LiI solutions, followed by NaI, LiBr and NaBr solutions. The latter system showed a significantly weaker dielectric decrement than the other three salt solutions. To determine if the solvation number is correlated with the dielectric decrement, we plotted the coordination numbers of the salt solutions. We found that the coordination numbers for NaI and LiI change little with respect to concentration, while the coordination number sharply decreases for NaBr, with LiBr causing intermediate effect, which matches our data considerably. Our data for dielectric constants also agree with our plots of the number of ion types with respect to inter-ionic distance. We observe that NaBr precipitates in solution, which not only corroborates our hypothesis on the cause of dielectric decrement (ions using electric fields to prevent solvent molecules to contribute fully to the dielectric constant), but also agrees with experimental observation that NaBr is relatively insoluble in MeCN. We attribute the quantitative differences with respect to experiment to our use of non-polarizable charges in our simulations. Spångberg et al.[256] found that a pairwise force field

(P2) for MeCN overestimated the solvation shell for cations with respect to the shell found using a polarizable force field. Because our hypothesis is that the dielectric constant decreases relative to the number of solvent molecules attracted to the ions, an overestimated solvation shell would cause the dielectric constant to decrease at a greater rate with respect to experiment, which would explain the larger dielectric decrement of our data.

Because our force fields for the ions in MeCN produced adequate agreement with experiment, we used the same force fields to calculate dielectric constants for NaI, LiBr and NaBr solutions of PC and NaI solutions of EC/DMC mixtures. The dielectric decrement was roughly equivalent for the three PC solutions. For EC/DMC mixtures, there does not appear to be any literature examining possible dielectric decrement for EC/DMC mixtures, which would make our work the first to report this effect in these mixtures. The effect of salt concentration showed negative to zero correlation with respect to dielectric constant for the two EC/DMC systems composes the largest portion of DMC. In the future, computer simulations could be performed for additional PC solutions to compare to existing experimental data.

Our data adds to the existing knowledge of dielectric decrement in the following ways. As stated earlier, continuum modelers can use our results for the dielectric constant of salt solutions for their calculations of capacitance to ensure better agreement with experimental conditions. Also, our investigations into the atomistic structure of MeCN with respect to the ions verified previous theoretical thought on one of the principal causes of dielectric decrement.

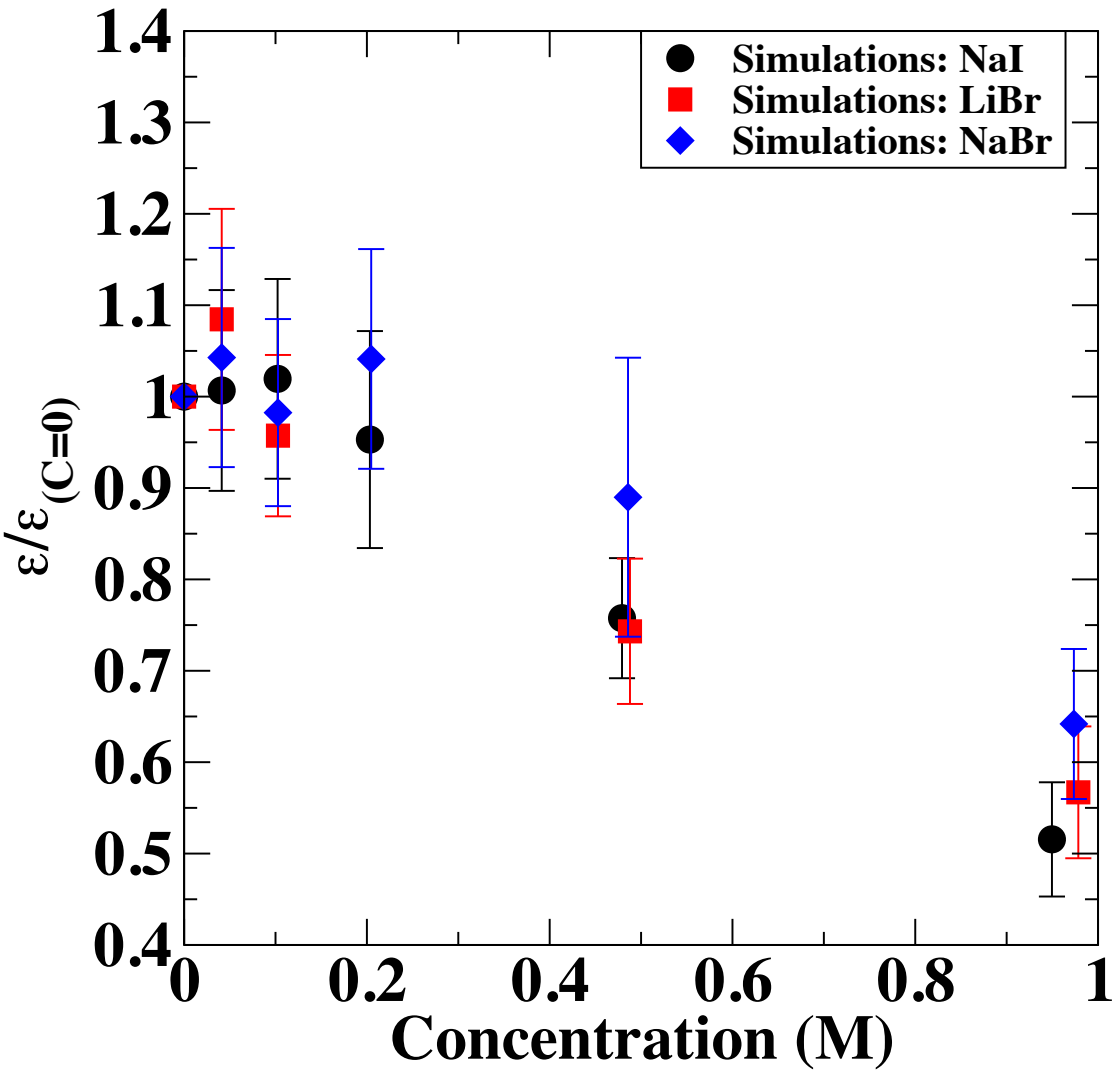

Figure 7.13: Dielectric constant fraction for salt solution of PC as a function of salt concentration.

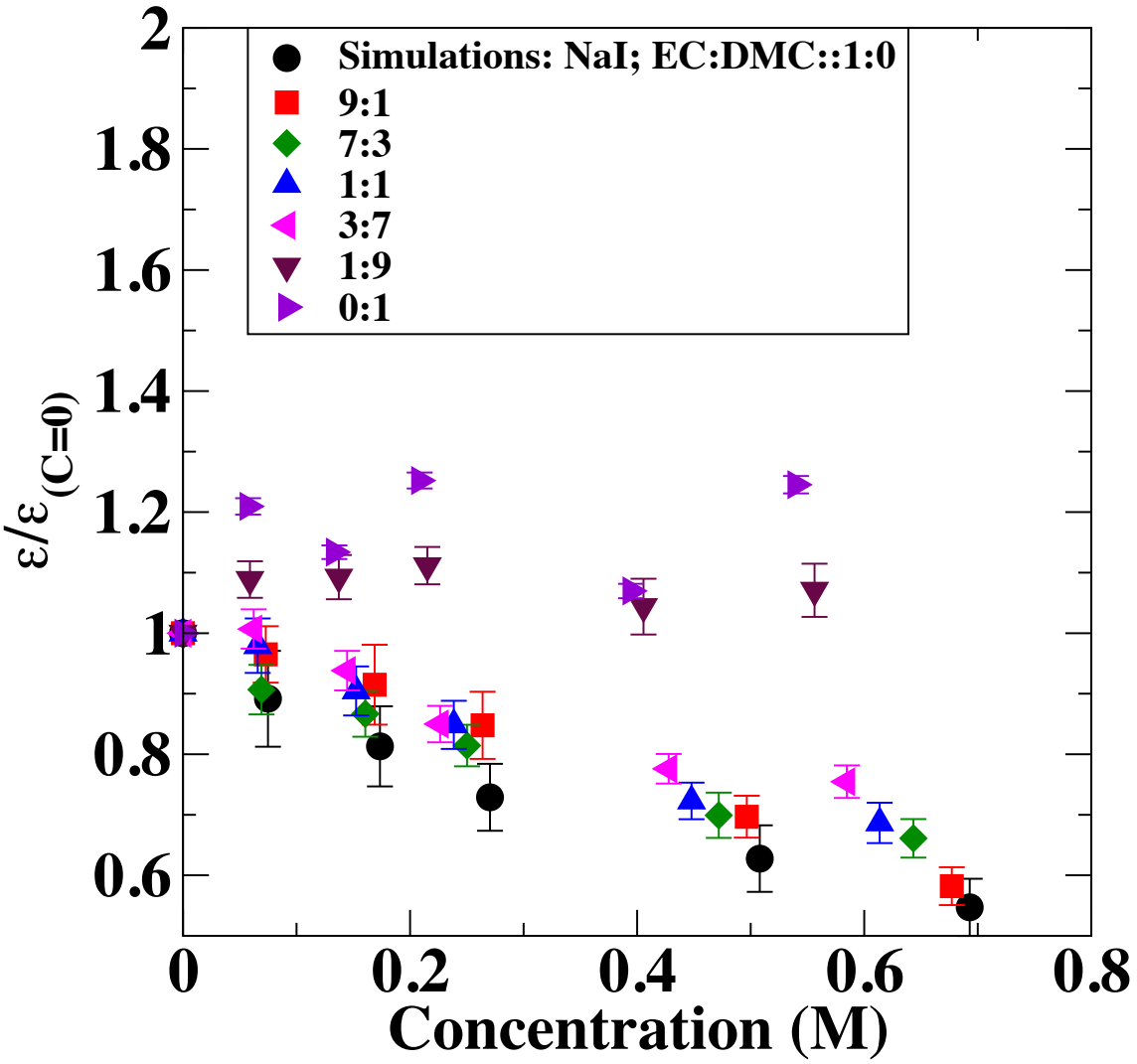

Figure 7.14: Dielectric constant fraction for salt solution of several molar compositions of EC/DMC mixtures as a function of NaI concentration.

Chapter 8

Conclusion

We have addressed two significant issues with regards to our current energy crisis with the aid of molecular simulations: means to curb output of greenhouse gases and energy storage for use for renewable resources.

Grand Canonical Monte Carlo simulations were employed to determine the adsorption of several gases in Zeolitic Imidazolate Frameworks. For CO_2 and CH_4, we compare the data produced with that of experiment and find fairly good agreement generally. With this confidence, we explored the systems in additional ways. Specifically, we explored the contribution electrostatics plays in adsorption. We also tried to determine where the gas molecules preferred to adsorb in the ZIF. To accomplish this, we created density maps for these gases and proceeded to connect this data with our adsorption information in order to plausibly explain our results. One of the key results we found is that adsorption tends to favor adsorption in smaller pores as low pressure while the opposite occurs at high pressure, though, we have noted there are exceptions to this, some of which may depend on specific aspects of the geometry of the systems. We also provided some results on adsorption of H_2S, and also examined the contribution of charges.

In the second part of our work, we examined the dielectric constants of solvent systems. This work consisted of examining the effect of two different stimuli: applied electric field and salt concentration. For both, we observe that the dielectric constant for the most part decreases with

the magnitude of these two stimuli. We note that 'electrofreezing' occurs at high field for MeCN systems, EC systems, and EC/DMC systems with a majority of EC using snapshots to back up our claims. When these data points were omitted from the fits, we found very good agreement. For the effect of salt concentration, we looked at the MeCN solvent using four ion systems: sodium iodide (NaI), sodium bromide (NaBr), lithium iodide (LiI) and lithium bromide (LiBr). We compared data from the first two systems with experiment and found acceptable agreement. In order to understand the cause of the decrement, we determined coordination numbers for all simulations, which show that NaBr solutions have considerably lower coordination numbers than for the other two salts, especially at larger concentration. We also examined a snapshot from NaI and NaBr solutions at several concentrations and found considerable ion aggregation for NaBr solutions.

Various avenues are available to continue our work with respect to ZIF adsorption and examination of the dielectric constants of electrolyte solvents. Investigations regarding the adsorption of H_2S for ZIFs 7/11 and 93/94 can be started using the ZIF force fields employed for CO_2 and CH_4 adsorption. To correct for the effect of charge polarization on the dielectric decrement, models using fluctuating charges can be employed. This will be especially useful for examining the dielectric decrement. Future simulations can be performed to examine the electrofreezing we observed to determine if it is an artifact of the simulations or a possible phenomenon that could be observed in experiment.

In addition to future work involving atomistic simulations, our results can also assist researchers outside this field The results we found for H_2S adsorption can be used by experimentalists as a gauge to measure the adsorption of promising ZIFs. With regards to energy storage systems, the fitted values for the dependence of dielectric constant with respect to electric field can be used by continuum modelers to more accurately examine the capacitance of EDLCs.

Appendix A

Derivation of Booth Model

Before using the Booth Model, one should understand how it is derived and the assumptions made while performing this derivation.

We will start our overall derivation by examining Onsager's work. He separates the potential of a dipole into separate components. The first involves a point dipole in a spherical cavity, while the second involves an empty cavity undergoing an electric field. This cavity is created in order to allow a continuum in which the dielectric constant is uniform. Thus, we will use a mean field approximation. We will first examine the former case. In the cavity there is a dielectric constant of n^2 while outside the dielectric constant is ε^2 The potential must obey Laplace's equation

$$\nabla^2 \psi = 0 \tag{A.1}$$

and the following boundary conditions:

$$\psi(r,\theta) - \frac{\mu \cos(\theta)}{n^2 r^2} \text{ is continuous } < \infty \tag{A.2}$$

and

$$n^2 \left(\frac{\partial \psi}{\partial r}\right)_{r=a-0} = \varepsilon \left(\frac{\partial \psi}{\partial r}\right)_{r=a+0} \tag{A.3}$$

We can use the knowledge that the solution of Laplace's Equation in spherical coordinates and azimuthal symmetry has the general form of

$$\sum_{l=0}^{\infty}\left[A_l r^l + B_l r^{-(l+1)}\right] P_l(\cos\phi) \tag{A.4}$$

with $P_l(x)$ is the Legendre polynomial. Thus we will determine the potential that satisfy the above condition. Note that we can conclude the following from Equation A.2

$$\psi(r,\theta) = G(r,\theta) + \frac{\mu\cos(\theta)}{n^2 r^2} \tag{A.5}$$

with

$$G(r,\theta) = \begin{cases} D(r,\theta) & r < R \\ E(r,\theta) & r \geq R \end{cases} \tag{A.6}$$

$D(r,\theta)$ and $E(r,\theta)$ both being continuous functions. For our purposes, $E(r,\theta)$ is the total potential of the space outside the sphere, while $D(r,\theta) + \frac{m\cos(\theta)}{n^2 r^2}$ is the potential inside the sphere.

Outside the cavity, the dipole is still able to exert the following potential,

$$E(r,\theta) = \frac{\mu_e}{\varepsilon r^2}\cos\theta \tag{A.7}$$

in which is the external dipole moment. The dipole also produces the following potential stemming from it's field.

$$D(r,\theta) = -Rr\cos\theta \tag{A.8}$$

We will now solve for both constants. At $r = a$ (cavity radius), we can determine the following relation,

$$\frac{\mu\cos\theta}{n^2 a^2} - Ra\cos\theta = \frac{\mu_e\cos\theta}{\varepsilon a^2} \tag{A.9}$$

which leads to

$$\mu_e = a^2\varepsilon\left(\frac{\mu}{n^2 a^2} - Ra\right) \tag{A.10}$$

Using Equation A.3 we know

$$-\frac{2n^2\mu\cos\theta}{n^2 a^3} - Rn^2\cos\theta = \frac{-2\varepsilon\mu_e\cos\theta}{a^3} \tag{A.11}$$

Substituting Equation A.10 into A.11 gives

$$-\frac{2\mu n^2\cos\theta}{n^2a^3}-Rn^2\cos\theta=\frac{-2\varepsilon^2a^2\left(\frac{\mu}{n^2a^2}-Ra\right)\cos\theta}{a^3\varepsilon}=\frac{-2\varepsilon\left(\frac{\mu}{n^2a^2}-Ra\theta\right)\cos\theta}{a} \tag{A.12}$$

We can factor out $\cos\theta$ and find

$$-\frac{2\mu}{a^3}-Rn^2=-2\varepsilon\left(\frac{\mu}{n^2a^3}-R\right) \tag{A.13}$$

thus

$$R\left(2\varepsilon+n^2\right)=\frac{2\mu\left(\varepsilon-n^2\right)}{n^2a^3} \tag{A.14}$$

which gives us

$$R=\frac{2\mu\left(\varepsilon-n^2\right)}{\left(2\varepsilon+n^2\right)n^2a^3} \tag{A.15}$$

R denotes the magnitude of the electric field created by the dipole in the cavity. Substituting Equation A.15 into A.10 for $r=a$ gives

$$\mu_e=\varepsilon a^2\left(\frac{\mu}{n^2a^2}-\left(\frac{2\mu\left(\varepsilon-n^2\right)}{\left(2\varepsilon+n^2\right)n^2a^3}\right)a\right)=\frac{\varepsilon\mu}{n^2}-\frac{2\varepsilon\mu\left(\varepsilon-n^2\right)}{n^2\left(2\varepsilon+n^2\right)} \tag{A.16}$$

Using algebra we find

$$\mu_e=\frac{\varepsilon\mu\left(2\varepsilon+n^2\right)}{n^2\left(2\varepsilon+n^2\right)}-\frac{2\varepsilon\mu\left(\varepsilon-n^2\right)}{n^2\left(2\varepsilon+n^2\right)}=\frac{2\varepsilon^2\mu+\varepsilon\mu n^2-2\varepsilon^2\mu+2\varepsilon n^2\mu}{n^2\left(2\varepsilon+n^2\right)} \tag{A.17}$$

Thus

$$\mu_e=\frac{3\varepsilon}{\left(2\varepsilon+n^2\right)}\mu \tag{A.18}$$

This term refers to the force that the dipole will have on a distant charge in a dielectric, through a medium of dielectric constant n^2. Now we will focus on the case involving a cavity in an electric field. The boundary conditions for the derivatives of the potentials are the same, but note that

$$\psi(r,\theta)+Er\cos\theta \text{ is continuous} <\infty \tag{A.19}$$

With this information, we can write the potential as

$$\psi(r,\theta)=W(r,\theta)-Er\cos\theta \tag{A.20}$$

in which

$$W(r,\theta) = \begin{cases} T(r,\theta) & r < R \\ S(r,\theta) & r \geq R \end{cases} \tag{A.21}$$

$S(r,\theta)$ and $T(r,\theta)$ both being continuous functions. For our purposes, $S(r,\theta) - Er\cos\theta$ is the total potential of the space outside the sphere, while $T(r,\theta)$ is the potential in the sphere. Because $S(r,\theta)$ should decrease with respect to distance from the cavity surface so that the potential that remains is $Er\cos\theta$, we can assume

$$S(r,\theta) = -\frac{M\cos\theta}{r^2} \tag{A.22}$$

in which M is a constant, because it both fits the physical criterion and satisfies the general solution of the Laplacian. Inside the sphere, we will assume

$$T(r,\theta) = -Gr\cos\theta \tag{A.23}$$

caused by the field in the cavity, in which G is a constant. Thus, using Equation (3)

$$-Ea\cos\theta - \frac{M}{a^2}\cos\theta = -Ga\cos\theta \tag{A.24}$$

which leads us to

$$G = E + \frac{M}{a^3} \tag{A.25}$$

With the aid of Equation A.3, we know

$$\varepsilon\left(-E\cos\theta + 2\frac{M}{a^3}\cos\theta\right) = n^2\left(-G\cos\theta\right) \tag{A.26}$$

Substituting Equation (25) into (26) gives

$$\varepsilon\left(-E\cos\theta + 2\frac{M}{a^3}\cos\theta\right) = -n^2\left(E + \frac{M}{a^3}\right)\cos\theta \tag{A.27}$$

which gives

$$\frac{M}{a^3}\left(2\varepsilon + n^2\right) = E\left(\varepsilon - n^2\right) \tag{A.28}$$

Thus

$$M = \frac{E\left(\varepsilon - n^2\right)}{2\varepsilon + n^2}a^3 \tag{A.29}$$

Thus, M is the field in the cavity. Placing Equation (29) into (25) gives

$$G = E + \frac{E\left(\varepsilon - n^2\right)}{2\varepsilon + n^2} = \frac{3\varepsilon E}{2\varepsilon + n^2} \tag{A.30}$$

Now that we have determined the magnitude of the reaction field and cavity field, R and G respectively, we can construct the total field, $\mathbf{F}$ through including the directions for R and G, giving.

$$\mathbf{F} = \mathbf{G} + \mathbf{R} = \frac{3\varepsilon \mathbf{E}}{2\varepsilon + n^2} + \frac{2\mu\left(\varepsilon - n^2\right)}{\left(2\varepsilon + n^2\right) n^2 a^3} \tag{A.31}$$

Using the assumption of $\varepsilon \gg n^2$for Equation (30),

$$\mathbf{F} = \frac{3}{2}\mathbf{E} + \frac{\mu}{n^2 a^3} \tag{A.32}$$

Now that we know that total field, we can determine the electric moment of the system through the following equation

$$M_e = 5N\mu \langle \cos\theta \rangle \tag{A.33}$$

in which θ is the angle between $\mathbf{E}$ and μ. At this point we note the Booth Model was originally used for water, thus the 'dipole' for water is actually that of itself and its four neighbors. Thus, we will multiply this value by five.

We will now proceed to determine $\langle \cos\theta \rangle$

$$\langle \cos\theta \rangle = \frac{\int_0^\pi \cos\theta \sin\theta \exp\left(5\mu \cdot \mathbf{F}/kT\right) d\theta}{\int_0^\pi \sin\theta \exp\left(5\mu \cdot \mathbf{F}/kT\right) d\theta} \tag{A.34}$$

This equation will allow us to determine the extent to which the direction of the electric field attenuates the moment.

Writing the explicit form of $\mathbf{F}$ gives

$$\langle \cos\theta \rangle = \frac{\int_0^\pi \cos\theta \sin\theta \exp\left(5\mu \cdot \left(\frac{3}{2}\mathbf{E} + \frac{\mu}{n^2 a^3}\right)/kT\right) d\theta}{\int_0^\pi \sin\theta \exp\left(5\mu \cdot \left(\frac{3}{2}\mathbf{E} + \frac{\mu}{n^2 a^3}\right)/kT\right) d\theta} \tag{A.35}$$

Using the property of dot product gives

$$\langle \cos\theta \rangle = \frac{\int_0^{\pi} \cos\theta \sin\theta \exp\left(5\left(\frac{3}{2kT} E\mu \cos\theta_2 + \frac{m^2}{n^2 a^3 kT}\cos 0\right)\right) d\theta}{\int_0^{\pi} \sin\theta \exp\left(5\left(\frac{3}{2kT} E\mu \cos\theta + \frac{m^2}{n^2 a^3 kT}\cos 0\right)\right) d\theta} \tag{A.36}$$

The equation can be factored as shown

$$\langle \cos\theta \rangle = \frac{\exp\left(\frac{m^2}{kTn^2a^3}\right) \int_0^{\pi} \cos\theta \sin\theta \exp\left(\frac{15}{2kT} E\mu \cos\theta\right) d\theta}{\exp\left(\frac{m^2}{kTn^2a^3}\right) \int_0^{\pi} \sin\theta \exp\left(\frac{15}{2kT} E\mu \cos\theta\right) d\theta} \tag{A.37}$$

which simplifies to

$$\langle \cos\theta \rangle = \frac{\int_0^{\pi} \cos\theta \sin\theta \exp\left(\frac{15}{2kT} E\mu \cos\theta\right) d\theta}{\int_0^{\pi} \sin\theta \exp\left(\frac{15}{2kT} E\mu \cos\theta\right) d\theta} \tag{A.38}$$

The solution for the above integral is

$$\langle \cos\theta \rangle = \coth\left(\frac{15E\mu}{2kT}\right) - \frac{1}{\frac{15E\mu}{2kT}} = L\left(\frac{15E\mu}{2kT}\right) \tag{A.39}$$

in which $L(x)$ is the Langevin function. Thus, we now know the following

$$\bar{M}_E = 5N\mu L\left(\frac{15E\mu}{2kT}\right) \tag{A.40}$$

Given that

$$P = \frac{\bar{M}_E}{V} \tag{A.41}$$

one obtains the following

$$P = \frac{5N\mu L\left(\frac{15E\mu}{2kT}\right)}{V} \tag{A.42}$$

in which ν represents molar volume and leads to the molecular volume as shown

$$y = N/V \tag{A.43}$$

Substituting Equation A.43 into A.42 gives

$$P = 5y\mu L\left(\frac{15\mu E}{2kT}\right) \tag{A.44}$$

Substituting this into the following equation from Booth's paper

$$\varepsilon - n^2 = 4\pi P/E \tag{A.45}$$

and using Equation A.18, (in our circumstance, the dielectric in that equation will be a vacuum) gives

$$\varepsilon(E) = n^2 + \frac{4\pi\left(n^2+2\right)5}{3E}\left(\mu_e y L(3\beta E)\right) \tag{A.46}$$

in which

$$\beta = \frac{5\left(n^2+2\right)\mu_e E}{2kT} \tag{A.47}$$

Cancelling out terms gives

$$\varepsilon(E) = n^2 + \frac{20\pi\left(n^2+2\right)}{3E} y\mu_e L(\beta E) \tag{A.48}$$

Now one converts the previous formula into a format similar to Pilon's, as shown below.

$$\varepsilon(E) - n^2 = \frac{4\pi y\left(n^2+2\right)}{3E}\mu_e L(\beta E) \tag{A.49}$$

One divides the above by $\varepsilon_0 - n^2$, which is equivalent to $lim_{E\to 0}\varepsilon(E) - n^2$, which gives

$$\frac{\varepsilon(E)-n^2}{\varepsilon(0)-n^2} = \frac{\frac{20y\pi\left(n^2+2\right)5}{3E}\left(x\mu_e L(\beta E)\right)}{\frac{20y\pi\left(n^2+2\right)5}{3E}\left(\left(x\mu_e L(\beta E)\right)\right)_{E\to 0}} \tag{A.50}$$

Now one writes the denominator with explicit Langevins as shown

$$\varepsilon(0) - n^2 = \left(\mu_e\left(\coth(\beta E) - \frac{1}{\beta E}\right)\right) \tag{A.51}$$

Before proceeding, it is important to note the following Taylor series

$$\coth(x) = \frac{1}{x} + \frac{x}{3} - \frac{x^3}{45} + ... \tag{A.52}$$

Performing a Taylor Series for the denominator gives

$$\varepsilon(0) - n^2 = \mu_e\left(\frac{1}{\beta E} + \frac{\beta E}{3} - \frac{1}{\beta E}\right) \tag{A.53}$$

And with this one obtain

$$\frac{\varepsilon(E)-n^2}{\varepsilon(0)-n^2} = \frac{\left(\mu_e L(\beta E)\right)}{\left(\mu_e\left(\frac{\beta E}{3}\right)\right)} \tag{A.54}$$

With rearrangement, one may finally obtain the following

$$\varepsilon(E) = n^2 + \left(\varepsilon(0) - n^2\right)\left(\frac{3}{\beta E} L(\beta E)\right) \tag{A.55}$$

Appendix B

Presentations and Manuscripts

Poster Presentations

-“Molecular Modeling of Metal Oxide Pseudocapacitors”, Kansas Physical Chemistry Symposium, Kansas State University, October 13 2012.

-“Molecular Modeling of Dielectric Constant of EC/DMC Mixtures”. CEBC Fall Industry Advisory Meeting, October 6 2014.

-“The Dielectric Constant for ethylene carbonate/dimethyl carbonate a a Function of Electric Field”, CEBC Spring Industry and Science Advisory Board Meeting, April 18 2015.

-“The Dielectric Constant for ethylene carbonate/dimethyl carbonate a a Function of Electric Field”, CEBC Fall Advisory Meeting, October 5 2015.

-“The Dielectric Constant for Pure and Mixed Solvents as a Function of Electric Field”, Midwest Regional Meeting of the American Chemical Society”, October 27 2015.

-“The Dielectric Constant for Pure and Mixed Solvents as a Function of Electric Field”, Wakarusa Valley ACS Student Research Symposium, November 7 2015.

-“The Dielectric Constant for ethylene carbonate/dimethyl carbonate as a Function of Electric Field”, American Chemical Society Conference, March 24 2015.

-“The Dielectric Constant for Acetonitrile as a Function of Salt Concentration”, American

Chemical Society Conference, March 15 2016

Oral Presentations

-"Zeolitic Imidazolate Frameworks: Analyzing the adsorption and selectivity for CO_2", Physical Chemistry seminar, University of Kansas, May 2011.

-"Gas Adsorption in Zeolitic Imidazolate Frameworks", Physical Chemistry seminar, University of Kansas, February 2012.

-Absorption of Toxic Gases in Zeolite Imidazolate Frameworks: A Computational Study", Kansas Physical Chemistry Symposium, University of Kansas, November 19 2011.

-"Examining Metal-Oxide Pseudocapacitors", DyMERS seminar, University of Kansas, December 5 2012.

-"Molecular Modeling of Solutions for Use in Supercapacitors", Kansas Physical Chemistry Symposium, University of Kansas, November 9 2013.

-"Molecular Modeling of Organic Electrolyte Solutions", DyMERS seminar, University of Kansas, April 9 2014.

-"Molecular Modeling of Organic Electrolyte Solutions", Augustana College, May 2014.

Publications

-"A Combined experimental-computational study on the effect of topology in zeolitic imidazolate frameworks", W. Morris, N. He, K. Ray, P. Klonowski, H. Furkukawa, I. Daniels, Y.A. Houndonougbo, M.D. Asta, B.B. Laird and O.M. Yaghi, J. Phys. Chem. C 116, 24084-24090 (2012).

-"Dielectric Properties of Organic Solvents in an Electrical Field", I. N. Daniels, Z. Wang and B. B. Laird, (XXXX), in preparation

-"Dielectric Properties of Organic Electrolyte Solutions", I. N. Daniels and B. B. Laird, (XXXX), in preparation

References

[1] A. Phan, C. J. Doonan, F. J. Uribe-Romo, C. B. Knobler, M. O'keeffe, and O. M. Yaghi, Acc. Chem. Res **43**, 58 (2010).

[2] Z. Wang, Y. Yang, D. L. Olmsted, M. Asta, and B. B. Laird, J. Chem. Phys. **141**, 1 (2014).

[3] V. A. Kuzkin, Z. Angew. Math. Mech. **95**, 1290 (2015).

[4] K. S. Park, Z. Ni, A. P. Côté, J. Y. Choi, R. Huang, F. J. Uribe-Romo, H. K. Chae, M. O'Keeffe, and O. M. Yaghi, P. Natl Acad. Sci. USA **103**, 10186 (2006).

[5] I. S. . A. U.S. Department of Energy, Energy Information Administration, *Figure 11.1 carbon dioxide emissions from energy consumption*, URL `http://www.eia.gov/totalenergy/data/annual/pdf/sec11_2.pdf`.

[6] P. Zhao, G. I. Lampronti, G. O. Lloyd, E. Suard, and S. A. Redfern, J. Mater. Chem. A **2**, 620 (2014).

[7] W. Morris, B. Leung, H. Furukawa, O. K. Yaghi, N. He, H. Hayashi, Y. Houndonougbo, M. Asta, B. B. Laird, and O. M. Yaghi, J. Am. Chem. Soc. **132**, 11006 (2010).

[8] M. O'Keeffe, M. A. Peskov, S. J. Ramsden, and O. M. Yaghi, Acc. Chem. Res **41**, 1782 (2008).

[9] O. S. Smart, J. M. Goodfellow, and B. Wallace, Biophys. J. **65**, 2455 (1993).

[10] W. Morris, N. He, K. G. Ray, P. Klonowski, H. Furukawa, I. N. Daniels, Y. A. Houndonougbo, M. Asta, O. M. Yaghi, and B. B. Laird, J. Phys. Chem. C **116**, 24084 (2012).

[11] W. Morris, *Experimental data for zif adsorption*, Private communcation.

[12] M. Winter and R. J. Brodd, Chem. Rev. **104**, 4245 (2004).

[13] J. Varghese, H. Wang, and L. Pilon, J. Electrochem. Soc. **158**, A1106 (2011).

[14] J. B. Hasted, D. M. Ritson, and C. H. Collie, J. Chem. Phys. **16**, 1 (1948).

[15] R. Naejus, D. Lemordant, R. Coudert, and P. Willman, J. Chem. Thermodyn. **29**, 1503 (1997).

[16] J. Barthel, M. Kleebauer, and R. Buchner, J. Solution Chem. **24**, 1 (1995).

[17] A. L. Spek, J. Appl. Crystallogr. **36**, 7 (2003).

[18] J. Barthel, M. Kleebauer, and R. Buchner, J. Sol. Chem. **24**, 1 (1995).

[19] N. Metropolis, A. W. Rosenbluth, M. N. Rosenbluth, A. H. Teller, and E. Teller, J. Chem. Phys. **21**, 1087 (1953).

[20] B. J. Alder and T. E. Wainwright, J. Chem. Phys. **27**, 1208 (1957).

[21] D. Frenkel and B. Smit, *Understanding molecular simulation: from algorithms to applications*, vol. 1 (Academic press, 2001).

[22] M. P. Allen and D. J. Tildesley, *Computer Simulation of liquids* (Oxford university press, 1989).

[23] B. Widom, J. Chem. Phys. **39**, 2808 (1963).

[24] L. Verlet, Phys. Rev. **159**, 98 (1967).

[25] W. C. Swope, H. C. Andersen, P. H. Berens, and K. R. Wilson, J. Chem. Phys. **76**, 637 (1982).

[26] S. Nosé, Mol. Phys. **52**, 255 (1984).

[27] W. G. Hoover, Phys. Rev. A **31**, 1695 (1985).

[28] G. J. Martyna, M. L. Klein, and M. Tuckerman, J. Chem. Phys. **97**, 2635 (1992).

[29] G. J. Martyna, D. J. Tobias, and M. L. Klein, J. Chem. Phys. **101**, 4177 (1994).

[30] H. C. Andersen, J. Chem. Phys. **72**, 2384 (1980).

[31] R. W. Hockney and J. W. Eastwood, *Computer simulations using particles* (CRC Press, 1988).

[32] M. Jian, B. Liu, G. Zhang, R. Liu, and X. Zhang, Colloids Surf., A **465**, 67 (2015).

[33] C.-s. Wu, Z.-h. Xiong, C. Li, and J.-m. Zhang, R. Soc. Chem. Adv. **5**, 82127 (2015).

[34] Y. Zhao, Y. Pan, W. Liu, and L. Zhang, Chem. Lett. **44**, 758 (2015).

[35] Y. Gao, J. Wu, W. Zhang, Y. Tan, J. Zhao, and B. Tang, Mater. Lett. **128**, 208 (2014).

[36] S. D. Kenarsari, D. Yang, G. Jiang, S. Zhang, J. Wang, A. G. Russell, Q. Wei, and M. Fan, R. Soc. Chem. Adv. **3**, 22739 (2013).

[37] N. Du, H. B. Park, M. M. Dal-Cin, and M. D. Guiver, Energ. Environ. Sci. **5**, 7306 (2012).

[38] M. E. Boot-Handford, J. C. Abanades, E. J. Anthony, M. J. Blunt, S. Brandani, N. Mac Dowell, J. R. Fernández, M.-C. Ferrari, R. Gross, J. P. Hallett, et al., Energ. Environ. Sci. **7**, 130 (2014).

[39] D. M. D'Alessandro, B. Smit, and J. R. Long, Angew. Chem. Int. Ed. **49**, 6058 (2010).

[40] P. Markewitz, W. Kuckshinrichs, W. Leitner, J. Linssen, P. Zapp, R. Bongartz, A. Schreiber, and T. E. Müller, Energ. Environ. Sci. **5**, 7281 (2012).

[41] X. Huang, J. Zhang, and X. Chen, Chinese Sci. Bull. **48**, 1531 (2003).

[42] Y.-Q. Tian, Z.-X. Chen, L.-H. Weng, H.-B. Guo, S. Gao, and D. Y. Zhao, Inorg. Chem. **43**, 4631 (2004).

[43] X.-C. Huang, Y.-Y. Lin, J.-P. Zhang, and X.-M. Chen, Angew. Chem.-Ger. Edit. **118**, 1587 (2006).

[44] T. Panda, K. M. Gupta, J. Jiang, and R. Banerjee, CrystEngComm **16**, 4677 (2014).

[45] L. Mu, B. Liu, H. Liu, Y. Yang, C. Sun, and G. Chen, J. Mater. Chem. **22**, 12246 (2012).

[46] P. Cheng and Y. H. Hu, J. Phys. Chem. C **118**, 21866 (2014).

[47] A. Kasik, X. Dong, and Y. Lin, Micropor. Mesopor. Mat. **204**, 99 (2015).

[48] X. Liu, Y. Li, Y. Ban, Y. Peng, H. Jin, H. Bux, L. Xu, J. Caro, and W. Yang, Chem. Commun. **49**, 9140 (2013).

[49] R. Banerjee, A. Phan, B. Wang, C. Knobler, H. Furukawa, M. O'Keeffe, and O. M. Yaghi, Science **319**, 939 (2008).

[50] R. Banerjee, H. Furukawa, D. Britt, C. Knobler, M. O'Keeffe, and O. M. Yaghi, J. Am. Chem. Soc. **131**, 3875 (2009).

[51] H. Hayashi, A. P. Cote, H. Furukawa, M. O'Keeffe, and O. M. Yaghi, Nat. Mater. **6**, 501 (2007).

[52] B. Wang, A. P. Côté, H. Furukawa, M. O'Keeffe, and O. M. Yaghi, Nature **453**, 207 (2008).

[53] Q. Shi, X. Kang, F.-N. Shi, and J. Dong, Chem. Commun. **51**, 1131 (2015).

[54] J. A. Thompson, C. R. Blad, N. A. Brunelli, M. E. Lydon, R. P. Lively, C. W. Jones, and S. Nair, J. Chem. Mater. **24**, 1930 (2012).

[55] J. A. Thompson, J. T. Vaughn, N. A. Brunelli, W. J. Koros, C. W. Jones, and S. Nair, Micropor. Mesopor. Mat. **192**, 43 (2014).

[56] L. Huang, M. Xue, Q. Song, S. Chen, Y. Pan, and S. Qiu, Inorg. Chem. Commun. **46**, 9 (2014).

[57] J. Kahr, J. P. Mowat, A. M. Slawin, R. E. Morris, D. Fairen-Jimenez, and P. A. Wright, Chem. Commun. **48**, 6690 (2012).

[58] M. Gustafsson and X. Zou, J. Porous Mater. **20**, 55 (2013).

[59] H. Fei, J. F. Cahill, K. A. Prather, and S. M. Cohen, Inorg. Chem. **52**, 4011 (2013).

[60] Y. Ban, Y. Li, Y. Peng, H. Jin, W. Jiao, X. Liu, and W. Yang, Chem. Eur. J. **20**, 11402 (2014).

[61] H. Wu, W. Zhou, and T. Yildirim, J. Am. Chem. Soc. **129**, 5314 (2007).

[62] C. Chmelik, J. van Baten, and R. Krishna, J. Membr. Sci. **397**, 87 (2012).

[63] H. Bux, F. Liang, Y. Li, J. Cravillon, M. Wiebcke, and J. Caro, J. Am. Chem. Soc. **131**, 16000 (2009).

[64] F. Cacho-Bailo, B. Seoane, C. Téllez, and J. Coronas, J. Membr. Sci. **464**, 119 (2014).

[65] X. Dong and Y. Lin, Chem. Commun. **49**, 1196 (2013).

[66] Y. Pan, B. Wang, and Z. Lai, J. Membr. Sci. **421**, 292 (2012).

[67] A. Huang, Y. Chen, N. Wang, Z. Hu, J. Jiang, and J. Caro, Chem. Commun. **48**, 10981 (2012).

[68] Y.-C. Liu, G. Zeng, Y. Pan, and Z. Lai, J. Membr. Sci. **379**, 46 (2011).

[69] L. Li, J. Yao, R. Chen, L. He, K. Wang, and H. Wang, Micropor. Mesopor. Mat. **168**, 15 (2013).

[70] H. Bux, C. Chmelik, R. Krishna, and J. Caro, J. Membr. Sci. **369**, 284 (2011).

[71] K. LunáYeung et al., J. Mater. Chem. A **1**, 10635 (2013).

[72] A. Huang and J. Caro, Angew. Chem. Int. Ed. **50**, 4979 (2011).

[73] A. Huang, H. Bux, F. Steinbach, and J. Caro, Angew. Chem. **122**, 5078 (2010).

[74] K. Tao, C. Kong, and L. Chen, Chem. Eng. J. **220**, 1 (2013).

[75] L. Dumée, L. He, M. Hill, B. Zhu, M. Duke, J. Schütz, F. She, H. Wang, S. Gray, P. Hodgson, et al., J. Mater. Chem. A **1**, 9208 (2013).

[76] A. Huang, N. Wang, C. Kong, and J. Caro, Angew. Chem. Int. Ed. **51**, 10551 (2012).

[77] A. Huang, Q. Liu, N. Wang, Y. Zhu, and J. Caro, J. Am. Chem. Soc. **136**, 14686 (2014).

[78] N. Hara, M. Yoshimune, H. Negishi, K. Haraya, S. Hara, and T. Yamaguchi, J. Membr. Sci. **450**, 215 (2014).

[79] Z. Y. Yeo, P. W. Zhu, A. R. Mohamed, and S.-P. Chai, CrystEngComm **16**, 3072 (2014).

[80] D. Liu, X. Ma, H. Xi, and Y. Lin, J. Membr. Sci. **451**, 85 (2014).

[81] S. Aguado, J. Canivet, and D. Farrusseng, Chem. Commun. **46**, 7999 (2010).

[82] Y. Pan, T. Li, G. Lestari, and Z. Lai, J. Membr. Sci. **390**, 93 (2012).

[83] A. Huang, Q. Liu, N. Wang, and J. Caro, Micropor. Mesopor. Mat. **192**, 18 (2014).

[84] Y. Liu, E. Hu, E. A. Khan, and Z. Lai, J. Member. Sci. **353**, 36 (2010).

[85] M. Shah, H. T. Kwon, V. Tran, S. Sachdeva, and H.-K. Jeong, Micropor. Mesopor. Mat. **165**, 63 (2013).

[86] G. Xu, J. Yao, K. Wang, L. He, P. A. Webley, C.-s. Chen, and H. Wang, J. Membr. Sci. **385**, 187 (2011).

[87] K. Xu, Chem. Rev. **104**, 4303 (2004).

[88] V. M. A. Melgar, H. Ahn, J. Kim, and M. R. Othman, J. Ind. Eng. Chem. **21**, 575 (2015).

[89] K. Díaz, M. López-González, L. F. del Castillo, and E. Riande, J. Membr. Sci. **383**, 206 (2011).

[90] L. Li, J. Yao, X. Wang, Y.-B. Cheng, and H. Wang, J. Appl. Polym. Sci. **131** (2014).

[91] S. Japip, H. Wang, Y. Xiao, and T. Shung Chung, J. Membr. Sci. **467**, 162 (2014).

[92] S. Liu, G. Liu, X. Zhao, and W. Jin, J. Membr. Sci. **446**, 181 (2013).

[93] Y. Dai, J. R. Johnson, O. Karvan, D. S. Sholl, and W. J. Koros, J. Membr. Sci. **401**, 76 (2012).

[94] A. F. Bushell, M. P. Attfield, C. R. Mason, P. M. Budd, Y. Yampolskii, L. Starannikova, A. Rebrov, F. Bazzarelli, P. Bernardo, J. Carolus Jansen, et al., J. Membr. Sci. **427**, 48 (2013).

[95] A. Kudasheva, S. Sorribas, B. Zornoza, C. Téllez, and J. Coronas, J. Chem. Technol. Biotechnol. (2014).

[96] R. Mueller, V. Hariharan, C. Zhang, R. Lively, and S. Vasenkov, J. Membr. Sci. **499**, 12 (2016).

[97] M. Amirilargani and B. Sadatnia, J. Membr. Sci. **469**, 1 (2014).

[98] M. Fang, C. Wu, Z. Yang, T. Wang, Y. Xia, and J. Li, J. Membr. Sci. **474**, 103 (2015).

[99] C. Zhang, R. P. Lively, K. Zhang, J. R. Johnson, O. Karvan, and W. J. Koros, J. Phys. Chem. Lett. **3**, 2130 (2012).

[100] M. T. Luebbers, T. Wu, L. Shen, and R. I. Masel, Langmuir **26**, 15625 (2010).

[101] Y. Pan and Z. Lai, Chem. Commun. **47**, 10275 (2011).

[102] D. Peralta, G. Chaplais, A. Simon-Masseron, K. Barthelet, and G. D. Pirngruber, Ind. Eng. Chem. Res. **51**, 4692 (2012).

[103] L. Diestel, H. Bux, D. Wachsmuth, and J. Caro, Micropor. Mesopor. Mat. **164**, 288 (2012).

[104] D. Fairen-Jimenez, R. Galvelis, A. Torrisi, A. D. Gellan, M. T. Wharmby, P. A. Wright, C. Mellot-Draznieks, and T. Dueren, Dalton Trans. **41**, 10752 (2012).

[105] H. T. Kwon and H.-K. Jeong, J. Am. Chem. Soc. **135**, 10763 (2013).

[106] P. A. Mendes, P. Rodrigues, Alírio E .and Horcajada, C. Serre, and J. A. Silva, Micropor. Mesopor. Mat. **194**, 146 (2014).

[107] J. van den Bergh, C. Gücüyener, E. A. Pidko, E. J. Hensen, J. Gascon, and F. Kapteijn, Chem. Eur. J. **17**, 8832 (2011).

[108] T. Chokbunpiam, R. Chanajaree, O. Saengsawang, S. Reimann, C. Chmelik, S. Fritzsche, J. Caro, T. Remsungnen, and S. Hannongbua, Micropor. Mesopor. Mat. **174**, 126 (2013).

[109] U. Böhme, B. Barth, C. Paula, A. Kuhnt, W. Schwieger, A. Mundstock, J. Caro, and M. Hartmann, Langmuir **29**, 8592 (2013).

[110] D. Peralta, G. Chaplais, J.-L. Paillaud, A. Simon-Masseron, K. Barthelet, and G. D. Pirngruber, Micropor. Mesopor. Mat. **173**, 1 (2013).

[111] C. Gücüyener, J. van den Bergh, J. Gascon, and F. Kapteijn, J. Am. Chem. Soc. **132**, 17704 (2010).

[112] S. Sorribas, B. Zornoza, C. Téllez, and J. Coronas, J. Membr. Sci. **452**, 184 (2014).

[113] M. J. C. Ordonez, K. J. Balkus Jr., J. P. Ferraris, and I. H. Musselman, J. Membr. Sci. **361**, 28 (2010).

[114] A. F. Ferreira, M. C. Mittelmeijer-Hazeleger, M. A. Granato, V. F. D. Martins, A. E. Rodrigues, and G. Rothenberg, Phys. Chem. Chem. Phys. **15**, 8795 (2013).

[115] T. Chokbunpiam, R. Chanajaree, T. Remsungnen, O. Saengsawang, S. Fritzsche, C. Chmelik, J. Caro, W. Janke, and S. Hannongbua, Micropor. Mesopor. Mat. **187**, 1 (2014).

[116] D. I. Kolokolov, L. Diestel, J. Caro, D. Freude, and A. G. Stepanov, J. Phys. Chem. C **118**, 12873 (2014).

[117] K. Li, D. H. Olson, J. Seidel, T. J. Emge, H. Gong, H. Zeng, and J. Li, J. Am. Chem. Soc. **131**, 10368 (2009).

[118] M. Hartmann, U. Bohme, M. Hovestadt, and C. Paula, Langmuir **31**, 12382 (2015).

[119] H. T. Kwon and H.-K. Jeong, Chem. Commun. **49**, 3854 (2013).

[120] N. Chang, Z.-Y. Gu, and X.-P. Yan, J. Am. Chem. Soc. **132**, 13645 (2010).

[121] N. A. Khan, B. K. Jung, Z. Hasan, and S. H. Jhung, J. Hazard. Mater. **282**, 194 (2015).

[122] D. F. Sava, M. A. Rodriguez, K. W. Chapman, P. J. Chupas, J. A. Greathouse, P. S. Crozier, and T. M. Nenoff, J. Am. Chem. Soc. **133**, 12398 (2011).

[123] K. W. Chapman, D. F. Sava, G. J. Halder, P. J. Chupas, and T. M. Nenoff, J. Am. Chem. Soc. **133**, 18583 (2011).

[124] J. A. Gee, J. Chung, S. Nair, and D. S. Sholl, J. Phys. Chem. C **117**, 3169 (2013).

[125] L. H. Wee, Y. Li, K. Zhang, P. Davit, S. Bordiga, J. Jiang, I. F. Vankelecom, and J. A. Martens, Adv. Funct. Mater. (2014).

[126] J. Cousin Saint Remi, T. Rémy, V. Van Hunskerken, S. van de Perre, T. Duerinck, M. Maes, D. De Vos, E. Gobechiya, C. E. Kirschhock, G. V. Baron, et al., ChemSusChem **4**, 1074 (2011).

[127] K. Zhang, R. P. Lively, C. Zhang, W. J. Koros, and R. R. Chance, J. Phys. Chem. C **117**, 7214 (2013).

[128] R. P. Lively, M. E. Dose, J. A. Thompson, B. A. McCool, R. R. Chance, and W. J. Koros, Chem. Commun. **47**, 8667 (2011).

[129] C.-H. Kang, Y.-F. Lin, Y.-S. Huang, K.-L. Tung, K.-S. Chang, J.-T. Chen, W.-S. Hung, K.-R. Lee, and J.-Y. Lai, J. Membr. Sci. **438**, 105 (2013).

[130] G. M. Shi, H. Chen, Y. Jean, and T.-S. Chung, Polymer **54**, 774 (2013).

[131] G. M. Shi, T. Yang, and T. S. Chung, J. Membr. Sci. **415**, 577 (2012).

[132] K. Zhang, A. Nalaparaju, Y. Chen, and J. Jiang, Phys. Chem. Chem. Phys. **16**, 9643 (2014).

[133] K. Zhang, R. P. Lively, M. E. Dose, A. J. Brown, C. Zhang, J. Chung, S. Nair, W. J. Koros, and R. R. Chance, Chem. Commun. **49**, 3245 (2013).

[134] L. Ding and A. O. Yazaydin, Phys. Chem. Chem. Phys. **15**, 11856 (2013).

[135] J. Xie, F. Yan, Naiquiang ande Liu, Z. Qu, S. Yang, and P. Liu, Front. Environ. Sci. Eng. **8**, 162 (2014).

[136] J. Li, Y.-n. Wu, Z. Li, B. Zhang, M. Zhu, X. Hu, Y. Zhang, and F. Li, J. Phys. Chem. C **118**, 27382 (2014).

[137] B. K. Jung, J. W. Jun, Z. Hasan, and S. H. Jhung, Chem. Eng. J. **267**, 9 (2015).

[138] F. Yan, Z.-Y. Liu, J.-L. Chen, S. Xiao-Yan, X.-J. Li, M.-X. Su, B. Li, and B. Di, R. Soc. Chem. Adv. **4**, 33047 (2015).

[139] A. G. Kontos, Likodimos, C. M. Verziri, E. Kouvelos, N. Moustakas, G. N. Karanikolos, G. E. Romanos, and P. Falaras, ChemSusChem **7**, 1696 (2014).

[140] D. Liu, C. Zheng, Q. Yang, and C. Zhong, J. Phys. Chem. C **113**, 5004 (2009).

[141] R. B. Rankin, J. Liu, A. D. Kulkarni, and J. K. Johnson, J. Phys. Chem. C **113**, 16906 (2009).

[142] H. Amrouche, S. Aguado, J. Pérez-Pellitero, C. Chizallet, F. Siperstein, D. Farrusseng, N. Bats, and C. Nieto-Draghi, J. Phys. Chem. C **115**, 16425 (2011).

[143] A. Sirjoosingh, S. Alavi, and T. K. Woo, J. Phys. Chem. C **114**, 2171 (2010).

[144] Y. Houndonougbo, C. Signer, N. He, W. Morris, H. Furukawa, K. G. Ray, D. L. Olmsted, M. Asta, B. B. Laird, and O. M. Yaghi, J. Phys. Chem. Ch **117**, 10326 (2013).

[145] E.-Y. Chen, Y.-C. Liu, M. Zhou, L. Zhang, and Q. Wang, Chem. Eng. Sci. **71**, 178 (2012).

[146] S. S. Han, S.-H. Choi, and W. A. Goddard III, J. Phys. Chem. C **114**, 12039 (2010).

[147] E.-Y. Chen, Y.-C. Liu, T.-Y. Sun, Q. Wang, and L.-J. Liang, Chem. Eng. Sci. **97**, 60 (2013).

[148] H. Amrouche, B. Creton, F. Siperstein, and C. Nieto-Draghi, R. Soc. Chem. Adv. **2**, 6028 (2012).

[149] H.-c. Guo, F. Shi, Z.-f. Ma, and X.-q. Liu, J. Phys. Chem. C **114**, 12158 (2010).

[150] B. Liu and B. Smit, J. Phys. Chem. C **114**, 8515 (2010).

[151] E. Atci and S. Keskin, J. Phys. Chem. C **116**, 15525 (2012).

[152] A. Battisti, S. Taioli, and G. Garberoglio, Micropor. Mesopor. Mat. **143**, 46 (2011).

[153] L. Hertäg, H. Bux, J. Caro, C. Chmelik, T. Remsungnen, M. Knauth, and S. Fritzsche, J. Membr. Sci. **377**, 36 (2011).

[154] G. Yilmaz and S. Keskin, J. Membr. Sci. **454**, 407 (2014).

[155] J. Liu, S. Keskin, D. S. Sholl, and J. K. Johnson, J. Phys. Chem. C **115**, 12560 (2011).

[156] A. K. Rappé, C. J. Casewit, K. S. Colwell, W. A. Goddard III, and W. M. Skiff, J. Am. Chem. Soc. **114**, 10024 (1992).

[157] J. Pérez-Pellitero, H. Amrouche, F. R. Siperstein, G. Pirngruber, C. Nieto-Draghi, G. Chaplais, A. Simon-Masseron, D. Bazer-Bachi, D. Peralta, and N. Bats, Chem. Eur. J. **16**, 1560 (2010).

[158] J. J. G. Sevillano, S. Calero, C. O. Ania, J. B. Parra, F. Kapteijn, J. Gascon, and S. Hamad, J. Phys. Chem. C **117**, 466 (2012).

[159] W. L. Jorgensen and J. Tirado-Rives, J. Amer. Chem. Soc. **110**, 1657 (1988).

[160] K. G. Ray, D. Olmsted, N. He, Y. Houndonougbo, B. B. Laird, and M. Asta, Phys. Rev. B **85**, 085410 (2012).

[161] J. G. McDaniel, K. Yu, and J. R. Schmidt, J. Phys. Chem. C **116**, 1892 (2012).

[162] C. O. Ania, E. García-Pérez, M. Haro, G.-S. J. J., T. Valdés-Solís, J. B. Parra, and S. Calero, J. Phys. Chem. Lett. **3**, 1159 (2012).

[163] D. Fairen-Jimenez, S. A. Moggach, M. T. Wharmby, P. A. Wright, S. Parsons, and T. Duren, J. Am. Chem. Soc. **133**, 8900 (2011).

[164] M. Pera-Titus, ChemPhysChem **15**, 1581 (2014).

[165] H. Tanaka, S. Ohsaki, S. Hiraide, D. Yamamoto, S. Watanabe, and M. T. Miyahara, J. Phys. Chem. C **118**, 8445 (2014).

[166] R. Mueller, S. Zhang, C. Zhang, R. P. Lively, and S. Vasenkov, J. Membr. Sci. **477**, 123 (2014).

[167] Q. Song, S. Nataraj, M. V. Roussenova, J. C. Tan, D. J. Hughes, W. Li, P. Bourgoin, M. A. Alam, A. K. Cheetham, S. A. Al-Muhtaseb, et al., Energy Environ. Sci. **5**, 8339 (2012).

[168] B. Zheng, M. Sant, P. Demontis, and G. B. Suffritti, J. Phys. Chem. C **116**, 933 (2012).

[169] E. Haldoupis, T. Watanabe, S. Nair, and D. S. Sholl, ChemPhysChem **13**, 3449 (2012).

[170] L. Zhang, Z. Hu, and J. Jiang, J. Am. Chem. Soc. **135**, 3722 (2013).

[171] P. Schierz, S. Fritzsche, W. Janke, S. Hannongbua, O. Saengsawang, C. Chmelik, and J. Kärger, Micropor. Mesopor. Mat. **203**, 132 (2015).

[172] E. Pantatosaki, G. Megariotis, A.-K. Pusch, C. Chmelik, F. Stallmach, and G. K. Papadopoulos, J. Phys. Chem. C **116**, 201 (2012).

[173] X.-J. Hou and H. Li, J. Phys. Chem. C **114**, 13501 (2010).

[174] S. Wongprakarn, J. Prasongkit, and P. Srepusharawoot, Jpn. J. Appl. Phys. **53**, 08NK03 (2014).

[175] B. Assfour, S. Leoni, and G. Seifert, J. Phys. Chem. C **114**, 13381 (2010).

[176] F. G. Pazzona, P. Demontis, and G. B. Suffritii, J. Phys. Chem. C **117**, 349 (2012).

[177] C. Zhang, J. A. Gee, D. S. Sholl, and R. P. Lively, J. Phys. Chem. C **118**, 20727 (2014).

[178] D.-Y. Peng and D. B. Robinson, Ind. Eng. Chem. Fundam. **15**, 59 (1976).

[179] S. Brunauer, P. H. Emmett, and E. Teller, Journal of the American Chemical Society **60**, 309 (1938).

[180] K. S. Walton and R. Q. Snurr, Journal of the American Chemical Society **129**, 8552 (2007).

[181] C. Campaná, B. Mussard, and T. K. Woo, J. Chem. Theory Comput. **5**, 2866 (2009).

[182] J. G. Harris and K. H. Yung, J. Phys. Chem. **99**, 12021 (1995).

[183] L. Verlet and J.-J. Weis, Mol. Phys. **24**, 1013 (1972).

[184] R. Khare, A. K. Sum, S. K. Nath, and J. J. de Pablo, J. Phys. Chem. B **108**, 10071 (2004).

[185] W. L. Jorgensen, *Opls all-atom parameters for organic molecules, ions, & nucleic acids 12/96*, available by sending an email to W. L. Jorgensen.

[186] W. L. Jorgensen, *OPLS all-atom parameters for organic molecules, ions & nucleic acids 5/01*, available by sending an email to W. L. Jorgensen.

[187] N. He, *Force field for rho ZIFs for H_2S adsorption*, Private communcation.

[188] J. J. Potoff and J. I. Siepmann, AIChE Journal **47**, 1676 (2001).

[189] S. Aguado, G. Bergeret, M. P. Titus, V. Moizan, C. Nieto-Draghi, N. Bats, and D. Farrusseng, New J. Chem. **35**, 546 (2011).

[190] B. E. Conway, J. Electrochem. Soc. **138**, 1539 (1991).

[191] J. R. Miller and A. F. Burke, Electrochem. Soc. Interface **17**, 53 (2008).

[192] P. J. Hall, M. Mirzaeian, S. I. Fletcher, F. B. Sillars, A. J. R. Rennie, G. O. Shitta-Bey, G. Wilson, A. Cruden, and R. Carter, Energy Environ. Sci. **3**, 1238 (2010).

[193] C. Merlet, B. Rotenberg, P. A. Madden, P.-L. Taberna, P. Simon, Y. Gogotsi, and M. Salanne, Nat. Mater. **11**, 306 (2012).

[194] J. Vatamanu, O. Borodin, and G. D. Smith, Phys. Chem. Chem. Phys. **12**, 170 (2010).

[195] S. Kondrat, N. Georgi, M. V. Fedorov, and A. A. Kornyshev, Phys. Chem. Chem. Phys. **13**, 11359 (2011).

[196] D. A. Iozzo, M. Tong, G. Wu, and E. P. Furlani, J. Phys. Chem. C **119**, 25235 (2015).

[197] J. Chmiola, G. Yushin, Y. Gogotsi, C. Portet, P. Simon, and P.-L. Taberna, Science **313**, 1760 (2006).

[198] G. Feng and P. T. Cummings, J. Phys. Chem. Lett. **2**, 2859 (2011).

[199] Y. Shim, H. J. Kim, and Y. Jung, Faraday Discuss. **154**, 249 (2012).

[200] S. Kondrat, C. Perez, V. Presser, Y. Gogotsi, and A. Kornyshev, Energ. Environ. Sci. **5**, 6474 (2012).

[201] G.-W. Yang, C.-L. Xu, and H.-L. Li, Chem. Commun. pp. 6537–6539 (2008).

[202] W. Xing, S. Qiao, X. Wu, X. Gao, J. Zhou, S. Zhuo, S. B. Hartono, and D. Hulicova-Jurcakova, J. Power Sources **196**, 4123 (2011).

[203] H. Wang, J. Varghese, and L. Pilon, Electrochim. Acta **56**, 6189 (2011).

[204] H. Wang and L. Pilon, J. Phys. Chem. C **115**, 16711 (2011).

[205] J. A. Greathouse, S. E. Feller, and D. A. McQuarrie, Langmuir **10**, 2125 (1994).

[206] L. B. Bhuiyan, L. Blum, and D. Henderson, J. Chem. Phys. **78**, 442 (1983).

[207] M. Rose, Y. Korenblit, E. Kockrick, L. Borchardt, M. Oschatz, S. Kaskel, and G. Yushin, Small **7**, 1108 (2011).

[208] Y. Shim, Y. Jung, and H. J. Kim, J. Phys. Chem. C **115**, 23574 (2011).

[209] P. Simon and Y. Gogotsi, Nat. Mater. **7**, 845 (2008).

[210] A. Lewandowski, A. Olejniczak, M. Galinski, and I. Stepniak, J. Power Sources **195**, 5814 (2010).

[211] M. Armand, F. Endres, D. R. MacFarlane, H. Ohno, and B. Scrosati, Nat. Mater. **8**, 621 (2009).

[212] M. L. P. Le, L. Cointeaux, P. Strobel, J.-C. Lepretre, P. Judeinstein, and F. Alloin, J. Phys. Chem. C **116**, 7712 (2012).

[213] M. H. Kowsari, S. Alavi, M. Ashrafizaadeh, and B. Najafi, J. Chem. Phys. **130**, 014703 (2009).

[214] Y. Gur, I. Ravina, and A. J. Babchin, J. Colloid Interface Sci. **64**, 333 (1978).

[215] J. R. Macdonald and C. A. Barlow Jr., J. Chem. Phys. **36**, 3062 (1962).

[216] V. N. Paunov, R. I. Dimova, P. A. Kralchevsky, G. Broze, and A. Mehreteab, J. Colloid Interface Sci. **182**, 239 (1996).

[217] T. Malewitz, P. N. Pintauro, and D. Rear, J. Membr. Sci. **301**, 171 (2007).

[218] H. Chen and I. Nakamura, J. Phys. Chem. C **119**, 24714 (2015).

[219] L. Yang, B. H. Fishbine, A. Migliori, and L. R. Pratt, J. Chem. Phys. **132**, 044701 (2010).

[220] E. Glueckauf, Trans. Faraday Soc. **60**, 1637 (1964).

[221] L. Onsager, J. Am. Chem. Soc. **58**, 1486 (1936).

[222] I.-C. Yeh and M. L. Berkowitz, J. Chem. Phys. **110**, 7935 (1999).

[223] F. Booth, J. Chem. Phys. **19**, 391 (1951).

[224] R. L. Fulton, J. Chem. Phys. **20**, 204503 (2009).

[225] G. H. Haggis, J. B. Hasted, and T. J. Buchanan, J. Chem. Phys. **20**, 1452 (1952).

[226] F. E. Harris and C. T. O'Konski, J. Phys. Chem. **61**, 310 (1957).

[227] J. B. Hasted and G. W. Roderick, J. Chem. Phys. **29**, 17 (1958).

[228] E. A. S. Cavell, J. Chem. Soc. Faraday Trans. 2 **78**, 537 (1982).

[229] J. Barthel and R. Buchner, Pure Appl. Chem. **58**, 1077 (1986).

[230] U. Kaatze, J. Mol. Liq. **162**, 105 (2011).

[231] D. Ben-Yaakov, D. Andelman, and R. Podgornik, J. Chem. Phys. **134**, 074705 (2011).

[232] Y. Marcus, J. Solution Chem. **42**, 2354 (2013).

[233] J. B. Hubbard, L. Onsager, W. M. van Beek, and M. Mandel, Proc. Natl. Acad. Sci. USA **74**, 401 (1977).

[234] J. Anderson, J. Ullo, and S. Yip, Chem. Phys. Lett. **152**, 447 (1988).

[235] G. Löffler, H. Schreiber, and O. Steinhauser, J. Mol. Biol. **270**, 520 (1997).

[236] L. Yang, S. Weerasinghe, P. E. Smith, and B. M. Pettitt, Biophys. J. **69**, 1519 (1995).

[237] S. Plimpton, J. Comp. Phys. **117**, 1 (1995).

[238] L. Martínez, R. Andrade, E. G. Birgin, and J. M. Martínez, J. Comp. Chem. **30**, 2157 (2009).

[239] W. D. Cornell, P. Cieplak, C. I. Bayly, I. R. Gould, K. M. Merz, D. M. Ferguson, D. C. Spellmeyer, T. Fox, J. W. Caldwell, and P. A. Kollman, J. Am. Chem. Phys. **117**, 5179 (1995).

[240] *Simulation Studies of Ions in Ethylene Carbonate* (2013).

[241] D. R. Wheeler, Ph.D. thesis, University of California, Berkeley (2002).

[242] C. D. Wick, J. M. Stubbs, N. Rai, and J. I. Siepmann, J. Phys. Chem. B **109**, 18974 (2005).

[243] J.-P. Ryckaert, G. Ciccotti, and H. J. Berendsen, J. Comp. Phys. **23**, 327 (1977).

[244] B. R. Arbad, M. K. Lande, N. N. Wankhede, and D. S. Wankhede, J. Chem. Eng. Data **51**, 68 (2006).

[245] P. S. Nikam, L. N. Shirsat, and M. Hasan, J. Chem. Eng. Data **43**, 732 (1998).

[246] I. Garcia de la Fuente, J. A. Gonzalez, J. C. Cobos, and C. Casanova, J. Chem. Eng. Data **37**, 535 (1992).

[247] R. Payne and I. E. Theodorou, J. Phys. Chem. **76**, 2892 (1972).

[248] G. P. Cunningham, G. A. Vidulich, and R. L. Kay, J. Chem. Eng. Data **12**, 336 (1967).

[249] I. M. Svishchev and P. G. Kusalik, Phys. Rev. Lett. **73**, 975 (1994).

[250] P. Winsor IV and R. H. Cole, J. Phys. Chem. **86**, 2486 (1982).

[251] M. L. T. Asaki, A. Redondo, T. A. Zawodzinski, and A. J. . Taylor, J. Chem. Phys. **116**, 8469 (2002).

[252] W. M. van Beek and M. Mandel, J. Chem. Soc. Faraday Trans. 1 (????).

[253] Y.-Z. Wei, P. Chiang, and S. Sridhar, J. Chem. Phys. **96**, 4569 (1992).

[254] A. Lileev and A. Lyashchenko, J. Mol. Liq. **150**, 4 (2009).

[255] R. Buchner and G. Hefter, J. Sol. Chem. **31**, 521 (2002).

[256] D. Spångberg and K. Hermansson, Chem. Phys. **300**, 165 (2004).